

ANALYSIS OF POROSITY EVOLUTION DURING LOW TEMPERATURE  
METAMORPHISM OF BASALTIC LAVAS AND IMPLICATIONS FOR FLUID  
FLOW

By

JANE E. GUSTAVSON

A THESIS PRESENTED TO THE GRADUATE SCHOOL  
OF THE UNIVERSITY OF FLORIDA IN PARTIAL FULFILLMENT  
OF THE REQUIREMENTS FOR THE DEGREE OF  
MASTER OF SCIENCE

UNIVERSITY OF FLORIDA

2006

Copyright 2006

by

Jane E. Gustavson

## ACKNOWLEDGMENTS

There are many people in my life who have been influential in helping me to obtain my Master of Science. Of those, there are a few that require special mention. My father, James M. Gustavson, did all that he knew to provide the best for his children. If it were not for his selflessness and honest love, I would not be the person I am today. Allyn Spear, though we have a mottled history, was the one who stood beside me and gave me the courage to pursue a higher level of education when I was filled with so much self doubt. Dr. Philip S. Neuhoff was always there with a patient yet guiding hand to see me through my research. He has become more than just my advisor; he is also a good friend. And finally, PJ Moore, who has become the companion I have searched for. His promise to walk beside me gives me the strength to enter the real world with the confidence I need to succeed.

## TABLE OF CONTENTS

|   | <u>page</u> |
|---|-------------|
| ACKNOWLEDGMENTS .....   | iii         |
| LIST OF TABLES .....  | vi          |
| LIST OF FIGURES .....   | viii        |
| ABSTRACT .....  | xi          |
| CHAPTER   |             |
| 1 INTRODUCTION .....  | 1           |
| Porosity and Permeability in Vesicular Lavas.....                           | 3           |
| Low Grade Alteration of Basaltic Lavas .....                                | 6           |
| Coupling Between Porosity Evolution and Chemical Reactions .....            | 8           |
| Role of the Present study .....   | 9           |
| 2 LOW-GRADE ALTERATION OF THE NORTH SHORE VOLCANIC GROUP,<br>MINNESOTA..... | 10          |
| Introduction.....   | 10          |
| Geologic Background .....   | 12          |
| Methods .....   | 15          |
| Results.....  | 17          |
| Primary Basalt Composition and Mineralogy .....                             | 17          |
| Regional Alteration Mineralogy.....   | 22          |
| Laumontite zone lavas.....  | 26          |
| Stilbite-heulandite zone lavas.....   | 27          |
| Thomsonite-mesolite zone lavas .....  | 27          |
| Analcime zone lavas.....  | 28          |
| Alteration Mineral Chemistry.....   | 29          |
| Discussion.....   | 31          |
| Regional Variation of Metamorphic Grade .....                               | 31          |
| Conditions of Alteration .....  | 38          |
| Structural Interpretations .....  | 42          |

|   |   |     |
|---|---|-----|
| 3 | PETROGRAPHIC AND DIGITAL ANALYSIS OF POROSITY EVOLUTION DURING ALTERATION ..... | 45  |
|   | Introduction.....   | 45  |
|   | Methods .....   | 47  |
|   | Field Techniques .....  | 47  |
|   | Optical and Digital Techniques .....  | 48  |
|   | Observations .....  | 49  |
|   | NSVG Field Sites 3, 4 and 6 .....   | 49  |
|   | Reaction Progress .....   | 55  |
|   | Partial infilling at low-grades .....   | 55  |
|   | Mafic phyllosilicate to zeolite infilling .....                                 | 58  |
|   | Multiple stage zeolite infilling .....  | 63  |
|   | Discussion.....   | 63  |
|   | Nature of Porosity and Permeability in Basalts.....                             | 63  |
|   | Controls on Reaction Progress .....   | 68  |
| 4 | MODELING OF MINERAL PARAGENESES .....   | 70  |
|   | Introduction.....   | 70  |
|   | Methods .....   | 71  |
|   | Results.....  | 75  |
|   | Mineral Parageneses.....  | 75  |
|   | Volume Changes During Alteration.....   | 83  |
| 5 | DISCUSSION.....   | 86  |
|   | Reaction Progress in Low-Grade Metabasalts.....                                 | 86  |
|   | Dependence of Reaction Progress on Pore Size .....                              | 88  |
| 6 | CONCLUSIONS .....   | 96  |
|   | LIST OF REFERENCES .....  | 99  |
|   | BIOGRAPHICAL SKETCH .....   | 110 |

## LIST OF TABLES

| <u>Table</u>   | <u>page</u> |
|--|-------------|
| 2.1 Field study locations in the North Shore Volcanic Group. ....  | 16          |
| 2.2 Whole-rock chemical compositions (wt %) of samples. ....   | 18          |
| 2.3 Representative compositions of plagioclase. ....   | 20          |
| 2.4 Representative compositions of pyroxenes. ....   | 21          |
| 2.5 Representative compositions of mafic phyllosilicates. ....   | 30          |
| 2.6 Representative compositions of thomsonites. ....   | 32          |
| 2.7 Representative compositions of mesolite, analcime, and laumontite. ....  | 34          |
| 3.1 Statistical analysis of vesicle size (diameter) as a function of reaction progress<br>from outcrop scale measurements at Site 6. ....  | 51          |
| 3.2 Statistical analysis of vesicle size (area) as a function of reaction progress from<br>measured vesicles of a low-grade metabasalt from East Greenland (thin section<br>421505). ....          | 57          |
| 3.3 Statistical analysis of vesicle size as a function of reaction progress for vesicles<br>filled with chlorite and/or laumontite at the thin section scale (sample NS04-14)<br>from Site 4. .... | 59          |
| 3.4 Statistical analysis of vesicle areas (mm <sup>2</sup> ) and clay rim thicknesses (mm) for<br>sample 94-80 from eastern Iceland. ....  | 63          |
| 4.1 Bulk rock composition for olivine tholeiite basalt (wt %) ....   | 72          |
| 4.2 Modal abundances and compositions of primary mineral phases in olivine<br>tholeiite. ....  | 72          |
| 4.3 Calculated anhydrous bulk composition of basaltic andesite before and after<br>reaction. ....  | 74          |
| 4.4 Reactant phase composition, abundance, and relative dissolution rate in basaltic<br>andesite used as input for reaction path model. ....   | 75          |

|     |  |    |
|-----|--|----|
| 4.5 | Mole, volume and mass amounts in unaltered and altered andesite for the computer (modeled) and mathematical (calculated) models..... | 81 |
| 4.6 | Phase compositions and abundances at end of reaction path for basaltic andesite.   | 82 |

## LIST OF FIGURES

| <u>Figure</u>  | <u>page</u> |
|--|-------------|
| 1.1 Cross sectional view showing distribution of primary porosity (vesicles, scoria, breccia) typical of thick aa lava flows.....  | 4           |
| 1.2 Schematic diagrams depicting the effects of pore size, shape and connectivity on the permeability of vesicular basalts. ....   | 4           |
| 2.1 Generalized geological map of northeastern Minnesota showing the distribution of the NSVG lavas and associated Keweenaw intrusives (after Miller <i>et al.</i> , 2001).....  | 11          |
| 2.2 Flow boundary between two vesicular basalt flows at Site 12. ....  | 14          |
| 2.3 Total alkalis-silica diagram showing compositional ranges of NSVG basalts sampled in this study (black circles). ....  | 19          |
| 2.4 Field photo from Site 3 (Table 2.1) showing an extensively altered pahoehoe flow. Visible within the flow are bleached haloes around vesicles connected by thin anastomosing bleached areas. ....                        | 23          |
| 2.5 Secondary alteration in NSVG lavas. All photomicrographs were taken through partially crossed polars.....  | 24          |
| 2.6 Compositions of mafic phyllosilicates formed during regional metamorphism of the NSVG as a function of the number of non-interlayer cations (Si + Al + Mg + Fe) versus the interlayer charge (2 Ca + Na + K). ....       | 31          |
| 2.7 Plot showing the compositional variation of analyzed thomsonites in NSVG basalts (black circles). ....   | 33          |
| 2.8 Generalized map of northeastern Minnesota showing the distribution of NSVG lavas (gray) and interpretations of metamorphic grade based on this study and the work of Schmidt (1993) and Schmidt and Robinson (1997)..... | 35          |
| 2.9 Stratigraphy of the NSVG (Vervoort and Green, 1997; Miller <i>et al.</i> , 2002) correlated along the fold axis dividing the lavas into the southwest and northeast limb.....  | 36          |

|      |  |    |
|------|--|----|
| 2.10 | Schematic diagram showing the distribution of minerals and mineral zones typically developed during very low grade metamorphism of large igneous provinces (after Walker, 1960; Neuhoff <i>et al.</i> , 1997, 2000).                               | 39 |
| 3.1  | Outcrop photograph of vesicular basalt at Site 6 ( <b>Table 2.1</b> ) illustrating typical variation in pore size, shape and spacing.  | 50 |
| 3.2  | Images of reaction zones around and between macroscopic pore space in NSVG lavas.  | 52 |
| 3.3  | Image is of sample NS04-14, showing the laumontite zone alteration found at Site 4.  | 53 |
| 3.4  | Various levels of secondary alteration in the matrix of NSVG basalts sampled during the field season. All photomicrographs were taken through crossed polars.  | 54 |
| 3.5  | Example of digital analysis of vesicle fillings in a zeolite facies vesicular lava from East Greenland.  | 56 |
| 3.6  | Frequency of vesicle areas versus the amount of secondary alteration filling the vesicle for a sample of chabazite-thomsonite zone alteration from East Greenland (cf. Neuhoff <i>et al.</i> , 1997).  | 58 |
| 3.7  | Plot shows the thickness in mm of chlorite rims (black circles) and the total percent of the vesicle filled with chlorite (open circles) with respect to total vesicle area in mm <sup>2</sup> .   | 60 |
| 3.8  | Plot shows the percentage of mineral infilling with respect to total vesicle area.   | 61 |
| 3.9  | Photomicrograph showing a thin section of a mesolite-scolecite zone lava from eastern Iceland.   | 62 |
| 3.10 | Data compiled from digital analysis of mesolite-scolecite zone lava from eastern Iceland (refer to <b>Figure 3.3</b> ).  | 64 |
| 4.1  | Mineralogic composition of lavas as a function of reaction progress. Panels A, B, and C depict individual models.  | 76 |
| 4.2  | Instantaneous change in total mineral volume as a function of reaction progress. Panels A, B, and C correspond to models shown in <b>Figure 4.1</b> .  | 84 |
| 5.1  | Schematic representation of a spherical pore of radius $r_{\text{pore}}$ surrounded by a reaction aureole of thickness $x_{\text{aureole}}$ .  | 89 |
| 5.2  | Graph depicting the percentage of volume occupied by the pore in a given pore-aureole local reaction region as a function of $r_{\text{pore}}$ and $x_{\text{aureole}}$ using pore sizes and aureole thicknesses typical of vesicular mafic lavas. | 90 |

|     |  |
|-----|--|
| 5.3 | Schematic representation of a spherical pore showing secondary infilling typical of the petrographically observed alteration in the basaltic andesite of the NSVG. .92   |
| 5.4 | Plot depicting the aureole thickness (x) required to completely fill pore space within a vesicle of a given pore radius ( $r_{\text{pore}}$ ) with alteration minerals, shown for total infilling and for clay or laumontite infilling. ....93 |
| 5.5 | Percent chlorite infilling as a function of the axial ratio for an ellipsoidal vesicle elongated in one direction assuming a constant volume and a constant chlorite rim thickness. ....94   |

Abstract of Thesis Presented to the Graduate School  
of the University of Florida in Partial Fulfillment of the  
Requirements for the Degree of Master of Science

ANALYSIS OF POROSITY EVOLUTION DURING LOW TEMPERATURE  
METAMORPHISM OF BASALTIC LAVAS AND IMPLICATIONS FOR FLUID  
FLOW

By

Jane E. Gustavson

August 2006

Chair: Philip S. Neuhoff

Major Department: Geological Sciences

Basaltic lavas are the most abundant rock type in the crust and globally form important reservoirs for the migration and storage of crustal fluids. As in any porous medium, the porosity and permeability of basalt lavas control the movement and extent of chemical interaction of these fluids and thus the availability and quality of obtainable resources (e.g., groundwater and petroleum). The highly-reactive nature of basaltic lavas near the surface leads to intimate coupling between hydrologic properties and extent of chemical alteration, which controls the aquifer/reservoir quality and chemical fluxes during alteration. Our ability to quantitatively understand these processes is limited by rigorous models of how chemical reactions and porosity/permeability modifications are coupled in these systems.

In the present study, development of secondary mineral parageneses is used as a monitor of fluid access to pores and to obtain a quantitative description and interpretation

of the evolution of pore space through time. This work has shown that fluid movement through vesicular basalts occurs along a permeable network of microfractures and connected vesicles, which are depicted by the extremely weathered aureoles of alteration surrounding these pathways and the vesicles they connect.

This research also shows that the extent of reaction progress, as evidenced by the temporal sequence of mineral infillings within pore space, is heavily influenced by the vesicle size and shape. Larger vesicles exhibit greater degrees of reaction progress while smaller ones are closed off earlier in the reaction progress. Irregularly shaped vesicles may close off earlier in the reaction progress due to constriction caused by the shortest diameter. This dependence of reaction progress on pore size is more specifically based on the volume percent occupied by the pore within a closed pore-aureole system. Each vesicle independently exchanges chemical components with the surrounding lava matrix (the alteration aureole), implying that the reaction progress exhibited within a given vesicle is based on the proportion of the vesicle to aureole size. For a given vesicle size, the pore space evolution due to secondary mineralization will be less with a smaller alteration aureole, due to the low level of fluid rock interaction evidenced by this smaller alteration aureole. Inversely, a larger alteration aureole implies a higher level of fluid-rock interaction, which may create enough secondary mineralization to progress to later stages of alteration or to completely fill the pore space.

## CHAPTER 1 INTRODUCTION

Fluid movement is inherently coupled with geochemical reactions during earth processes. Mass transport of chemical species during fluid flow has received considerable attention as a means of explaining the chemical evolution of geochemical systems such as hydrothermal ore deposits, petroleum reservoirs, groundwater aquifers, and metamorphic systems (e.g., reviews and references therein of Norton and Knight, 1977; Cathles, 1981, 1990; Etheridge et al., 1983; Garven and Freeze, 1984a,b; Norton, 1984; Wood and Hewett, 1984; Garven, 1985, 1989, 1995; Broedehoeft and Norton, 1990; Steefel and Lasaga, 1992; Garven et al., 1993; Garven and Raffensperger, 1994; Raffensperger and Garven, 1995a,b; Lichtner et al., 1996; Person et al., 1996; and many others). Dissolution and precipitation of solid phases during reactive transport processes leads to changes in permeability and porosity of rocks and sediments. Permeability influences the extent and distribution of chemical alteration during hydrothermal and metamorphic processes by controlling the rates and magnitudes of supply and removal of chemical species (e.g., Lasaga, 1986, 1989; Ortoleva et al., 1987; Norton, 1988; Dewers and Ortoleva, 1990; Steefel and Van Cappellen, 1990; Steefel and Lasaga, 1992, 1994; Manning et al., 1993; Lasaga and Rye, 1993; Rose, 1995; Bolten et al., 1999). Porosity controls the amount of aqueous solution that is in contact with the porous media, and can also have considerable effects on permeability (Xu and Pruess, 2001).

The interrelation between porosity, permeability, and chemical reaction is especially profound in basaltic lavas and other volcanic rocks. The effect of mineral

paragenesis on porosity in low-grade metabasalts has been noted in many studies (Schmidt, 1990, 1993; Bevins, Rowbotham, and Robinson, 1991; Manning and Bird, 1991, 1995; Robert and Goffé, 1993; Schmidt and Robinson, 1997; Neuhoff *et al.*, 1999). Basaltic lavas are the most abundant rock type in the earth's crust (Wedepohl, 1969), and can form extensive aquifers for the storage and migration of groundwater (e.g., Kononov, 1978; Ingebritson and Scholl, 1993; Rose *et al.*, 1996; Manga, 1997, 1999), geothermal fluids (e.g., Arnorsson, 1995a, b) and petroleum (e.g., Pendkar and Kumar, 1999; Christiansen, 1994; Iijima, 2001). Once basaltic lavas are emplaced at the surface of the earth, the primary magmatic phases formed during cooling (i.e., olivine, anorthite-rich plagioclase, pyroxenes, oxides and glass) are metastable. The highly-reactive nature of basaltic lavas near earth's surface leads to extensive dissolution and hydrolysis of the primary magmatic phases that releases chemical constituents of the lavas into the aqueous phase. There they are transported by diffusion and advection through the rock (e.g., Steefel and Lasaga, 1992) and/or re-precipitated in secondary mineral phases such as clays, zeolites, and silica minerals. These phases have relatively large molar volumes and typically occlude pore space as they require additional room to grow beyond the space generated through dissolution or hydrolysis of the primary basaltic minerals. This causes portions of the rock to be closed off from the fluid flow pathway, which has a significant effect on the porosity and fluid movement through the rock.

This thesis explores the relationship between porosity evolution during secondary mineral paragenesis and fluid flow through vesicular basalts. The following sections of this chapter provide a review of the nature of porosity and permeability in vesicular lavas, low-grade alteration of basaltic lavas, and the relationships between chemical reaction,

porosity, and permeability in terms of fluid movement through these lavas. This information is used to pose several questions about the coupling of chemical alteration and porosity evolution in lavas that are addressed by the work below.

### **Porosity and Permeability in Vesicular Lavas**

Due to parameters such as temperature and pressure experienced by the lava flow during eruption, total porosity can vary significantly within a single stratigraphic flow as can factors such as the size, spacing and geometry of pore spaces (e.g., Larsen *et al.*, 2004; Burgisser and Gardner, 2004). Vesicular basalt flows can generally be divided into three sections based on the density of vesicles (Figure 1.1): 1) the bottom, which is high in porosity with elongated pores due to the stress of overburden during flow; 2) the center, which tends to be massive and lacks pores; and 3) the top, which has the highest porosity and more spherical pores due to less overburden pressure during deposition (Neuhoff *et al.*, 1999).

As a consequence, porosity can vary dramatically from essentially 0% in the massive flow centers up to 85% in scoraceous zones (e.g., Cashman and Mangan, 1994). The macroscopic porosity depicted in Figure 1.1 tends to dominate total porosity, as porosities determined by point counting or other digital analyses tend to agree well with those obtained by laboratory techniques (e.g., Saar and Manga, 1999, Al-Harhi *et al.*, 1999).

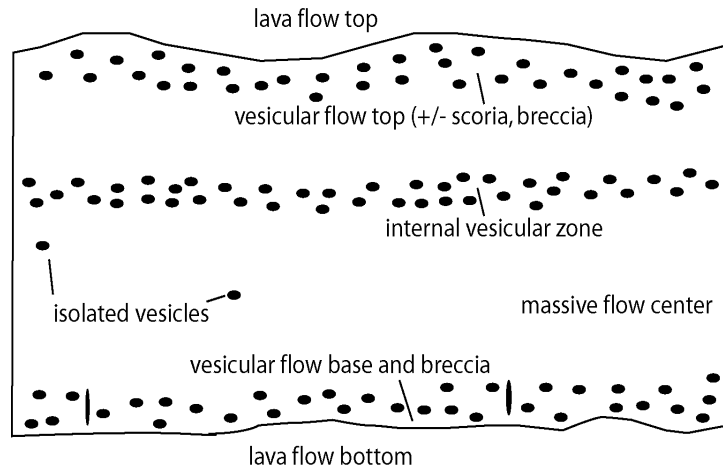


Figure 1.1: Cross sectional view showing distribution of primary porosity (vesicles, scoria, breccia) typical of thick aa lava flows. Note heterogeneous but regular distribution of porosity through the flow.

Figure 1.2 illustrates three different possible pore geometries within the vesicular zones of basalt. In Figure 1.2A, the highly vesicular lava contains coalesced pore spaces, leading to high permeability that is controlled by the apertures of the pore intersections (Saar and Manga, 1999); this situation is typical of scoraceous zones within flow tops. At lower porosities, where vesicle density is too low for widespread coalescence, variations in vesicle geometry can have a profound effect on the nature of permeability.

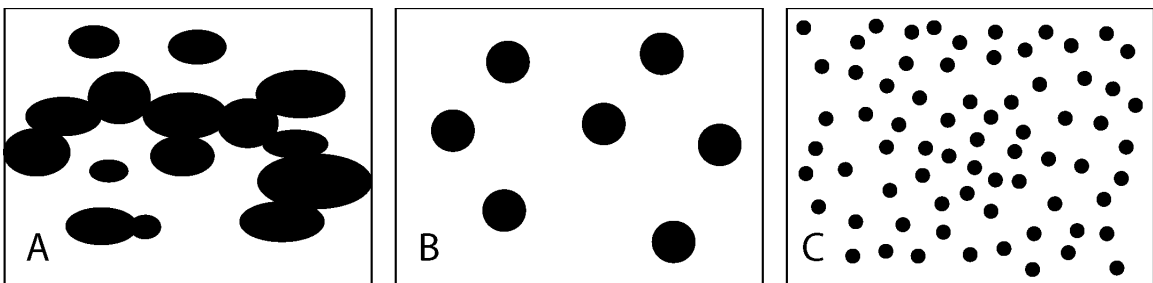


Figure 1.2: Schematic diagrams depicting the effects of pore size, shape and connectivity on the permeability of vesicular basalts. The lava depicted in (A) has highest porosity, with coalesced vesicles that lead to connected fluid flow paths. The lavas shown in (B) and (C) have the same porosity, but different pore size and mean pore-pore distances that will affect the ease and direction of fluid flow through the rock.

For instance, the lavas depicted in parts B and C have the same porosity, but different pore sizes. The distribution of pore space into a greater number of smaller pores in part C relative to that in part B leads to significantly reduced pore-pore distances, which is likely to impact the ease of fluid movement between pores. These variations in porosity and pore geometry depicted in Figure 1.2 can exist even within a single vesicular zone of the basalt (Gardner *et al.*, 1996).

Vesicular volcanic rocks exhibit a wide range of permeabilities, ranging from about  $10^{-7}$  to  $10^{-16}$  cm<sup>2</sup> (e.g., Klug and Cashman, 1996; Saar and Manga, 1999; Mueller *et al.*, 2005). Zones within basaltic lavas exhibiting macroscopic porosity generally have relatively high permeabilities, often in the range of  $10^{-7}$  to  $10^{-11}$  cm<sup>2</sup>. This is comparable to clean unconsolidated sand or karstic limestone. Matrix permeabilities in non-porous lavas can be considerably lower, often as low as  $10^{-16}$  cm<sup>2</sup> (e.g., Saar and Manga, 1999; Sruoga *et al.*, 2004; Mueller *et al.*, 2004).

Recent research demonstrates that vesicular basalts do not follow porosity-permeability relations typically applied to granular rocks (Saar and Manga, 1999). Previous studies of the relationship between porosity and permeability in granular rocks have applied percolation theory (e.g., Carman, 1956; Dullien, 1992; Bosl *et al.*, 1998) which predicts a percolation threshold, or the minimum porosity at which a connected pathway for fluid movement through the sample exists, of 30%. Following this theory, when the porosity of a sample drops below this critical value there will be a dramatic decrease in permeability. This approach leads to widely applied power law dependencies of permeability on porosity such as the Kozeny-Carman equation (e.g., Carman, 1956; Dullien, 1992; Le Gallo *et al.*, 1998; Balashov and Yardley, 1998; Park and Ortoleva,

2003; Freedman *et al.*, 2003). Experimental studies of lava degassing, transport modeling, and textural studies of pumices and other high-vesicular materials predict that interconnected pathways resulting from bubble coalescence of vesicles generally occur at porosities over 30 % (e.g., Klug and Cashman, 1996; Blower, 2001; Mueller *et al.*, 2004; Burgisser and Gardner, 2005). However, it is clear that vesicular volcanic rocks exhibit relatively high, but variable, permeabilities ( $\sim 10^{-8}$  cm<sup>2</sup>) down to porosities as low as a few percent, in contrast to the behavior of granular rocks and the predictions of percolation theory (e.g., Saar and Manga, 1999; Mueller *et al.*, 2004). Numerous models have been proposed to explain this behavior, largely relying on textural explanations (e.g., Saar and Manga, 1999; Blower, 2001). Recent work has suggested that the elevated permeabilities in volcanic rocks are associated with microfractures formed between vesicles during degassing, leading to connected fluid pathways that are not quantitatively important components of total porosity (Mueller *et al.*, 2004).

### **Low Grade Alteration of Basaltic Lavas**

When basalt is emplaced at the earth's surface it is metastable. The olivine, pyroxene, anorthite-rich plagioclase, oxide and glass phases in basalts form under higher temperature conditions and are easily weathered at surface conditions. Chemical alteration of basalts begins to occur almost immediately after emplacement (e.g., Hearn *et al.*, 1981; Jakobsson and Moore, 1986), and the specific reactions that take place between basaltic lavas and groundwaters are strongly dependent on temperature and pressure conditions as well as the composition of the lavas and fluids (e.g., Kristmannsdóttir and Tómasson, 1978; Neuhoff *et al.*, 1999, 2000). In general, the sequence of reactions experienced by lavas of this nature can be summarized as 1) reaction of lavas with oxygenated aqueous solutions forming iron oxyhydroxides, celadonite, amorphous silica,

amorphous aluminosilicates, and clay minerals during weathering; 2) continued reaction of the lavas to form clay minerals (smectite, chlorite) and later zeolites and other calcium aluminosilicates during burial metamorphism; and 3) localized, late stage hydrothermal alteration in fracture systems around intrusions (Neuhoff *et al.*, 1999). These various stages of mineral formation can be distinguished through careful use of geologic relationships and relative dating techniques (Neuhoff *et al.*, 1999).

The sequence of chemical reactions that alter basaltic lavas after emplacement typically leads to the development of depth-controlled zones, which reflect increasing temperature with depth. Clay minerals trend from dioctahedral smectite to trioctahedral smectite to mixed layer chlorite-smectite to chlorite with increasing depth/temperature (e.g., Schiffman and Friedliefsson, 1991; Neuhoff *et al.*, 1999, 2006); these minerals are observed as replacements of glass, olivine, pyroxenes, fine-grained groundmass, sometimes plagioclase, and are also found to rim vesicle walls. Zeolites occur as replacements of plagioclase and occasionally groundmass, and more commonly as vesicle infillings after formation of mafic phyllosilicates.

Prominent depth-controlled distribution of individual zeolite species within vesicles is often noted, allowing delineation of mineral zones defined by the occurrence of one or more index zeolite species. These zones are well described in many tholeiitic lava flows throughout the world, and as many as five separate zones exist in regionally metamorphosed basaltic lavas and Icelandic geothermal systems (Walker, 1951, 1960a, b; Sukheswala *et al.*, 1974; Kristmannsdottir and Tomasson, 1978; Jorgensen, 1984; Murata *et al.*, 1987; Schmidt, 1990, 1993; Neuhoff *et al.*, 1997, 1999; Christiansen *et al.*, 1999). They are relatively uniform in thickness over large distances and cross-cut

individual lava flows. The thickness, orientation, and geologic relations between these mineral zones and lava stratigraphy provide critical information for assessing pre-erosional lava thicknesses as well as crustal deformation (e.g., Neuhoff *et al.*, 1997, 2000).

### **Coupling Between Porosity Evolution and Chemical Reactions**

As in any porous medium, the hydrologic properties of basalt lavas control the movement and extent of fluid-rock interaction, which affects the formation of secondary minerals and thus the availability and quality of obtainable resources (e.g., groundwater and petroleum). In principle, porosity change during chemical alteration can be determined from the change in mineral volume during reaction due to mineral dissolution and precipitation. The extent of porosity destruction is a function of both the relative volumes of primary and secondary phases, and of their relative solubilities in the aqueous phase (Putnis, 2002). Provided a suitable determinative relationship between porosity and permeability is known (such as the Kozeny-Carman equation; Carman, 1956), changes in mineral volume during chemical reaction from petrographic or modeling results can be used to estimate changes in permeability (e.g., Steefel and Lasaga, 1994; Panda and Lake, 1995; Balashov and Yardley, 1998; Le Gallo *et al.*, 1998; Saripalli *et al.*, 2001, 2005; Park and Ortoleva, 2003; Xu and Pruess, 2001; Freedman *et al.*, 2003).

In low-grade metabasalts, the destruction of porosity is evident through the progressive infilling of vesicles by phases such as mafic phyllosilicates and zeolites. This is a direct consequence of the open crystal structures of mafic phyllosilicates and zeolites, which leads to a net increase in mineral volume (Neuhoff *et al.*, 1999, 2000). These pore fillings will alter the size, geometry and connectivity of the pore space and can effectively close off portions of the rock to further alteration (Neuhoff *et al.*, 1999).

Because, as noted above, permeability of vesicular lavas is likely strongly dependent on the geometry of the pore space, these processes may lead to variations in permeability with reaction progress that are not readily predicted by simple power-law porosity-permeability relationships. What is clear is that progressive alteration of lavas leads to distinct reductions in permeability, for instance in oceanic lavas (Fisher, 1998), petroleum reservoirs (Sruoga *et al.*, 2004; Luo *et al.*, 2005), and geothermal systems (Stimac *et al.*, 2004).

### **Role of the Present study**

The ability to quantify and further understand the time dependent changes in the properties of porous media is sought after by geologists, hydrologists and oil companies among many others (Aharonov *et al.*, 1997). The evolution of porosity and permeability during reactive transport has received surprisingly little attention (e.g., Steefel and Lasaga, 1994; Le Gallo, 1998; Saripalli *et al.*, 2001; Freedman *et al.*, 2003), and our ability to quantitatively understand these processes is limited due to a lack of rigorous models of how chemical reactions and porosity/permeability modifications are coupled in these systems. This is particularly true for vesicular lavas for reasons noted above. The present study uses secondary mineral parageneses in vesicular basalts to address three aspects of this problem:

1. What causes the high permeabilities of vesicular volcanic rocks, even at low porosities?
2. Does the extent of reaction progress (as evidenced by the temporal sequence of mineral infillings of pore space) vary with aspects of pore geometry such as spacing, size, and shape?
3. What is the relationship between pore geometry and porosity evolution during mineral paragenesis?

CHAPTER 2  
LOW-GRADE ALTERATION OF THE NORTH SHORE VOLCANIC GROUP,  
MINNESOTA

**Introduction**

The distribution of individual zeolites, filling vesicles in low-grade metabasalts of large igneous provinces, is typically characterized by several depth-controlled zones defined by the occurrence of one or more index zeolite species (e.g., Walker, 1960a,b; Sukheswala *et al.*, 1974; Murata *et al.*, 1987; Schmidt, 1993; Neuhoff *et al.*, 1997, 1999). The thicknesses, orientations, and geologic relations between these mineral zones and lava stratigraphy provide critical information for assessing geothermal gradients, crustal deformation, and pre-erosional lava thicknesses (e.g., Neuhoff *et al.*, 1997, 2000). This style of alteration has typically been observed in Mesozoic or younger, relatively undeformed lavas due to the fact that low grade terrains are often lost to erosion or overprinted by subsequent metamorphism in older provinces. One exception is the 1.1 Ga North Shore Volcanic Group (NSVG), which is regionally deformed, yet still contains well-developed zeolite facies metamorphic zonation (Schmidt, 1993; Schmidt and Robinson, 1997; Figure 2.1).

The overall structure of the NSVG is a plunging synclinal fold with a hinge axis in the Tofte-Lutsen area (e.g., Miller *et al.*, 2002) dividing the region into two sections; the southwest limb and the northeast limb. Previous studies (e.g. Schmidt, 1993, Schmidt and Robinson, 1997) established a progression of metamorphic mineral assemblages in the southwest limb that range from lower zeolite facies in the uppermost parts of the

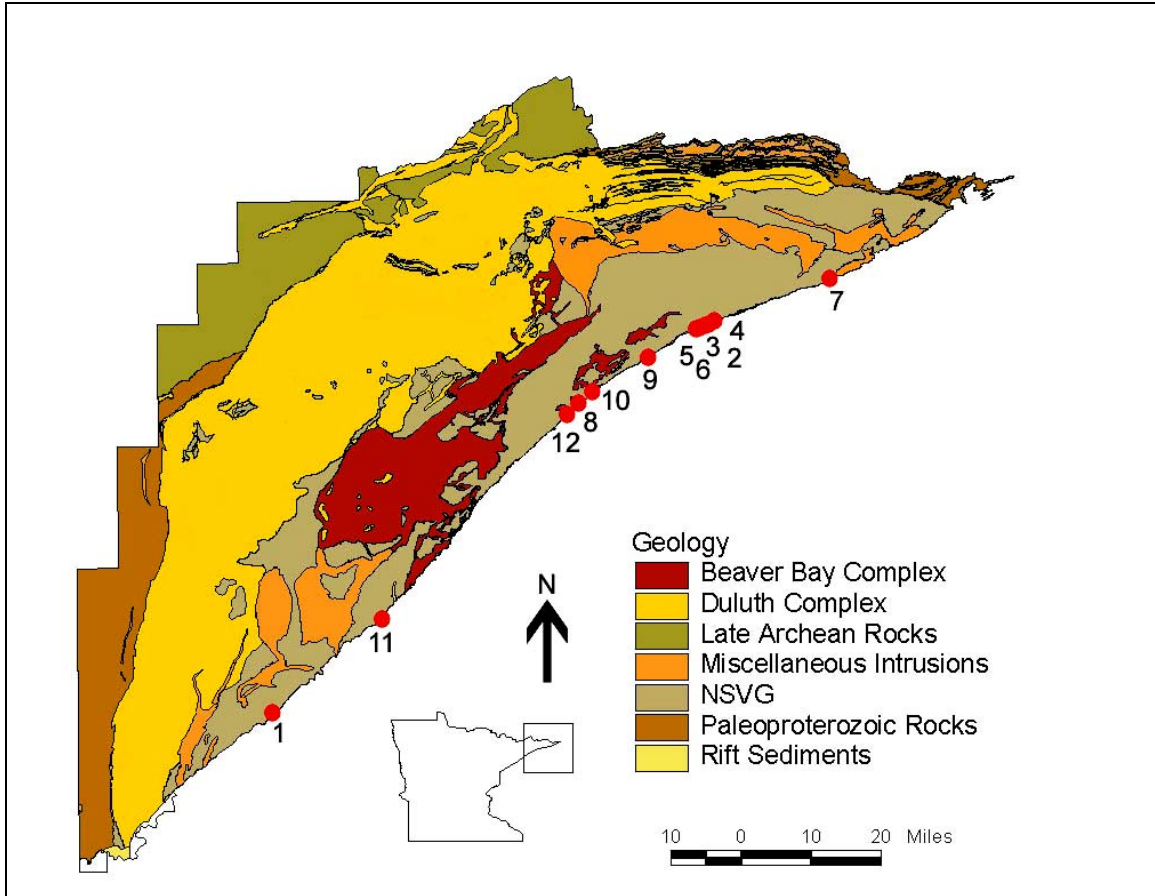


Figure 2.1: Generalized geological map of northeastern Minnesota showing the distribution of the NSVG lavas and associated Keweenaw intrusives (after Miller *et al.*, 2001). Numbered locations (red circles) refer to sampling sites from the present study (cf. Table 2.1).

stratigraphy through greenschist facies rocks in the lowermost lavas near Duluth. There appears to be little previous work on the metamorphism of the northeast limb as assessing the metamorphic history of this part of the province is complicated by the variable lava chemistry, which covers the whole range between rhyolites and olivine normative basalts (BVSP, 1981; Brannon, 1984; Schmidt, 1990; Miller *et al.*, 2002; Boerboom, 2004).

The present study investigates the distribution of metamorphic grade in the NSVG, with a concentration on the alteration present in the northeast limb. Field, petrographic, and analytical studies are combined to assess the variation in metamorphic grade across

the syncline. This data is then used to interpret the conditions and timing of alteration relative to the structural development of this province.

### **Geologic Background**

The most voluminous accumulations of basaltic lava on continental crust are flood basalts, which typically outcrop as thick sections of subhorizontal, subaerial tholeiitic flows (Coffin and Eldholm, 1994; Winter, 2001), such as the basalts of the Keweenaw province associated with the Midcontinent Rift. The Midcontinent rift system (MRS) is a major feature covering over 2,000 km of central North America (Van Schmus and Hinze, 1985; Cannon *et al.*, 1989, Cannon, 1992), extending northeast from Kansas into central Lake Superior and then southeastward through Michigan into Ohio (Green, 1982; Hinze *et al.*, 1997; Ojakangas and Dickas, 2002). The MRS is a product of extension occurring between 1108 and 1094 Ma, which was aborted prior to complete continental rifting due to convergence from the Grenville province allochthon to the east (Cannon, 1994; Allen *et al.*, 1997). Magmatism associated with this extension is believed to originate from a large asthenospheric plume centered below what is now Lake Superior (Vervoort and Green, 1997). The volcanic pile emplaced during magmatism is more than 8 km thick (Ojakangas and Matsch, 1982; Schmidt and Robinson, 1997) with an estimated volume of  $1.3 \times 10^6 \text{ km}^3$  (Hutchinson *et al.*, 1990; Allen *et al.*, 1992). This province is one of the oldest and best preserved large igneous provinces (BVSP, 1981; Boerboom, 2004) with the majority composed of either intrusions or subaerial volcanics later buried by Phanerozoic sedimentary strata (Ojakangas and Dickas, 2002). Surface exposures of the MRS are known only in the Lake Superior region, where a 30 km thick sequence of volcanic and sedimentary rocks composes the Keweenaw Supergroup (e.g., Ojakangas and Dickas, 2002).

The NSVG, a section of the Keweenawan province located in northern Minnesota, covers the extent of the Minnesota shoreline along Lake Superior and can be divided into two sub-basins of gently dipping strata (Vervoort and Green, 1997). These lavas consist mainly of olivine tholeiites with a continuous range of compositions from strongly olivine-phyric tholeiites to rhyolites (BVSP, 1981; Schmidt, 1990; Boerboom, 2004). Magmatism throughout most continental flood basalts is dominantly basaltic with only about 1% of the flows having a felsic composition; within the NSVG, 10% of the southwest limb and 25% of the northeast limb is composed of felsic flows (Vervoort and Green, 1997). It still is unclear if the range in composition is due to large-scale crustal melts or differentiates of more primitive magma (Vervoort and Green, 1997). The structure of the MRS is dominated by extension followed by compression, forming horst and graben structures followed by reverse and, in some cases, transform faulting (Van Schmus and Hinze, 1985; Vervoort and Green, 1997). Geophysical and geological data show that the Lake Superior region is a fault-bounded-asymmetric basin, but the exact structure of the area encompassing the NSVG is still unknown (Van Schmus and Hinze, 1985; Hinze *et al.*, 1997).

The flows of the NSVG are mainly between 1 and 50 m thick (Schmidt and Robinson, 1997), with an average thickness between 5 and 25 m (Schmidt, 1990). In areas where lava flows vary in composition, the morphology of individual flows is characteristic for each major compositional type (Saemundsson, 1979). In the NSVG, the volumetrically dominant olivine tholeiites occur as pahoehoe flows, while other compositions, such as the basaltic andesites occur as aa flows (Schmidt, 1990; Boerboom, 2004). Figure 1.1 shows a cross sectional diagram depicting the general

morphology of a typical aa flow. The upper vesicular zone can take up as much as half of the flow thickness in thinner flows and the flow bottoms are rich in pipe amygdules that often coalesce into inverted Y-shapes (Schmidt, 1990). Pahoehoe flows typically are vesicular throughout the entire thickness. In areas where multiple pahoehoe flows occur in vertical succession, flow boundaries are easily depicted due to the presence of pipe amygdules at the base and classic ropey pahoehoe flow-top characteristics at the top (Figure 2.2).



Figure 2.2: Flow boundary between two vesicular basalt flows at Site 12. Field book (12x19 cm) shown for scale. White curve superimposed on image highlights the flow boundary. Lower arrow points to pahoehoe structures indicative of the flow top of the lower flow, and the upper arrow points to the filled pipe amygdules found at the base of the upper aa flow.

## Methods

Field work was conducted along the North shore of Lake Superior in Minnesota during July 15-26, 2004. Field observations were made at 12 sites (Table 2.1, Figure 2.1). Several sites (3, 4, 6, 11, 12) were selected for detailed mapping at the outcrop scale using standard geologic methods. Photo-mosaics were acquired with a high resolution digital camera for later analysis. Samples for geochemical and digital analysis were collected from outcrops that were representative of the variation in porosity, alteration, mineralogy, and pore types encountered.

A suite of samples representative of the lithologies and mineral parageneses found in the NSVG were selected and used for in depth chemical and digital analysis of the various flow chemistries and alteration histories. In preparation for bulk rock analysis, twelve samples were powdered and sent to the Geosciences Laboratories of Ontario where major element contents were determined by wavelength dispersive X-ray fluorescence (XRF) with a detection limit of 0.01 wt%. Thin sections also were prepared from each sample for detailed petrographic observations of primary and secondary minerals. Petrographic analysis was performed on each thin section to quantify primary porosity and determine mineral parageneses. Mineral chemistry was determined by electron probe microanalysis (EPMA) using an automated JEOL 733A electron microprobe operated at 15 kV accelerating potential and 15 nA beam current. Calibration was conducted using natural geologic standards. Beam width for analysis of hydrous minerals (i.e., clays and zeolites) was 10 to 30  $\mu\text{m}$  to minimize alkali migration (this instrument is outfitted with wide detector slits that allow for large spot size analyses). Raw counts were collected for 20 s (approximately 60 s total beam contact at each point) and converted to oxide weight percents using the CITZAF correction procedure after

Table 2.1: Field study locations in the North Shore Volcanic Group.

| <i>Site</i> | <i>Site Description</i>  | <i>Samples</i>          | <i>Alteration Mineralogy</i>   | <i>Zeolite Zone</i>  |
|-------------|--|-------------------------|--|----------------------|
| 1           | Knife River Wayside<br>N46° 56.849', W91° 47.505'                                | 01                      | Prehnite-pumpellyite facies alteration,<br>laumontite float  | Prehnite-pumpellyite |
| 2           | Cut Face Creek outwash at Wayside<br>N47° 43.854', W90° 26.383'                  | 02                      | Laumontite fault breccia and stilbite-<br>bearing amygdaloidal lava float                          | Laumontite           |
| 3           | Private shoreline southeast of<br>Thomsonite Beach<br>N47° 43.358', W90° 27.076' | 04-10                   | Thomsonite + mesolite alteration   | Thomsonite-Mesolite  |
| 4           | Cut Face Creek<br>N47° 43.887', W90° 26.517'                                     | 11-12,<br>14, 30-<br>31 | Laumontite + chlorite alteration; (also<br>laumontite cemented breccia 2 miles<br>upstream)        | Laumontite           |
| 5           | Streambed to Butterwort Cliffs<br>N47° 43.266', W90° 28.089'                     | 16                      | Laumontite-cemented fault breccia<br>float   | Thomsonite-Mesolite  |
| 6           | Butterwort Cliffs (Cascade River<br>State Park)<br>N47° 43.212', W90° 28.033'    | 13B, 15,<br>17-19       | Thomsonite + mesolite + very minor<br>analcime +/- calcite alteration                              | Thomsonite-Mesolite  |
| 7           | Shoreline southeast of Judge<br>Magney State Park<br>N47° 48.716', W90° 03.999'  | 03                      | Silica + clay + laumontite alteration  | Laumontite           |
| 8           | Tofte Park<br>N47° 34.258', W90° 50.389'   | 20                      | Hydrothermally altered lava with<br>heulandite + scolecite + stilbite +<br>laumontite + thomsonite | Thomsonite-Mesolite  |
| 9           | Lutsen Grandview Park<br>N47° 39.568', W90° 38.349'                              | 21                      | Thomsonite + mesolite + analcime   | Analcime             |
| 10          | Roadcut along Hwy 61<br>N47° 35.536', W90° 48.071'                               | 22                      | Andesite (?) with laumontite   | Thomsonite-Mesolite  |
| 11          | Gooseberry Falls State Park<br>N47° 08.286', W91° 27.520'                        | 23-29                   | Chlorite + calcite + stilbite +<br>Laumontite alteration   | Laumontite           |
| 12          | Temperance River State Park<br>N47° 33.076', W90° 52.560'                        | 32-38                   | Stilbite + heulandite + quartz + chlorite<br>+ thomsonite alteration                               | Stilbite-heulandite  |

accounting for unanalyzed oxygen following the methods of Tingle *et al.* (1996). The analytical conditions and correction procedures employed have previously been shown to provide analyses of zeolites and clays that are within error of compositions determined by other methods (Tingle *et al.*, 1996).

## **Results**

Field observations indicate that low-grade secondary mineral assemblages are well-preserved through most of the NSVG. Alteration mineralogy is easily observed in the field as vesicle infillings in the high porosity zones. Vesicles typically show complete infilling with various zeolite minerals, and, in some cases, are initially lined with clay or silica rims. The lava matrix, in both the high and low porosity zones, appears to have also undergone alteration. This matrix alteration shows some zeolitization, but is dominated by clay and iron oxide alteration minerals. The secondary minerals present in these lavas are similar to those previously observed in tholeiitic lava sequences (e.g., Walker, 1960; Neuhoff, 1997, 2000), ranging from lower zeolite facies through greenschist facies alteration.

### **Primary Basalt Composition and Mineralogy**

Sampled lavas show compositional variations consistent with previous studies of this province (e.g., Schmidt, 1993; Schmidt and Robinson, 1997). Whole rock compositions for selected samples are shown in Table 2.2 and the total alkali-silica diagram of Figure 2.3. Most of the lavas were olivine-normative basalts, with a few from the northeast limb exhibiting more evolved basaltic andesite and dacitic compositions.

Table 2.2: Whole-rock chemical compositions (wt %) of samples.

| Sample                                      | NS04-03 | NS04-05 | NS04-10 | NS04-14B | NS04-15 | NS04-19 | NS04-21 | NS04-25 | NS04-29 | NS04-31 | NS04-37 | NS04-38 |
|---|---------|---------|---------|----------|---------|---------|---------|---------|---------|---------|---------|---------|
| Site <sup>a</sup>                           | 8       | 3       | 3       | 4        | 7       | 7       | 10      | 12      | 11      | 4       | 13      | 13      |
| SiO <sub>2</sub>                            | 66.87   | 44.96   | 45.05   | 55.51    | 45.4    | 46.82   | 45.28   | 43.29   | 48.66   | 46.62   | 46.59   | 44.92   |
| TiO <sub>2</sub>                            | 1.28    | 1.14    | 1.08    | 2.17     | 1.2     | 1.24    | 1.08    | 1.31    | 0.74    | 1.15    | 1.12    | 1.07    |
| Al <sub>2</sub> O <sub>3</sub>              | 9.42    | 16.8    | 15.5    | 12.15    | 15.67   | 15.88   | 16.35   | 15.31   | 16.04   | 16.86   | 16      | 15.73   |
| Fe <sub>2</sub> O <sub>3</sub> <sup>b</sup> | 12.6    | 9.98    | 9.68    | 13.45    | 10.02   | 10.56   | 9.08    | 10.97   | 6.86    | 10.26   | 9.8     | 9.53    |
| MnO   | 0.1     | 0.13    | 0.15    | 0.24     | 0.16    | 0.17    | 0.14    | 0.16    | 0.17    | 0.16    | 0.16    | 0.14    |
| MgO   | 1.5     | 7.48    | 9.26    | 3.58     | 8.5     | 9.41    | 8.4     | 7.44    | 6.87    | 7.98    | 7.89    | 8.31    |
| CaO   | 2.06    | 7.9     | 7.07    | 3.48     | 8.42    | 6.17    | 7.92    | 9.58    | 6.82    | 9.68    | 9.05    | 8.83    |
| Na <sub>2</sub> O                           | 3.59    | 3.66    | 3.3     | 3.83     | 2.58    | 4.03    | 2.84    | 2.23    | 2.54    | 2.27    | 2.12    | 1.92    |
| K <sub>2</sub> O                            | 0.49    | 0.14    | 0.07    | 1.64     | 0.73    | 0.22    | 0.8     | 0.27    | 0.25    | 0.28    | 0.45    | 0.41    |
| P <sub>2</sub> O <sub>5</sub>               | 0.39    | 0.12    | 0.11    | 0.44     | 0.12    | 0.12    | 0.12    | 0.14    | 0.05    | 0.12    | 0.13    | 0.13    |
| LOI   | 2.48    | 8.16    | 9.03    | 3.94     | 7.24    | 5.92    | 8.11    | 8.69    | 10.55   | 4.56    | 6.98    | 8.86    |
| Total                                       | 100.78  | 100.47  | 100.3   | 100.43   | 100.04  | 100.54  | 100.12  | 99.39   | 99.55   | 99.94   | 100.29  | 99.85   |

<sup>a</sup>Site descriptions given in Table 2.1, and locations shown on Figure 2.1. <sup>b</sup>Total Fe reported as Fe<sub>2</sub>O<sub>3</sub>.

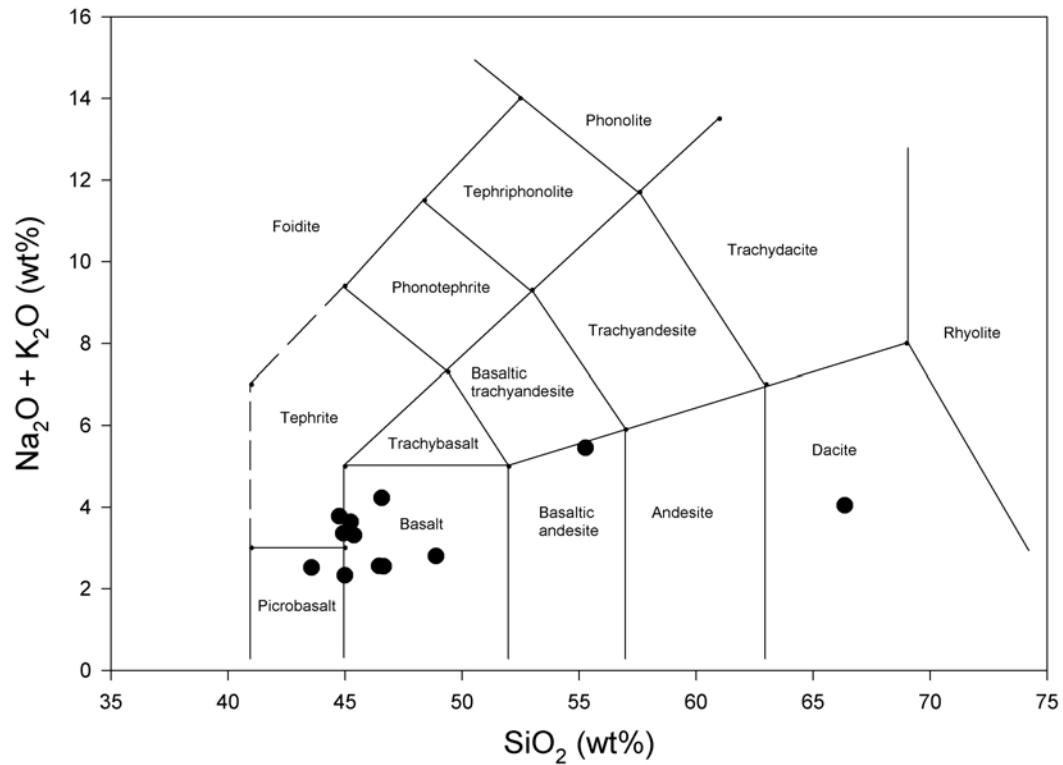


Figure 2.3: Total alkalis-silica diagram showing compositional ranges of NSVG basalts sampled in this study (black circles). Some of the collected samples are more evolved basaltic andesites and dacites, while the majority of samples are olivine-phyric basalts and picrobasalts.

Matrix alteration of the primary magmatic phases is observed to varying degrees in all of the analyzed samples. There was no glass, mesostasis or olivine observed in any of the samples, most likely due to alteration. Feldspar and pyroxene compositions within the lavas varied throughout each sample, and these variations showed no significant correlation to compositional variations of the lavas. The feldspar compositions (Table 2.3) range from  $Ab_{23}An_{72}Or_5$  to  $Ab_{99.5}An_{0.3}Or_{0.2}$ . The near-end member albite compositions observed in some plagioclase phenocrysts suggests that they have been subject to secondary albitization. Clinopyroxenes are present, with representative compositions shown in Table 2.4; the absence of orthopyroxenes could also be attributed to the alteration of each sample.

Table 2.3: Representative compositions of plagioclase.

| Sample                                     | NS04-03 | NS04-29B | NS04-05 | NS04-19 | NS04-10A | NS04-25 | NS04-38 | NS04-31A |
|--|---------|----------|---------|---------|----------|---------|---------|----------|
| <i>Oxide weight %</i>                      |         |          |         |         |          |         |         |          |
| SiO <sub>2</sub>                           | 68.46   | 69.28    | 61.79   | 49.73   | 45.73    | 53.84   | 53.20   | 48.62    |
| TiO <sub>2</sub>                           | 0.04    | 0.03     | 0.05    | 0.04    | 0.02     | 0.11    | 0.10    | 0.10     |
| Al <sub>2</sub> O <sub>3</sub>             | 19.55   | 19.94    | 19.01   | 17.91   | 25.15    | 27.74   | 29.64   | 31.79    |
| FeO <sup>a</sup>                           | 0.05    | 0.09     | 0.76    | 7.01    | 0.33     | 0.87    | 0.62    | 0.75     |
| MnO  | 0.00    | 0.01     | 0.02    | 0.16    | 0.00     | 0.02    | 0.00    | 0.03     |
| Cr <sub>2</sub> O <sub>3</sub>             | 0.04    | 0.02     | 0.04    | 0.01    | 0.03     | 0.05    | 0.05    | 0.03     |
| MgO  | 0.00    | 0.13     | 2.36    | 11.53   | 0.27     | 0.36    | 0.24    | 0.18     |
| CaO  | 0.06    | 0.58     | 1.26    | 1.56    | 8.14     | 10.93   | 13.02   | 14.66    |
| Na <sub>2</sub> O                          | 12.28   | 11.99    | 9.37    | 4.13    | 5.89     | 5.04    | 4.13    | 3.12     |
| K <sub>2</sub> O                           | 0.03    | 0.11     | 0.47    | 1.43    | 0.04     | 0.32    | 0.12    | 0.12     |
| Total                                      | 100.50  | 102.18   | 95.14   | 93.52   | 85.59    | 99.26   | 101.12  | 99.41    |
| <i>Anhydrous formula units<sup>b</sup></i> |         |          |         |         |          |         |         |          |
| Si   | 2.98    | 2.97     | 2.87    | 2.41    | 2.42     | 2.46    | 2.39    | 2.24     |
| Ti   | 0.00    | 0.00     | 0.00    | 0.00    | 0.00     | 0.00    | 0.00    | 0.00     |
| Al   | 1.00    | 1.01     | 1.04    | 1.05    | 1.57     | 1.49    | 1.57    | 1.73     |
| Fe   | 0.00    | 0.00     | 0.03    | 0.33    | 0.01     | 0.03    | 0.02    | 0.03     |
| Mn   | 0.00    | 0.00     | 0.00    | 0.01    | 0.00     | 0.00    | 0.00    | 0.00     |
| Cr   | 0.00    | 0.00     | 0.00    | 0.00    | 0.00     | 0.00    | 0.00    | 0.00     |
| Mg   | 0.00    | 0.01     | 0.17    | 0.97    | 0.02     | 0.02    | 0.02    | 0.01     |
| Ca   | 0.00    | 0.03     | 0.06    | 0.09    | 0.46     | 0.54    | 0.63    | 0.73     |
| Na   | 1.04    | 1.00     | 0.84    | 0.42    | 0.60     | 0.45    | 0.36    | 0.28     |
| K  | 0.00    | 0.01     | 0.03    | 0.01    | 0.00     | 0.02    | 0.01    | 0.01     |
| <i>Mole %</i>                              |         |          |         |         |          |         |         |          |
| Ab   | 99.57   | 96.80    | 89.53   | 80.70   | 56.50    | 44.67   | 36.20   | 27.60    |
| An   | 0.27    | 2.60     | 6.80    | 17.25   | 43.23    | 53.47   | 63.10   | 71.65    |
| Or   | 0.17    | 0.60     | 3.68    | 2.05    | 0.27     | 1.87    | 0.70    | 0.75     |

<sup>a</sup>Total Fe reported as FeO. <sup>b</sup>Based on 8 oxygen charge equivalents.

Table 2.4: Representative compositions of pyroxenes.

| Sample                                     | NS04-10A | NS04-10A | NS04-14B | NS04-15C | NS04-15C | NS04-37 | NS04-37 |
|--|----------|----------|----------|----------|----------|---------|---------|
| <i>Oxide weight %</i>                      |          |          |          |          |          |         |         |
| SiO <sub>2</sub>                           | 49.16    | 49.76    | 50.27    | 51.53    | 52.66    | 51.13   | 50.03   |
| TiO <sub>2</sub>                           | 1.54     | 1.93     | 0.77     | 1.32     | 0.67     | 1.66    | 1.63    |
| Al <sub>2</sub> O <sub>3</sub>             | 4.70     | 3.73     | 1.31     | 1.90     | 2.50     | 4.45    | 3.08    |
| FeO <sup>a</sup>                           | 10.11    | 10.07    | 21.10    | 13.47    | 6.83     | 10.28   | 12.68   |
| MnO  | 0.22     | 0.22     | 0.50     | 0.33     | 0.17     | 0.20    | 0.20    |
| Cr <sub>2</sub> O <sub>3</sub>             | 0.28     | 0.14     | 0.05     | 0.02     | 0.60     | 0.26    | 0.22    |
| MgO  | 13.40    | 14.16    | 10.38    | 15.67    | 16.42    | 12.96   | 12.17   |
| CaO  | 18.85    | 19.76    | 15.82    | 16.09    | 20.83    | 20.79   | 20.18   |
| Na <sub>2</sub> O                          | 0.52     | 0.35     | 0.22     | 0.33     | 0.30     | 0.32    | 0.32    |
| K <sub>2</sub> O                           | 0.02     | 0.01     | 0.01     | 0.03     | 0.05     | 0.00    | 0.01    |
| Total                                      | 98.79    | 100.14   | 100.43   | 100.69   | 101.04   | 102.05  | 100.53  |
| <i>Anhydrous formula units<sup>b</sup></i> |          |          |          |          |          |         |         |
| Si   | 3.72     | 3.72     | 3.90     | 3.84     | 3.84     | 3.75    | 3.77    |
| Ti   | 0.09     | 0.11     | 0.04     | 0.07     | 0.04     | 0.09    | 0.09    |
| Al   | 0.42     | 0.33     | 0.12     | 0.17     | 0.22     | 0.38    | 0.27    |
| Fe   | 0.64     | 0.63     | 1.37     | 0.84     | 0.42     | 0.63    | 0.80    |
| Mn   | 0.01     | 0.01     | 0.03     | 0.02     | 0.01     | 0.01    | 0.01    |
| Cr   | 0.02     | 0.01     | 0.00     | 0.00     | 0.03     | 0.01    | 0.01    |
| Mg   | 1.51     | 1.58     | 1.20     | 1.74     | 1.79     | 1.42    | 1.37    |
| Ca   | 1.53     | 1.58     | 1.31     | 1.29     | 1.63     | 1.63    | 1.63    |
| Na   | 0.08     | 0.05     | 0.03     | 0.05     | 0.04     | 0.05    | 0.05    |
| K  | 0.00     | 0.00     | 0.00     | 0.00     | 0.00     | 0.00    | 0.00    |
| <i>Mole %</i>                              |          |          |          |          |          |         |         |
| Wo   | 41.60    | 41.77    | 33.87    | 33.23    | 42.53    | 44.40   | 42.93   |
| En   | 41.03    | 41.63    | 30.90    | 45.07    | 46.60    | 38.50   | 36.03   |
| Fs   | 17.37    | 16.63    | 35.23    | 21.73    | 10.87    | 17.13   | 21.03   |

<sup>a</sup>Total Fe reported as FeO. <sup>b</sup>Based on 12 oxygen charge equivalents.

### **Regional Alteration Mineralogy**

Although flow morphologies and textures are well-preserved throughout the study area, all investigated lava flows exhibit some degree of secondary mineral alteration. In contrast to typical alteration patterns in younger very low-grade metabasalts, alteration is present even in areas away from zones of high primary porosity and is clearly observed in hand specimen. Within the matrix, the primary magmatic phases are usually replaced by secondary alteration minerals such as Fe(Ti) oxides, mafic phyllosilicates, zeolites, and occasionally silica minerals and calcite. The alteration mineralogy observed within vesicles is dominated by zeolite minerals, with occasional linings of silica and mafic phyllosilicates and overprinting by calcite.

The extent of chemical alteration within the matrix is typically greater within zones of high primary porosity (e.g., vesicular flow tops and bottoms) than in massive flow centers. In some samples there is a strong presence of sub-mm sized spots of bright red Fe(III) oxides (probably hematite), and in most cases oxide alteration occurs further away from amygdules than the mafic phyllosilicates and zeolites. Mafic phyllosilicates often are pervasive around vesicles as replacements of mesostasis, glass, and olivine, and also are commonly found lining pore walls. Plagioclase is variably replaced in vesicular zones by either near-end member albite or zeolites, and zeolite alteration within the matrix dominantly occurs in close proximity to amygdules also filled with zeolites. Often the only phenocryst phase that escapes alteration in these zones is clinopyroxene. The overall extent of this alteration appears to be a function of distance from primary porosity, and in some samples (Figure 2.4) light-colored reaction aureoles are observed as bleached haloes (probably due to oxidation reactions) around and between primary pores within the rock.



Figure 2.4: Field photo from Site 3 (Table 2.1) showing an extensively altered pahoehoe flow. Visible within the flow are bleached haloes around vesicles connected by thin anastomosing bleached areas. Pencil shown for scale.

Primary vesicles, especially in zones of relatively high porosity at the tops and bottoms of flows, are generally completely filled with zeolites and occasional linings of silica and mafic phyllosilicate minerals. Some vesicles undergo complete infilling with only one zeolite mineral, as shown by the thomsonite filled vesicle in Figure 2.5A. Many other vesicles show multiple stages of zeolite alteration and contain two or more zeolite minerals. Figure 2.5B shows a vesicle filled with thomsonite and mesolite, and the vesicle in Figure 2.5C contains analcime, thomsonite and mesolite. Some vesicle walls are rimmed by secondary minerals prior to zeolite infilling. Silica minerals are the first to form where present, as shown in Figure 2.5D. This amygdule exhibits early lining of silica, followed by a thin clay layer before complete infilling of laumontite. Most often the vesicle walls are lined only with mafic phyllosilicates prior to zeolite infilling, as shown in Figure 2.5E where chlorite rims precede laumontite infilling.

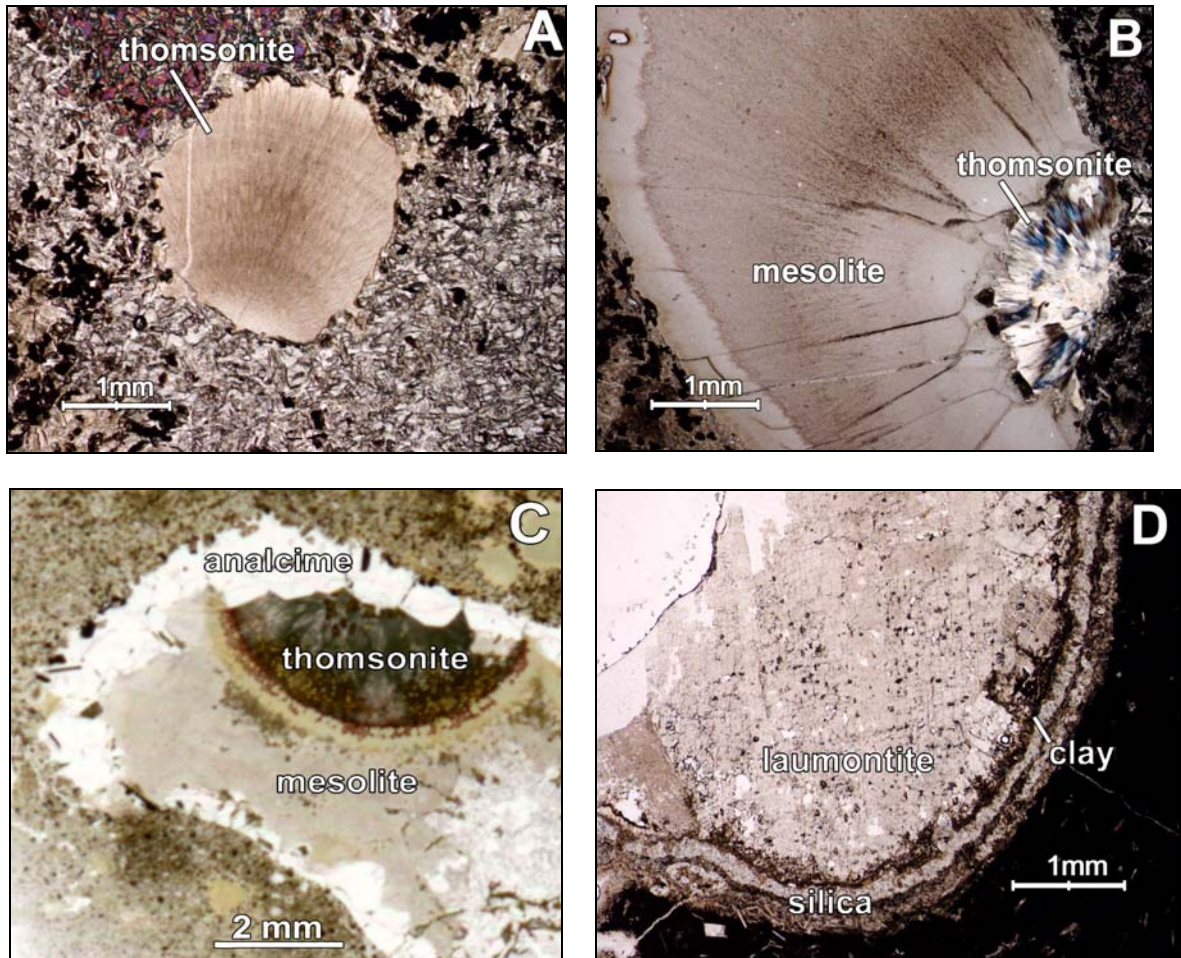


Figure 2.5: Secondary alteration in NSVG lavas. All photomicrographs were taken through partially crossed polars. A) Photomicrograph showing thomsonite alteration in sample NS04-31, collected directly above the sediment pile roadcut from Site 4 (Table 2.1). B) Photomicrograph of sample NS04-15 showing the thomsonite-mesolite alteration typical of Sites 3 and 6. C) Scanned image of thin section of sample NS04-15 showing analcime-thomsonite (thom.)-mesolite alteration. D) Photomicrograph of sample NS04-03 showing laumontite alteration typical of sample sites 4 and 7 with clearly-defined early silica and clay (rims on vesicles. E) Photomicrograph of sample NS04-14 showing laumontite alteration with initial formation of chlorite rims. F) Photomicrograph of sample NS04-10A highlighting calcite crystallization in thomsonite filled amygdule.

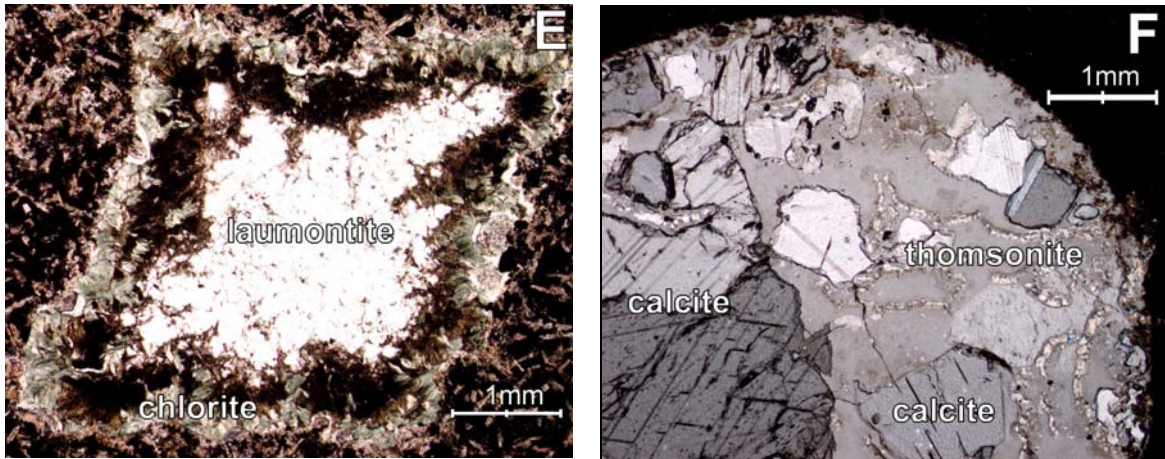


Figure 2.5: (continued)

Quartz and calcite are widespread throughout the study area, though not necessarily pervasive. Local, late-stage alteration that cross-cuts and, in some cases overprints these assemblages, is observed around veins and faults. Veins in these localities often contain quartz and calcite, along with laumontite, stilbite, and/or heulandite. Silica occasionally is present as initial pore linings, but most often is present within the matrix, while calcite dominantly is found as post-zeolite infillings of amygdules. Figure 2.5D shows an amygdule exhibiting early linings along the pore wall of quartz and interlayered chlorite/smectite, followed by complete zeolite infilling of residual pore space. The progression of mineralization within this depicted pore is typical of pores exhibiting silica linings. Figure 2.5F shows an amygdule filled with thomsonite that has experienced late calcite overprinting. The amygdules within a given sample that have experienced this late calcite overprinting appear to be randomly distributed.

Four distinct zeolite assemblages are observed within the lavas of the northeast limb of the study area. Mineral zones containing these assemblages are identified based on the presence of the index minerals analcime, thomsonite-mesolite, stilbite-heulandite, and laumontite within vesicles. In all cases, these zones are present in contiguous

sections of the NSVG, and, except for the stilbite-heulandite zone, are present in both limbs. Most of the isograds bounding these zones are not well-exposed, and their locations are approximate. Alteration higher in metamorphic grade than zeolite facies is present only in the very southern portion of the field area where alteration reached prehnite-pumpellyite and greenschist facies, and has already been discussed in detail by Schmidt (1993) and Schmidt and Robinson (1997).

The mineralogy of the four distinct zeolite zones is described below:

#### **Laumontite zone lavas**

Laumontite zone alteration is the highest zeolite grade alteration observed in the NSVG lavas, and is characterized by the presence of quartz, interlayered chlorite/smectite (c/s), and laumontite. The alteration zone was observed in two locations along the shoreline, from just south of Grand Marais to Grand Portage and from Little Marais to just south of Two Harbors. Albitized plagioclase laths and altered mesostasis dominate the matrix, and there are very minor amounts of unaltered pyroxene phenocrysts. Alteration affects most of the matrix and consists of c/s, quartz and iron oxides.

Quartz rims within amygdules are occasionally present where they precede rims of C/S (Figure 2.5D). Occasionally, C/S is visible in hand sample, and appears in thin section as a green fibrous mineral within vesicles. Smaller vesicles within these lavas are completely filled with c/s, while larger vesicles are rimmed with C/S and later filled with laumontite. Laumontite appears white in hand sample, and in thin section appears either blocky or fibrous depending on the orientation of the thin section to the fibrous mineral growth habit. Overprinting of laumontite with calcite is occasionally observed in the vesicles. The calcite exhibits twinning and, in most cases, rhombohedral crystal habit.

**Stilbite-heulandite zone lavas**

Stilbite-heulandite zone alteration is recognized in the NSVG lavas by the presence of amygdules filled with stilbite and/or heulandite. Unlike the other zeolite zones present along the NSVG, this zone was not found in the northeast limb. During this study it was only observed once along the southwest limb between the towns Little Marais and Tofte (and was observed by Schmidt (1993) in several localities in this area). Iron oxides, chlorite, albitized plagioclase laths and minor amounts of unaltered pyroxene phenocrysts dominate the lava matrix.

Trioctahedral smectite is present either as rims along vesicle walls or as complete infilling of vesicles. Smaller vesicles are completely filled with trioctahedral smectite, while in larger vesicles it is present as rims with the remaining open space filled with calcite. The calcite exhibits twinning and in some instances rhombohedral cleavage. It is possible that calcite occurs as overprinting of the original zeolites that filled the vesicles in these analyzed samples, as stilbite and heulandite were observed as vesicle infillings in the field.

**Thomsonite-mesolite zone lavas**

Lavas exhibiting amygdules filled with thomsonite, mesolite and C/S interlayered clays comprise this alteration zone observed in the NSVG. This zone of alteration occurred to the northeast and to the southwest of Lutsen, bounding the analcime zone discussed below. Pyroxene phenocrysts, plagioclase laths, and iron oxides dominate the lava matrix surrounding the vesicles. The pyroxene phenocrysts often are unaltered, whereas plagioclase is typically replaced by zeolites similar to those observed in vesicles. Amygdule minerals in hand samples are occasionally green in color, but are dominantly

either pink or white with dark-pink color bands. In thin section, the minerals appear colorless to white, with brown staining sometimes present around the rim of the vesicle.

There are two dominant crystallization habits of thomsonite and mesolite in the vesicles of this zone. In vesicles where there is a prevalent crystallization sequence of early thomsonite pore rims followed by late mesolite filling of remaining pore space, the thomsonite occurs as a massive growth of many small fibrous bundles rimming the vesicle wall, or in some rare occurrences completely filling the vesicle. Mesolite appears either massive with no crystal habit, or fibrous and fills any remaining space after the thomsonite rims in vesicles. The second dominant crystallization habit originates at some apparently random nucleation point along the vesicle wall and grows radially outward until the vesicle is completely filled (Figure 2.5B). The growth sequence is usually continuous from thomsonite originating at the nucleation site transitioning into mesolite with no visible boundary between the two; in amygdules where there is a clearly defined boundary between the thomsonite and mesolite, one, if not both minerals, exhibit a fibrous growth habit. In all vesicles observed in this zone, the relative amounts of these two minerals vary inconsistently. Also, clays are not present as rims along the vesicle wall, but they do occasionally exist as intergrowths of interlayered chlorite-smectites within the zeolite minerals, and in a majority of the amygdules, there is a late overprinting of calcite, with crystals exhibiting twinning and rhombohedral cleavage (Figure 2.5F).

### **Analcime zone lavas**

This alteration zone in the NSVG lavas is characterized by the presence of thomsonite and analcime within vesicles. This is the lowest grade of alteration observed in the field area, and is found only in the vicinity of Lutsen. Unaltered pyroxene

phenocrysts, albitized plagioclase laths, and iron oxides, with occasional zones of thomsonite alteration, dominate the lava matrix. No visible clay or silica rims were observed lining vesicle walls. The amygdule minerals appear pink to colorless in hand sample and clear in thin section. There is usually a sequence of mineralization from thomsonite rimming the vesicle to analcime growth in the residual open space. The thomsonite crystallization habit ranges from a massive growth of many small fibrous bundles rimming the pore, to one or two large fibrous bundles individually filling up to half of the vesicle, while the analcime exhibits a blocky habit. The relative amount of each mineral varies between vesicles, and in some instances the crystallization sequence is ambiguous.

#### **Alteration Mineral Chemistry**

Representative compositions of analyzed mafic phyllosilicates are listed in Table 2.5 and are plotted in Figure 2.6 in terms of the sum of Si + Al + Mg + Fe and the interlayer charge ( $2\text{Ca} + \text{Na} + \text{K}$ ). The bulk of the samples have compositions intermediate between trioctahedral smectites and chlorites, suggesting that they are interlayered chlorite/smectite phases. These samples are found in the thomsonite-mesolite and laumontite alteration zones. Samples representative of the stilbite-heulandite alteration zone are dominantly trioctahedral smectites, although some compositions are mixtures of dioctahedral and trioctahedral smectites. One last group exhibits compositions with  $(2\text{Ca} + \text{Na} + \text{K})$  greater than 1.5 per 28 O equivalents and lie along an extension of the trioctahedral smectite-chlorite mixing trend. These samples are mainly from the thomsonite-mesolite alteration zone, and may be altered celadonite (c.f. Neuhoff et al., 1999).

Table 2.5: Representative compositions of mafic phyllosilicates.

| Sample                                     | NS04-03 | NS04-19 | NS04-25 | NS04-37 | NS04-37 | NS04-37 | NS04-38 |
|--|---------|---------|---------|---------|---------|---------|---------|
| <i>Oxide weight %</i>                      |         |         |         |         |         |         |         |
| SiO <sub>2</sub>                           | 36.40   | 33.39   | 47.99   | 5.62    | 49.45   | 57.85   | 50.27   |
| TiO <sub>2</sub>                           | 0.47    | 0.00    | 0.04    | 19.82   | 0.01    | 0.03    | 0.02    |
| Al <sub>2</sub> O <sub>3</sub>             | 12.61   | 15.93   | 9.21    | 2.33    | 8.08    | 23.47   | 8.05    |
| FeO <sup>a</sup>                           | 10.69   | 12.36   | 2.48    | 58.96   | 0.79    | 0.55    | 0.69    |
| MnO  | 0.25    | 0.46    | 0.15    | 0.32    | 0.18    | 0.07    | 0.19    |
| Cr <sub>2</sub> O <sub>3</sub>             | 0.01    | 0.01    | 0.04    | 0.04    | 0.02    | 0.05    | 0.04    |
| MgO  | 18.24   | 24.19   | 24.30   | 2.51    | 28.04   | 6.58    | 28.33   |
| CaO  | 1.90    | 1.21    | 3.90    | 1.11    | 3.45    | 3.68    | 3.26    |
| Na <sub>2</sub> O                          | 0.15    | 0.04    | 0.05    | 0.57    | 0.04    | 0.05    | 0.05    |
| K <sub>2</sub> O                           | 0.08    | 0.01    | 0.05    | 0.06    | 0.01    | 0.12    | 0.01    |
| Total                                      | 80.80   | 87.59   | 88.22   | 91.34   | 90.07   | 92.45   | 90.92   |
| <i>Anhydrous formula units<sup>b</sup></i> |         |         |         |         |         |         |         |
| Si   | 7.58    | 6.53    | 8.61    | 1.56    | 8.68    | 9.44    | 8.72    |
| Ti   | 0.07    | 0.00    | 0.01    | 4.17    | 0.00    | 0.00    | 0.00    |
| Al   | 3.10    | 3.67    | 1.96    | 0.76    | 1.67    | 4.51    | 1.65    |
| Fe   | 1.86    | 2.02    | 0.38    | 13.77   | 0.12    | 0.07    | 0.10    |
| Mn   | 0.04    | 0.08    | 0.02    | 0.08    | 0.03    | 0.01    | 0.03    |
| Cr   | 0.00    | 0.00    | 0.01    | 0.01    | 0.00    | 0.01    | 0.00    |
| Mg   | 5.67    | 7.06    | 6.64    | 1.04    | 7.33    | 1.60    | 7.33    |
| Ca   | 0.42    | 0.25    | 0.76    | 0.33    | 0.65    | 0.64    | 0.61    |
| Na   | 0.06    | 0.01    | 0.02    | 0.31    | 0.01    | 0.01    | 0.02    |
| K  | 0.02    | 0.00    | 0.01    | 0.02    | 0.00    | 0.03    | 0.00    |
| SAMF <sup>c</sup>                          | 18.21   | 19.29   | 17.59   | 17.13   | 17.80   | 15.62   | 17.80   |
| 2Ca+Na+K                                   | 0.93    | 0.52    | 1.55    | 0.99    | 1.32    | 1.33    | 1.23    |

<sup>a</sup>Total Fe reported as FeO. <sup>b</sup>Based on 28 oxygen charge equivalents. <sup>c</sup>Sum of Si + Al + Mg + Fe in formula unit.

Zeolite compositions generally agree well with previous reported values.

Representative thomsonite compositions are listed in Table 2.6. Thomsonites span the entire compositional range found in this mineral (between Ca<sub>1.5</sub>Na<sub>1.5</sub>Al<sub>4.5</sub>Si<sub>5.5</sub>O<sub>20</sub>·nH<sub>2</sub>O and Ca<sub>2</sub>NaAl<sub>5</sub>Si<sub>5</sub>O<sub>20</sub>·nH<sub>2</sub>O; Ross *et al.*, 1992; Neuhoff and Ruhl, 2006; Figure 2.7) with some samples exhibiting compositions less Ca-Al-rich than previously observed in this

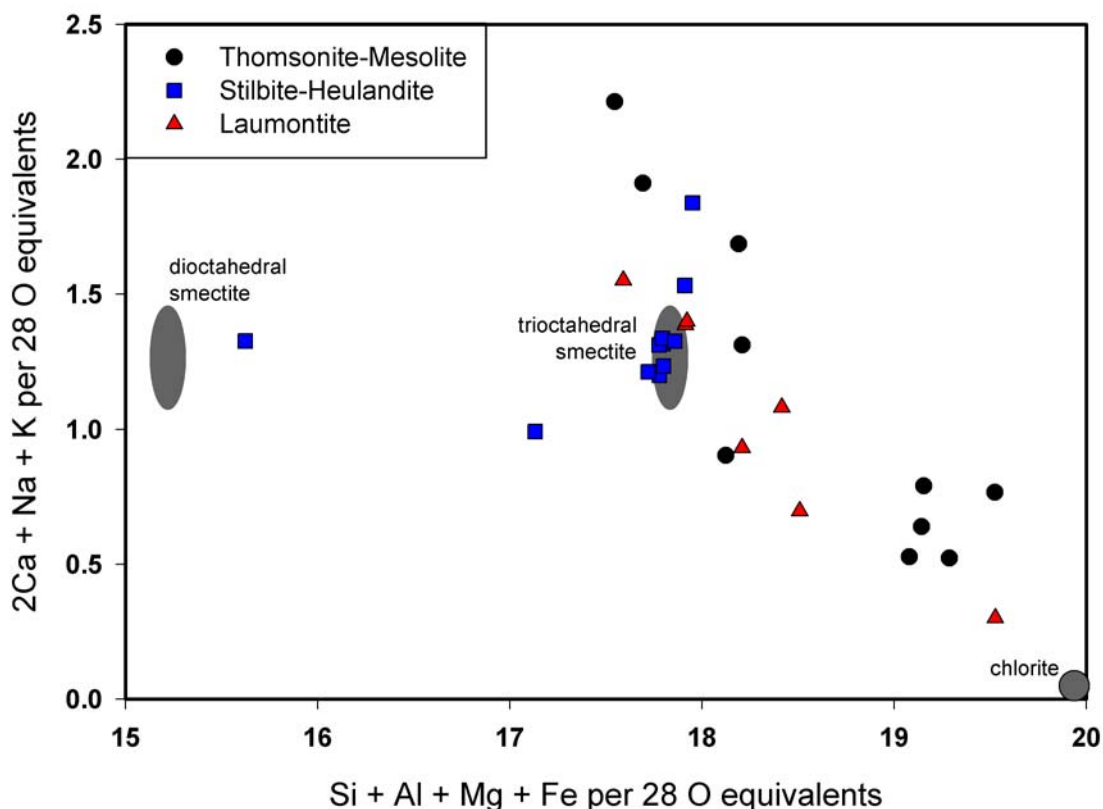


Figure 2.6: Compositions of mafic phyllosilicates formed during regional metamorphism of the NSVG as a function of the number of non-interlayer cations ( $\text{Si} + \text{Al} + \text{Mg} + \text{Fe}$ ) versus the interlayer charge ( $2\text{Ca} + \text{Na} + \text{K}$ ). Sample compositions were normalized to 28 O charge equivalents for comparison. Gray areas show the positions of ideal endmember dioctahedral and trioctahedral smectites and chlorite. The variation in zeolite zone alteration with relation to composition is depicted by the black circles (thomsonite-mesolite), blue squares (stilbite-heulandite), or red triangles (laumontite).

mineral. Mesolite and laumontite (Table 2.7) are essentially stoichiometric. Analcime compositions have Si/Al ratios close to 2.0 (Table 2.7), similar to other occurrences in low grade metabasalts (e.g., Passaglia and Sheppard, 2001; Neuhoﬀ *et al.*, 2006).

## Discussion

### Regional variation of metamorphic grade

One of the difficulties encountered in assessing metamorphic grade in continental flood basalts is that the lavas are frequently overprinted by small-scale hydrothermal systems associated with local intrusions and faults. Indeed, a number of sites visited in

Table 2.6: Representative compositions of thomsonites.

| Sample                                     | NS04-05 | NS04-10A | NS04-15C | NS04-21 | NS04-31A |
|--|---------|----------|----------|---------|----------|
| <i>Oxide weight %</i>                      |         |          |          |         |          |
| SiO <sub>2</sub>                           | 35.75   | 37.09    | 39.25    | 37.02   | 43.35    |
| TiO <sub>2</sub>                           | 0.06    | 0.01     | 0.02     | 0.04    | 0.00     |
| Al <sub>2</sub> O <sub>3</sub>             | 30.07   | 30.66    | 30.69    | 30.84   | 28.01    |
| FeO <sup>a</sup>                           | 0.07    | 0.21     | 0.18     | 0.08    | 0.00     |
| MnO  | 0.00    | 0.00     | 0.02     | 0.01    | 0.01     |
| Cr <sub>2</sub> O <sub>3</sub>             | 0.00    | 0.02     | 0.04     | 0.02    | 0.00     |
| MgO  | 0.22    | 0.47     | 0.00     | 0.21    | 0.00     |
| CaO  | 12.96   | 13.22    | 12.53    | 13.03   | 10.48    |
| Na <sub>2</sub> O                          | 4.00    | 3.78     | 4.44     | 4.13    | 5.44     |
| K <sub>2</sub> O                           | 0.01    | 0.02     | 0.04     | 0.03    | 0.01     |
| Total                                      | 83.14   | 85.48    | 87.19    | 85.41   | 87.31    |
| <i>Anhydrous formula units<sup>b</sup></i> |         |          |          |         |          |
| Si   | 5.00    | 5.04     | 5.20     | 5.03    | 5.68     |
| Ti   | 0.01    | 0.00     | 0.00     | 0.01    | 0.00     |
| Al   | 4.96    | 4.91     | 4.79     | 4.94    | 4.32     |
| Fe   | 0.01    | 0.02     | 0.02     | 0.01    | 0.00     |
| Mn   | 0.00    | 0.00     | 0.00     | 0.00    | 0.00     |
| Cr   | 0.00    | 0.00     | 0.01     | 0.00    | 0.00     |
| Mg   | 0.05    | 0.10     | 0.00     | 0.04    | 0.00     |
| Ca   | 1.94    | 1.92     | 1.78     | 1.90    | 1.47     |
| Na   | 1.08    | 0.99     | 1.14     | 1.09    | 1.38     |
| K  | 0.00    | 0.00     | 0.01     | 0.01    | 0.00     |
| Si/Al                                      | 1.01    | 1.03     | 1.09     | 1.02    | 1.31     |
| Ca/(Ca+Na+K)                               | 0.64    | 0.66     | 0.61     | 0.63    | 0.52     |
| Na/(Ca+Na+K)                               | 0.36    | 0.34     | 0.39     | 0.36    | 0.48     |

<sup>a</sup>Total Fe reported as FeO. <sup>b</sup>Based on 20 oxygen charge equivalents.

this study (e.g., Sites 3, 4, 8, and 10) contain well developed laumontite + quartz alteration associated with small zones of brittle deformation that are likely small fault zones. At Site 8 (Tofte Park), the aa and pahoehoe flows exposed along the coastline exhibit a severely over-constrained mineral assemblage of thomsonite + scolecite + stilbite + heulandite + laumontite + quartz. This assemblage is well-developed in other large igneous provinces, for instance in eastern Iceland (Neuhoff *et al.*, 1999), where it is always associated with local hydrothermal alteration. Phase rule analysis indicates that it is over-constrained. The minerals comprising this assemblage probably did not

crystallize together, but rather sequentially in response to changes in temperature, pressure, and/or fluid composition. The flows at Site 8 are crosscut by zeolite-filled veins that were likely major fluid conduits during hydrothermal alteration of this outcrop. Only in relatively isolated vesicular zones in the center of the aa flows is the likely regional metamorphic assemblage present where the lavas were able to escape later alteration. Therefore, observations of metamorphism in the lava flows of the NSVG are based on sample sites where regional metamorphic grade was not overprinted by local hydrothermal alteration.

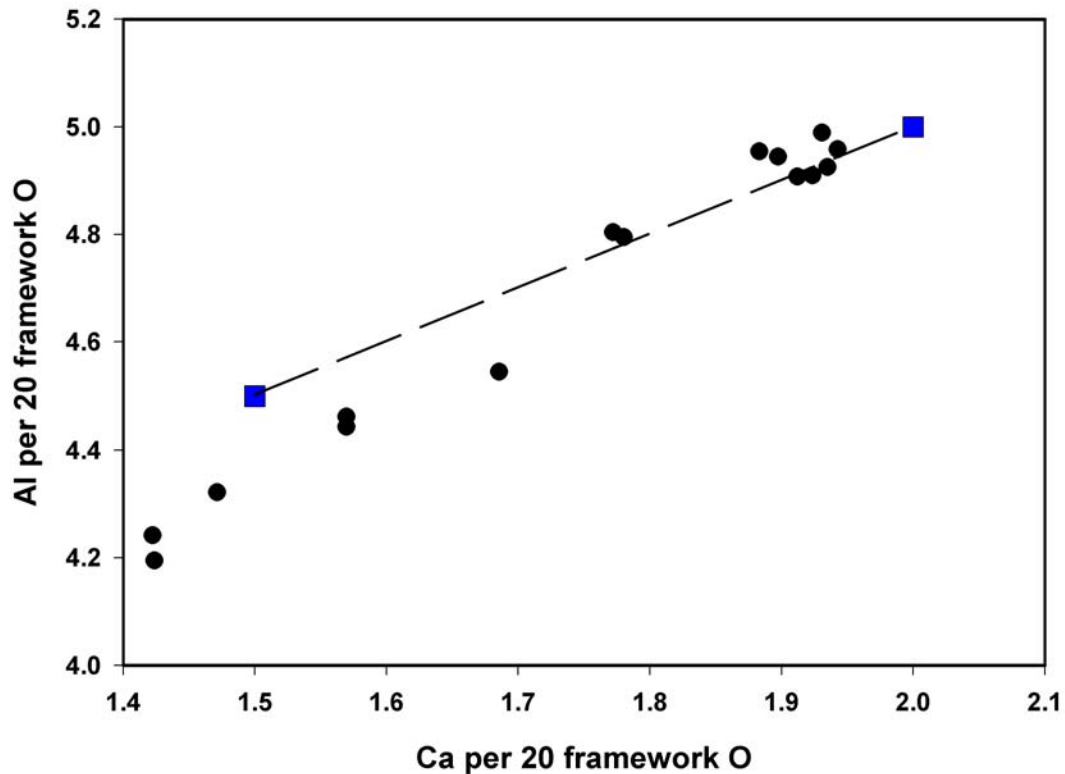


Figure 2.7: Plot showing the compositional variation of analyzed thomsonites in NSVG basalts (black circles). Thomsonite solid solution (dashed line) between  $\text{Ca}_{1.5}\text{Na}_{1.5}\text{Al}_{4.5}\text{Si}_{5.5}\text{O}_{20}\cdot n\text{H}_2\text{O}$  and  $\text{Ca}_2\text{NaAl}_5\text{Si}_5\text{O}_{20}\cdot n\text{H}_2\text{O}$  endmember compositions (blue squares) also shown (Rose *et al.*, 1992; Neuhoff and Ruhl, 2006).

Table 2.7: Representative compositions of mesolite, analcime, and laumontite.

| Sample                         | NS04-05  | NS04-10A | NS04-15A | NS04-15C | NS04-21  | NS04-14B   | NS04-03    |
|--------------------------------|----------|----------|----------|----------|----------|------------|------------|
| Mineral                        | Mesolite | Mesolite | Mesolite | Analcime | Analcime | Laumontite | Laumontite |
| <i>Oxide weight %</i>          |          |          |          |          |          |            |            |
| SiO <sub>2</sub>               | 43.79    | 44.43    | 46.42    | 53.58    | 55.56    | 51.53      | 50.64      |
| TiO <sub>2</sub>               | 0.03     | 0.01     | 0.03     | 0.05     | 0.07     | 0.01       | 0.01       |
| Al <sub>2</sub> O <sub>3</sub> | 25.48    | 25.56    | 27.09    | 22.94    | 22.36    | 22.22      | 22.03      |
| FeO <sup>a</sup>               | 0.00     | 0.01     | 0.10     | 0.00     | 0.00     | 0.09       | 0.04       |
| MnO                            | 0.00     | 0.00     | 0.00     | 0.00     | 0.02     | 0.03       | 0.00       |
| Cr <sub>2</sub> O <sub>3</sub> | 0.00     | 0.04     | 0.04     | 0.04     | 0.08     | 0.03       | 0.03       |
| MgO                            | 0.00     | 0.00     | 0.00     | 0.00     | 0.00     | 0.00       | 0.00       |
| CaO                            | 8.47     | 8.56     | 9.92     | 0.37     | 0.35     | 12.06      | 11.88      |
| Na <sub>2</sub> O              | 5.99     | 5.83     | 5.56     | 13.56    | 13.22    | 0.07       | 0.01       |
| K <sub>2</sub> O               | 0.08     | 0.05     | 0.03     | 0.09     | 0.01     | 0.09       | 0.28       |
| Total                          | 83.83    | 84.48    | 89.18    | 90.63    | 91.67    | 86.12      | 84.93      |
| <i>Anhydrous formula units</i> |          |          |          |          |          |            |            |
| Si                             | 2.97     | 2.98     | 2.96     | 1.99     | 2.03     | 3.98       | 3.96       |
| Ti                             | 0.00     | 0.00     | 0.00     | 0.00     | 0.00     | 0.00       | 0.00       |
| Al                             | 2.03     | 2.02     | 2.03     | 1.01     | 0.96     | 2.02       | 2.03       |
| Fe                             | 0.00     | 0.00     | 0.00     | 0.00     | 0.00     | 0.01       | 0.00       |
| Mn                             | 0.00     | 0.00     | 0.00     | 0.00     | 0.00     | 0.00       | 0.00       |
| Cr                             | 0.00     | 0.00     | 0.00     | 0.00     | 0.00     | 0.00       | 0.00       |
| Mg                             | 0.00     | 0.00     | 0.00     | 0.00     | 0.00     | 0.00       | 0.00       |
| Ca                             | 0.61     | 0.62     | 0.68     | 0.01     | 0.01     | 1.00       | 1.00       |
| Na                             | 0.79     | 0.76     | 0.69     | 0.98     | 0.94     | 0.01       | 0.00       |
| K                              | 0.01     | 0.00     | 0.00     | 0.00     | 0.00     | 0.01       | 0.03       |
| O <sup>b</sup>                 | 10       | 10       | 10       | 6        | 6        | 12         | 12         |
| Si/Al                          | 1.46     | 1.47     | 1.45     | 1.98     | 2.11     | 1.97       | 1.95       |
| Ca/(Ca+Na+K)                   | 0.44     | 0.45     | 0.50     | 0.01     | 0.01     | 0.98       | 0.97       |
| Na/(Ca+Na+K)                   | 0.56     | 0.55     | 0.50     | 0.98     | 0.98     | 0.01       | 0.00       |

<sup>a</sup>Total Fe reported as FeO. <sup>b</sup>Number of framework oxygens in formula unit.

Figures 2.8 and 2.9 synthesize the observations of regional metamorphic grade from this study and those of Schmidt (1993) in terms of their spatial and stratigraphic distributions, respectively. Many of the localities studied by Schmidt (1993) were

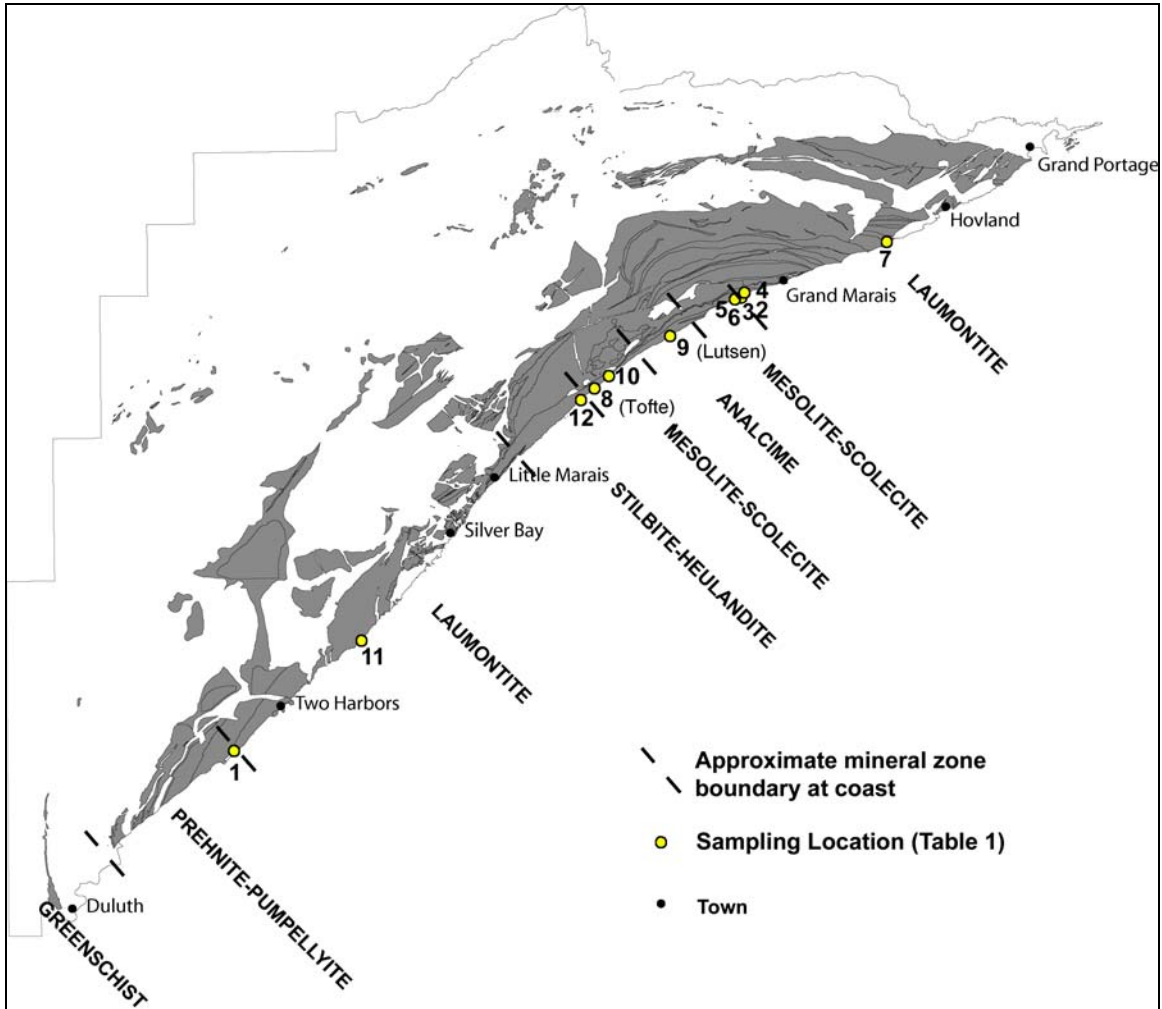


Figure 2.8: Generalized map of northeastern Minnesota showing the distribution of NSVG lavas (gray), the locations listed in Table 2.1, and interpretations of metamorphic grade based on this study and the work of Schmidt (1993) and Schmidt and Robinson (1997). Metamorphic mineral zones correspond to standard metamorphic facies designations (prehnite-pumpellyite and greenschist). Inferred boundaries between mineral zones are shown by the dashed lines.

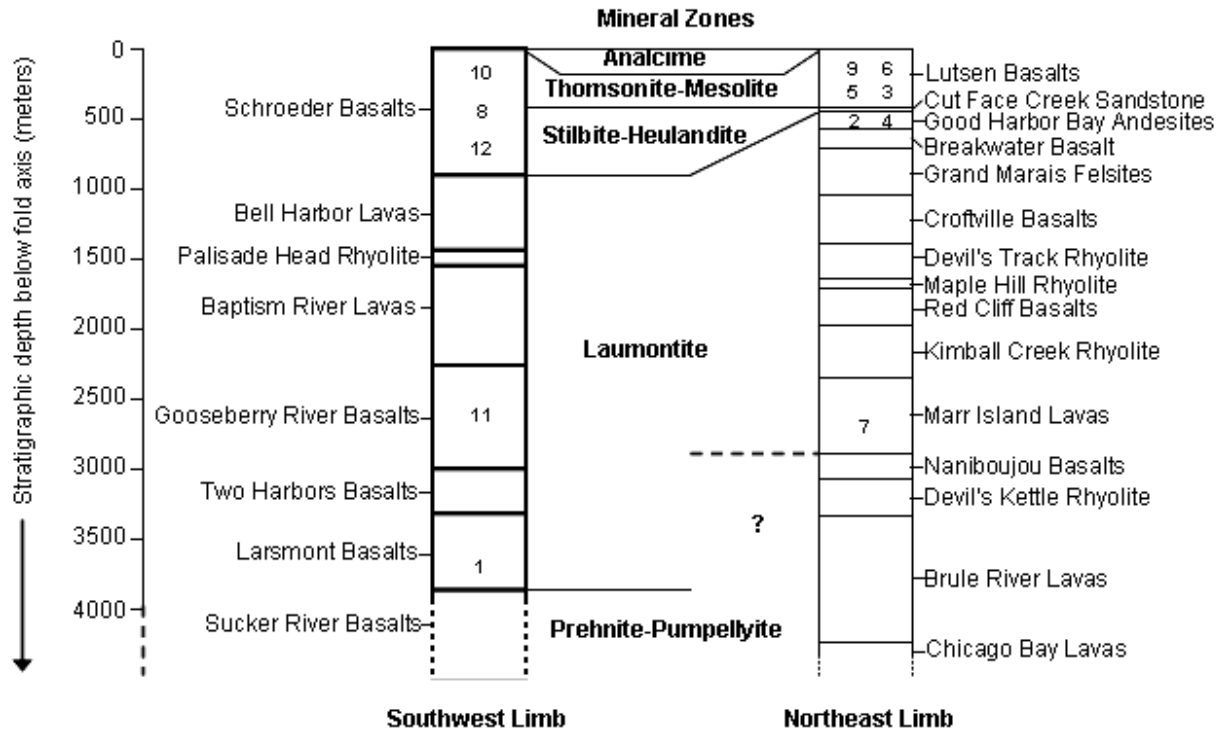


Figure 2.9: Stratigraphy of the NSVG (Vervoort and Green, 1997; Miller *et al.*, 2002) correlated along the fold axis dividing the lavas into the southwest and northeast limb. Numbers in stratigraphic columns refer to sampling sites in this study (Figure 2.1, Table 2.1). Mineral zones based on interpretations from this study and Schmidt (1993) and Schmidt and Robinson (1997).

revisited in this study, and in some cases reinterpreted in light of the complex metamorphic history noted above. Along the southern limb, the transition from the laumontite zone to the higher grade prehnite-pumpellyite zone is placed at Site 1 where primary pore spaces in adjoining lava flows indicate a change in mineral assemblage. The laumontite zone continues up through the stratigraphy for about 2700 meters until observations of stilbite and heulandite at Site 12 suggest a transition to the lower-grade the stilbite-heulandite zone. The onset of this alteration coincides with the basal contact of the Schroeder basalts along the southern limb, which shows a stratigraphic thickness of ~900 meters assuming the hinge axis as the upper extent of the section. The lower half of the Schroeder basalts contains the stilbite-heulandite zone, while the upper half of this

section shows thomsonite-mesolite zone alteration. This transition implies a correlation between shallower stratigraphic depth and lower grades of alteration.

The lowest grade of alteration noted during this study occurs at Site 9 (Lutsen Grandview Park) and corresponds to the lowermost analcime zone. This outcrop consists of a series of vesicular pahoehoe flows containing abundant thomsonite alteration. The exact extent of the analcime mineral zone is unclear due to limited exposures, though what is exposed shows no significant stratigraphic thickness. Typically in large igneous provinces there is a well-developed chabazite-thomsonite zone overlying the analcime zone (e.g., Walker, 1960; Kristmannsdóttir and Tómasson, 1978; Larsen *et al.*, 1989; Neuhoﬀ *et al.*, 1997, 2000, 2006) that is frequently as thick as the analcime, mesolite-scolecite (likely of equivalent grade to the thomsonite-scolecite zone observed in the NSVG), and stilbite-heulandite zones combined. The absence of this zone, together with the limited extent of the analcime zone and the thicknesses of the thomsonite-mesolite and stilbite-heulandite zones (Figure 2.9), implies that approximately 1000-2000 meters of the volcanic stratigraphy may have been lost to erosion in the NSVG.

The variation in metamorphic grade in the northeast limb of the NSVG appears to mirror that in the southwest limb, where metamorphic grade increases with stratigraphic depth. The Lutsen basalts exposed along the northeast limb of the NSVG are thinner (~450 meters) and contain well-developed thomsonite-mesolite zone alteration down to the lower stratigraphic boundary with the Cut Face Creek sediments. This sediment pile is ~20 meters thick, and the andesites directly below them show laumontite zone alteration. Limited accessibility precluded assessment of metamorphic grade northeast of locality 7, and thus the total thickness of the laumontite zone in this limb is

unconstrained. The most striking difference between the two limbs is the absence of stilbite-heulandite zone alteration in the northeast limb, discussed below.

### **Conditions of Alteration**

Observed mineral assemblages of the NSVG are comparable to similar alteration of the lavas in East Greenland, eastern Iceland, and the Icelandic geothermal systems (Walker, 1960; Kristmannsdóttir and Tómasson, 1978; Larsen *et al.*, 1989; Neuhoff *et al.*, 1997, 2000). The distribution of zeolite minerals with depth/temperature in basaltic terrains of Iceland and East Greenland are summarized in Figure 2.10 (Neuhoff *et al.*, 1997; 1999; 2000). The minerals observed to develop within each zeolite zone are shown with respect to temperature constraints of the mineral distributions typically observed in tholeiitic lava flows. Each mineral zone forms during alteration, transitioning to the next with increased temperature/depth.

It has been observed that thick sequences of lavas with varying chemistries exposed to the same alteration conditions will often exhibit substantially different mineral parageneses (e.g., Walker, 1960a; Robert, 2001; Neuhoff *et al.*, 2006), causing a need for observation of rock type along with alteration minerals present. The Schroeder-Lutsen basalts of the NSVG are lower in silica than those of the Greenland and Iceland provinces showing similar mineralogy, which may stabilize thomsonite relative to more silica-rich minerals like mesolite and scolecite (Neuhoff *et al.*, 2006). Therefore, the zone in Figure 2.10 labeled as the mesolite-scolecite zone is interpreted to be equivalent in grade to the thomsonite-mesolite zone.

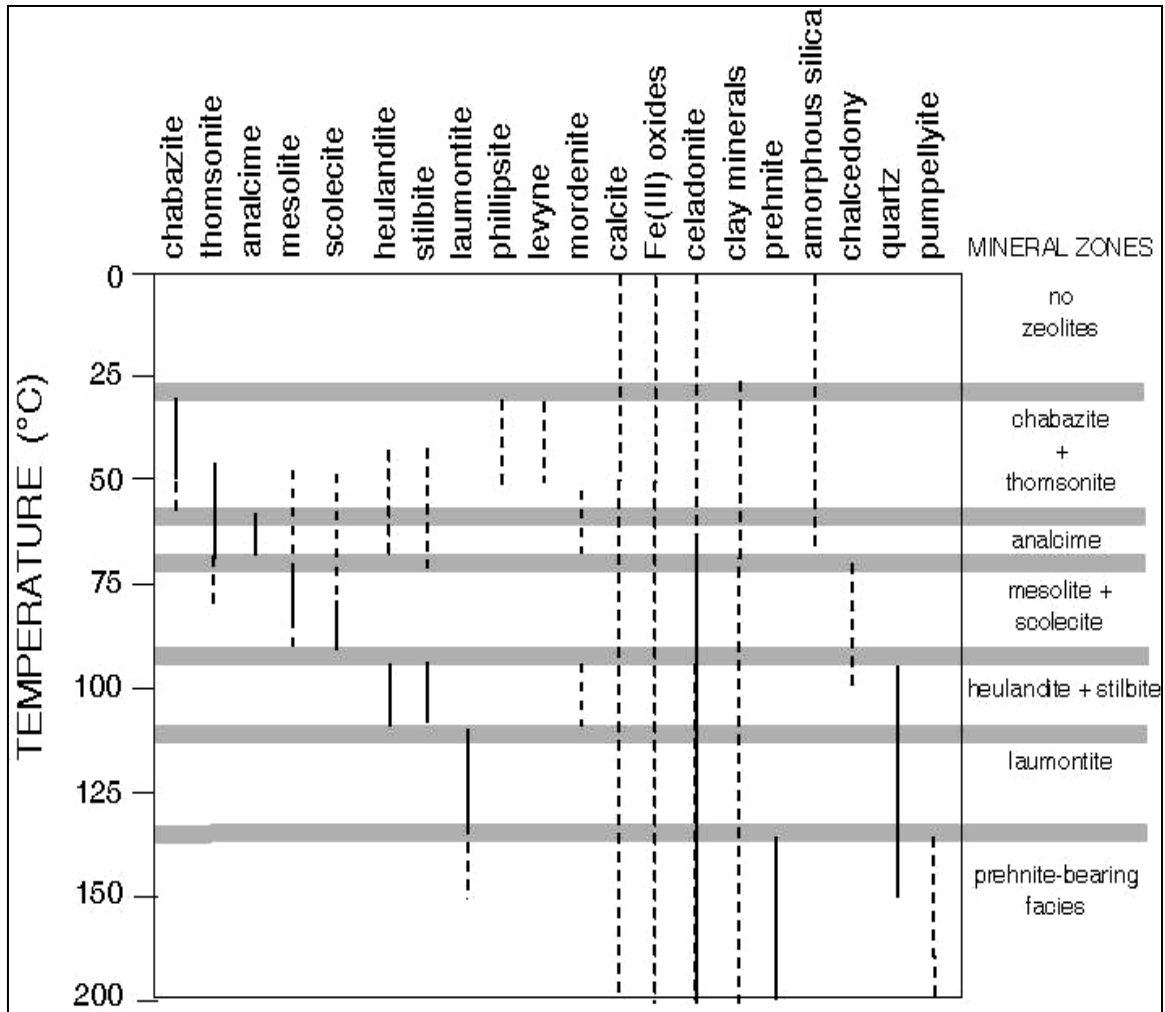


Figure 2.10: Schematic diagram showing the distribution of minerals and mineral zones typically developed during very low grade metamorphism of large igneous provinces (after Walker, 1960; Neuhoff *et al.*, 1997, 2000). Frequency of mineral occurrence with depth is denoted by solid (ubiquitous) and dashed (occasionally present) lines. Mineral list is non-exclusive. Temperatures listed on left side of diagram are based on observations by Kristmannsdóttir and Tómasson (1978) of the distribution of minerals as a function of temperature in Icelandic geothermal systems.

Figure 2.9 shows the estimated stratigraphic thicknesses given by Miller *et al.* (2002) combined with my observations of regional metamorphic grade boundaries with stratigraphic depth for the NSVG lavas. Comparisons of these observations to the observations in Figure 2.10 can be used to interpret the thermal and structural history experienced after emplacement (Neuhoff *et al.*, 2000). Observations show zeolite to

greenschist facies alteration along the exposed stratigraphy of the NSVG (Schmidt and Robinson, 1997; Neuhoff *et al.*, 2000), where alteration grade increases with stratigraphic depth along the exposure. Due to the synclinal structure of the region, the youngest lavas exposing the lowest grade of alteration are found near the hinge axis. This fold axis divides the region into two limbs, and stratigraphic depth as well as alteration grade increases to the southwest and northeast.

Analcime zone alteration, the lowest grade of alteration observed within the NSVG basalts, occurs near the hinge axis separating the Schroeder basalts in the southwest limb from the Lutsen basalts in the northeast limb. There is no significant thickness to this zone, though observations of analcime alteration in similar provinces predict relatively consistent stratigraphic thicknesses of each alteration zones. The limited thickness of the analcime zone, as well as the absence of alteration minerals exhibiting temperatures and pressures lower than analcime in grade, is likely due to erosion of once exposed stratigraphically younger lavas.

Stratigraphically below the analcime zone is the thomsonite-mesolite zone of alteration, exhibiting a consistent thickness in each limb of approximately 500 m. The lower thomsonite-mesolite boundary in the northeast limb is in direct contact with the higher grade laumontite zone, while in the southwest limb there is a 400 m thick stilbite-heulandite zone of alteration separating the thomsonite-mesolite zone from the laumontite zone. The thickness of the laumontite zone in the northeast limb is at least 1500 m, though the exact extent is unknown due to inadequate exposures further to the northeast. Assuming no structural complications, it can be expected to be as thick as the laumontite zone in the southwest limb, which is 2700 m thick and bounded below by the prehnite-

pumpellyite zone. The prehnite-pumpellyite zone is the highest grade of alteration observed in the NSVG basalts, with the onset of alteration occurring at a stratigraphic depth of 3,860 m below the fold axis. The thickness of this zone is unknown due to a lack of observations in outcrops further to the south.

The boundary constraints defined by the mapped zeolite zones can be correlated to the thermal boundaries corresponding to mineral isograds in Icelandic geothermal systems (Figure 2.10) to estimate average geothermal gradients during alteration. The well-constrained isograd locations bounding the thomsonite-mesolite and stilbite-heulandite zones in the southwest limb give a combined thickness of 900 meters, and indicate a temperature range of  $\sim 40$  °C. This implies a geothermal gradient of the NSVG region during alteration of approximately 42 °C/km, which compares well to the estimated geothermal gradients of 55 °C/km observed in LIPS formed during continental rifting in eastern Iceland (Neuhoff *et al.*, 1999) and 40 °C/km in East Greenland (Neuhoff *et al.*, 2000).

This information also can be used to calculate overburden pressure and heat flow experienced during the time of alteration. The estimated stratigraphic thickness of the basalts experiencing zeolitization during the time of alteration is  $\sim 5500$  m after combining the known stratigraphy with the estimated loss due to erosion. Pressures thus increased from a minimum of 1 bar (assuming atmospheric pressure) to maximum pressures ranging from  $\sim 550$  to  $\sim 1600$  bars, corresponding to hydrostatic and lithostatic pressures, respectively. Regional heat flow over the area during alteration was about 1.3-2.2 heat flow units, given a thermal conductivity for water-saturated basalt of 1.5-2.0 W/mK (Oxburgh and Argell, 1982) and the implied geothermal gradient for the NSVG of

42° C/km. These values are comparable to heat flow in present-day continental rift systems (Lysak, 1992).

### **Structural Interpretations**

The overall structure of the NSVG is a plunging synclinal fold with a hinge axis in the area between Tofte and Lutsen (e.g. Miller *et al.*, 2002). This fold has been interpreted as a subsidence feature formed during eruption of the lava pile due to evacuation of the underlying magma chamber and increased density of the growing lava pile (e.g., Ojakangas and Matsch, 1982), or alternatively as a late structural modification of the area due to strong influences from the nearby Grenville orogen (Van Schmus and Hinze, 1985).

The observation that metamorphic grade increases with stratigraphic depth, in both limbs of the province, has considerable implications for the structural development of the NSVG. Based on my field observations combined with those of Schmidt (1990), the distribution of secondary mineral paragenesis represented in the NSVG suggests that the metamorphic zones are folded along with the lavas. Regional metamorphism in large igneous provinces typically is initiated soon after volcanism and is of short duration (e.g., < 1 Ma; Neuhoff *et al.*, 1997). Thus, if the folding of the NSVG was syn-volcanic, one would expect the mineral zones to cross-cut the stratigraphy, whereas the isograds would be folded along with the lavas if deformation were due to post-volcanic processes. Combining this information with the observation that the regional metamorphism is typically rapid and of short duration after complete eruption of the lava pile in large igneous provinces (e.g. Neuhoff *et al.*, 1997, 1999, 2000), it appears that folding of the NSVG is a post-volcanic feature and was not a mechanism of crustal accommodation of the immense lava pile developed in this province.

The stratigraphic distributions of zeolite zones in the NSVG (Figure 2.9) are not symmetrical between limbs, as indicated by the absence of the stilbite-heulandite zone in the northwest limb of the province. Previous observations of zeolite zones in other continental flood basalt provinces have shown that these zones are relatively continuous and uniform in thickness (Walker, 1960b; Neuhoff *et al.*, 2000). Correlation of the overlying thomsonite-mesolite zone between the northeast and southwest limb show continuous and uniform thickness, implying that this should be the case in the continental flood basalts of the NSVG. The stilbite-heulandite zone, however, is mapped in the southwest limb with a thickness of almost 450m but is not present in the northeast limb. The expected position of the stilbite-heulandite zone in the northeast limb corresponds to the location of the Cutface Creek sediments, which are only 30-40 m thick and thus not extensive enough to contain the whole range of stratigraphic depth expected for this zone.

Two possible explanations might account for the lack of the stilbite-heulandite zone in the northeast limb. The first is based on the fact that there is a marked change in lava composition between the thomsonite-mesolite zone occurrences at site 3 (and immediately overlying the Cutface Creek sediments) and the laumontite zone lavas at site 4, with the latter exhibiting more silicic basaltic andesite compositions (e.g., Walker, 1960a; Kristmannsdóttir and Tómasson, 1978; Murata *et al.*, 1987; Hearn *et al.*, 1989; Robert, 2001; Neuhoff *et al.*, 2006). Potentially this change in lava composition may result in laumontite occurring at lower grades. This should, however, stabilize the more Si-rich minerals stilbite and heulandite relative to laumontite, not the other way around. A more plausible hypothesis is that there is a loss of stratigraphy in the region between sites 3 and 4. High-angle reverse faults are observed in the central and western regions of

this area due to compression, causing juxtaposition of older rocks next to younger rocks (e.g., White, 1966; Van Schmus and Hinze, 1985). Reverse faulting may have also occurred in the eastern region of the NSVG, and could explain the absence of the stilbite-heulandite zeolite zone in the northeast limb. The potential displacement of this alteration zone therefore occurred as relatively late faulting of the NSVG basalts, which agrees with the suggested post-volcanic compression.

CHAPTER 3  
PETROGRAPHIC AND DIGITAL ANALYSIS OF POROSITY EVOLUTION  
DURING ALTERATION

**Introduction**

Permeability in basaltic lavas has received considerable attention recently due to increased focus on their hydrologic properties and the role of degassing of volatiles in the dynamics of eruptive events (e.g., Fisher, 1998; Saar and Manga, 1999; Blower, 2001a, b; Srouga, 2004; Stimac, 2004). From this work, it is becoming increasingly clear that the geometry and connectivity of the pore network in vesicular lavas is fundamentally different than in more commonly considered porous media such as sediments and fractured rocks, and more attention is being placed on the relationship between porosity and permeability. For lavas with porosities >60%, there appears to be no significant relationship between porosity and permeability; when porosities are below 60%, however, experimental results from different studies show varying porosity-permeability relationships (Eichelberger *et al.*, 1986; Klug and Cashman, 1996; Saar and Manga, 1999).

In vesicular basalts the permeability can be as high as  $10^{-7}$  cm<sup>2</sup>, which is a value comparable to clean unconsolidated sand or karstic limestone. In basalts where the vesicles are small and closely spaced, there will be an increased probability of connected fluid pathways developing between pores that will likely lead to these higher permeabilities (e.g., Saar and Manga, 1999). Percolation theory (Lee, 1990; Sahimi, 1994; Grimmett, 1999) applied to basalts in experimental studies shows that the

percolation threshold, the critical porosity below which percolating clusters of bubbles should not exist, is around 30%, implying that little to no permeability can be expected below critical porosity. In these low porosity basalts, the vesicles become more isolated. If connectivity between pores is dependant on fluid flow through the matrix, permeability can be as low as  $10^{-18}$  cm<sup>2</sup> (Johnson, 1980; Saar and Manga, 1999). Multiple studies have shown, however, that vesicular lavas retain relatively high permeabilities ( $>10^{-8}$  cm<sup>2</sup>) down to porosities as low as a few percent (Feng *et al.*, 1987; Sahimi, 1994, 1995; Saar and Manga, 1999; Blower, 2001b). This does not follow the predicted model for granular rocks, and implies that there must be pathways forming within the matrix allowing fluid to flow at a faster rate.

Differences in porosity within basaltic lava flows leads to considerable flow-scale variations responsible for the development of secondary mineral paragenesis (Schmidt, 1990; Schmidt and Robinson, 1997). Under low-grade alteration, the chemical components necessary to precipitate the vesicle-filling minerals are derived from a spatially restricted region (alteration halos) around the vesicle and the fluid pathways over which diffusion occurs. This suggests that the presence of mineral infillings can be a reliable indicator of pores being part of a permeable network through the lava, as fluid flow is inherently coupled to changes in porosity and permeability brought about by mineralogic alteration. This chapter explores using mineralogic alteration to trace fluid pathways through the lavas and the temporal evolution of pore space through time. These observations will prove important not only for further understanding of groundwater and petroleum reservoirs in basalts, but also developing new methods to monitor the controls and affects of fluid flow and alteration within vesicular rocks.

## Methods

### Field Techniques

Field work was conducted along the north shore of Lake Superior in Minnesota during July 15-26, 2004. Of the sampling sites and methods discussed in Chapter 2, measurements were performed at sites 3, 4 and 6 (Table 2.1, Figure 2.1) of total initial porosity, pore size distributions, and the amount and type of secondary alteration within primary pore space and within the matrix.

Measurements of total porosity were made both on the thin section scale through digital analysis as well as on the outcrop scale in the field. All porosity in analyzed samples is essentially zero, due to the complete infilling of all vesicles by secondary alteration, so primary porosity is analyzed based on the initial void space in vesicles prior to alteration. *In situ* field measurements of primary macroscopic porosity (defined in this paper as the percentage of a given volume of rock occupied by pore space) were made in the field following the methods of Manning and Bird (1991). This is done by placing a transparent mylar sheet embossed with a precision drafted grid (1073 nodes) directly on the outcrop and counting the number of nodes on the grid that overlay pores. Porosity was taken to be the percentage of nodes overlying pores (Manning and Bird, 1991).

Measurements were made to assess the pore size distributions within sampled lava flows. Overall pore size distributions were assessed by measuring the maximum and minimum diameter of all pores within a representative area. Notes were made on the progress of reaction of each measured pore by assessing the level of secondary alteration observed with respect to pore size. Observations also were made of the amount of alteration visible in the matrix around and between pores to assess the characteristics of

fluid flow through the rock as well as the amount of lava that has undergone alteration during low-grade metamorphism.

### **Optical and Digital Techniques**

Numerous techniques have been applied to determine the distribution and character of macroscopic pore space in lavas, including impregnation with plastics and dissolution of the lava to reveal casts of pore structure (e.g., Sahagian *et al.*, 1989), three-dimensional imaging by X-ray computed tomography (e.g., Song *et al.*, 2001; Sahagian *et al.*, 2002), and digital analysis of two dimensional sections (e.g., Toramaru, 1990; Klug and Cashman, 1996; Sahagian and Prousevitch, 1998; Al-Harthi *et al.*, 1999; Saar and Manga, 1999). In this study, I adopt the last approach, because digital analysis of two dimensional sections will permit direct correlation of pore structure to the chemical and mineralogical observations.

Three thin sections from different regions are examined; a chabazite zone metabasalt from East Greenland, a mesolite-scolecite zone metabasalt from eastern Iceland, and a laumontite zone metabasalt from the NSVG (Site 4). These samples are chosen to represent progressive stages of zeolite alteration with respect to the range of pore evolution experienced during alteration. Thin sections are prepared for each sample, and digital images are prepared from the original thin section. This is done either by capturing digital images through a high powered petrographic microscope, or by scanning the thin section using a backlit flatbed scanner to create a high resolution image. These images were imported into the image processing software Adobe® Photoshop®, which was used to exaggerate the contrast between the features of interest and the background groundmass, remove residual background noise created during scanning, and convert the image to grayscale. The images were then imported into either Image J or ArcView®

GIS 3.2a (ArcView); both programs were used to measure and statistically analyze the porosity and secondary mineral phases in the images. When imported into ArcView the images were converted into shape files by creating a vector data format, which represents features as polygons defined by coordinate pairs, allowing for data analysis to be performed on the image. For porosity measurements, these methods were limited to pores visible at the thin section scale. This excludes macro-pores larger than the size of a standard thin section ( $27 \times 46$  mm) or micro-pores smaller than the pixilation ability of the digital image processing software (which varies between programs).

### **Observations**

#### **NSVG Field Sites 3, 4 and 6**

In situ field measurements of total original macroscopic porosity were made at Sites 4 and 6 (Table 2.1) within the NSVG, where outcrop exposures were adequate for sampling methods. Porosity measurements in the field were limited to macroscopic observations, which confined analysis to the high porosity tops and bottoms of each lava flow. Two measurements at Site 4 show primary porosities of 19.7% and 21.7%, and one measurement at Site 6 shows a primary porosity of 15%. This highlights the localized variation of porosity experienced within these high porosity zones of each lava flow.

Figure 3.1 shows a close-up of an outcrop exposure at Site 6 that is also representative of porosity at Site 4. It can be observed from this figure that vesicle shape, size and spacing vary considerably, and the numbered regions highlight examples of this random distribution. Circle 1 highlights an area of little to no porosity surrounded by vesicular areas. The average vesicle was oval to round in shape, though many vesicles exhibited little to no sphericity appearing more elongated as highlighted by the vesicle (4x12 mm) in circle 2. Vesicle size distributions within these measured zones were

highly variable, with average vesicle radii ranging from 46 to 1 mm. Table 3.1 gives the statistical analysis of vesicle size measurements performed on the outcrop of all amygdules, as well as those showing only thomsonite alteration or thomsonite and

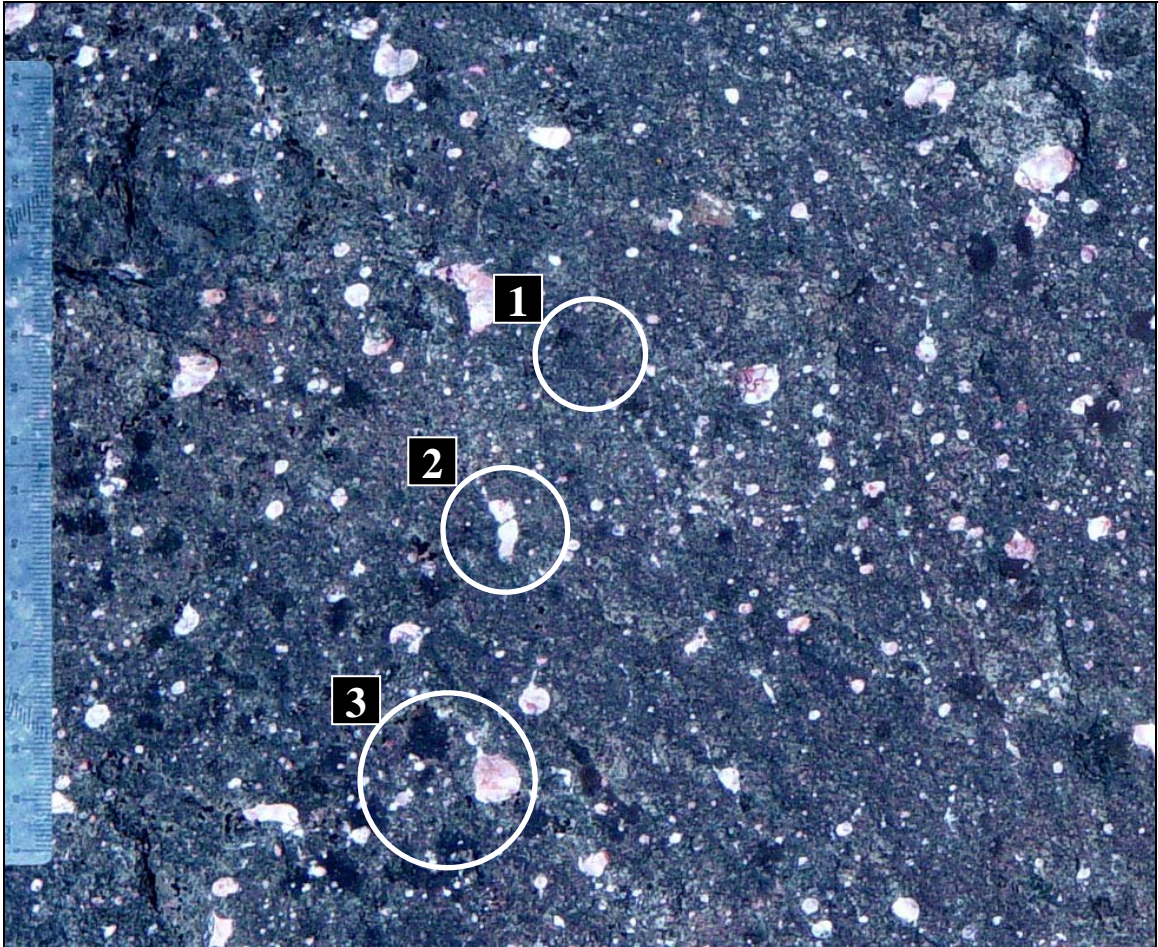


Figure 3.1: Outcrop photograph of vesicular basalt at Site 6 (Table 2.1) illustrating typical variation in pore size, shape and spacing. Ruler (15 cm long) shown on the left for scale. Vesicles are filled with white thomsonite-mesolite aggregates surrounded by the gray basalt. Numbered circles highlight various porosity characteristics of basalt; highlighted areas show 1) little to no porosity, 2) elongated vesicle, and 3) pores of various sizes in close proximity to each other.

mesolite alteration (discussed further below). Circle 3 in Figure 3.1 contains vesicles within close proximity of each other that range in size from ~1 to 10 mm. In each of these highlighted regions and in the areas surrounding them, there are no vesicles that are

visibly connected. The lack of interconnection between vesicles was observed at each sampling site.

Table 3.1: Statistical analysis of vesicle size (diameter) as a function of reaction progress from outcrop scale measurements at Site 6.

|                                      | All vesicles | Thomsonite only | Thomsonite + Mesolite |
|--------------------------------------|--------------|-----------------|-----------------------|
| <i>Statistical Data<sup>a</sup></i>  |              |                 |                       |
| n                                    | 185          | 125             | 160                   |
| Size Range                           | 1 – 46       | 1 – 10          | 10 – 46               |
| Mean                                 | 9.48         | 2.62            | 23.76                 |
| Mode                                 | 1.00         | 1.00            | 22.00                 |
| St. Dev. <sup>b</sup>                | 11.10        | 2.25            | 8.17                  |
| <i>Size Distribution<sup>c</sup></i> |              |                 |                       |
| 25%                                  | 17.00        | 1.00            | 1.00                  |
| 50%                                  | 22.50        | 2.00            | 4.00                  |
| 75%                                  | 28.50        | 3.00            | 17.0                  |
| 100%                                 | 46.00        | 10.00           | 46.00                 |

<sup>a</sup>All diameter values are given in mm. <sup>b</sup>Standard Deviation. <sup>c</sup>Percentage of pores  $\leq$  given value.

All vesicles were completely occluded due to secondary alteration, causing them to appear white or pink in outcrop. Many of the sites contained vesicles that appeared partially or completely unfilled, and the presence of such vesicles increased along river bed and shoreline exposures. Cut samples exposing fresh surfaces, however, showed complete infilling of all vesicles, thus these open vesicles can be attributed to weathering of alteration minerals. Sites 3 and 6 contained vesicles filled with either thomsonite or thomsonite and mesolite (Table 3.1). Vesicles at Site 4 were filled with either chlorite or chlorite and laumontite with occasional calcite overprinting of the laumontite.

Observations of collected NSVG samples show that matrix alteration varies within a given sample from areas with little alteration to areas showing complete alteration of primary magmatic phases. These areas of high alteration appear to exist as reaction aureoles around primary pore spaces, and around what appear to be microfractures acting as pathways between vesicles through the matrix. Figure 3.2A (also shown in Figure 2.4)

depicts the visible aureoles at the outcrop scale (Site 3), appearing as light-pink areas around and between amygdules. Figure 3.2B shows a schematic representation of these observed aureoles. The aureoles around vesicles are generally thicker than those around the possible microfractures between vesicles. In many cases the veins appear as connecting pathways between vesicles.

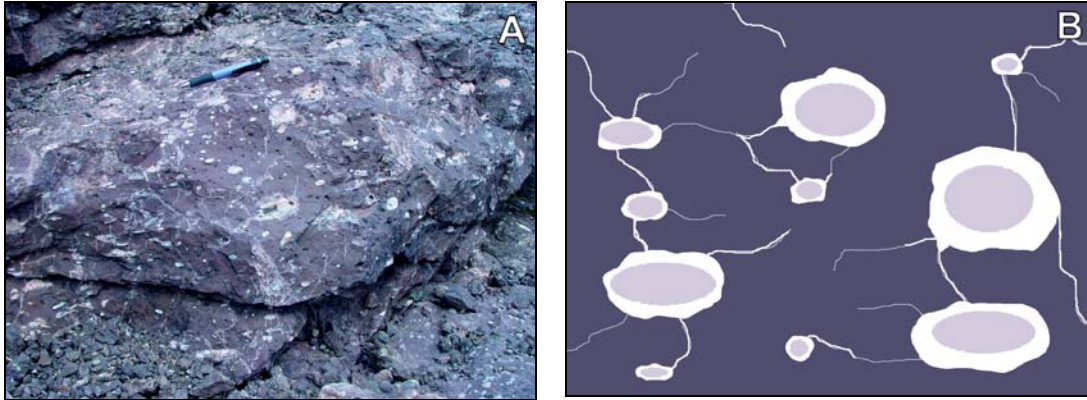


Figure 3.2: Images of reaction zones around and between macroscopic pore space in NSVG lavas. A) Field photo from Site 3 (Table 2.1) showing an extensively altered pahoehoe flow with bleached haloes around vesicles connected by thin anastomosing bleached areas. Pencil for scale. B) Schematic depiction of matrix alteration shown in (A), with broad alteration halos (white) around vesicles (light gray) connected by thin strands of alteration.

These aureoles were first observed as a weathering phenomenon at the outcrop scale, and further analysis of cut hand samples and thin sections (Figure 3.3) show that they are present throughout the entire rock. They are clearly visible as lighter areas around and between vesicles, though at higher magnifications they have a dark appearance compared to the less altered matrix surrounding them.

Petrographic observations at the thin section scale show that alteration appears to occur in stages that are independent of both lava composition and grade of alteration. Figure 3.4 depicts three stages of alteration observed within the matrix of analyzed

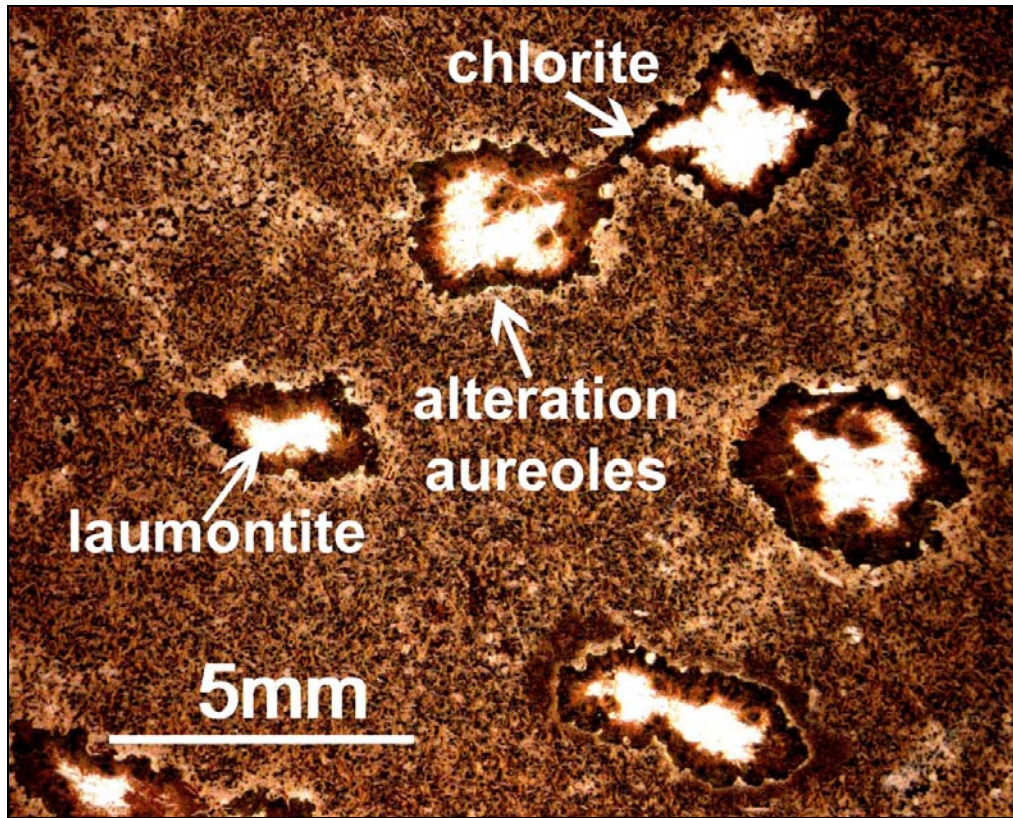


Figure 3.3: Image is of sample NS04-14, showing the laumontite zone alteration found at Site 4. Image was captured using a reflected light binocular microscope. Chlorite is the first mineral to fill the pore, as seen by the dark rim around the pore wall. Residual open space is filled by laumontite, the white mineral in the center of each pore. Alteration aureoles are seen here as light colored rims around and between pores.

NSVG samples, with minor alteration in 3.4A to extensive alteration in 3.4C. Figure 3.4A shows a sample containing the highest percentage of unaltered matrix (lighter matrix) where the areas of alteration (darker band in matrix) appear as networking veins. In samples exhibiting more alteration (Figure 3.4B), the areas of unaltered matrix are smaller and are surrounded by thicker networking veins. Other samples show no networking of alteration (Figure 3.4C), and instead the entire matrix has undergone alteration.

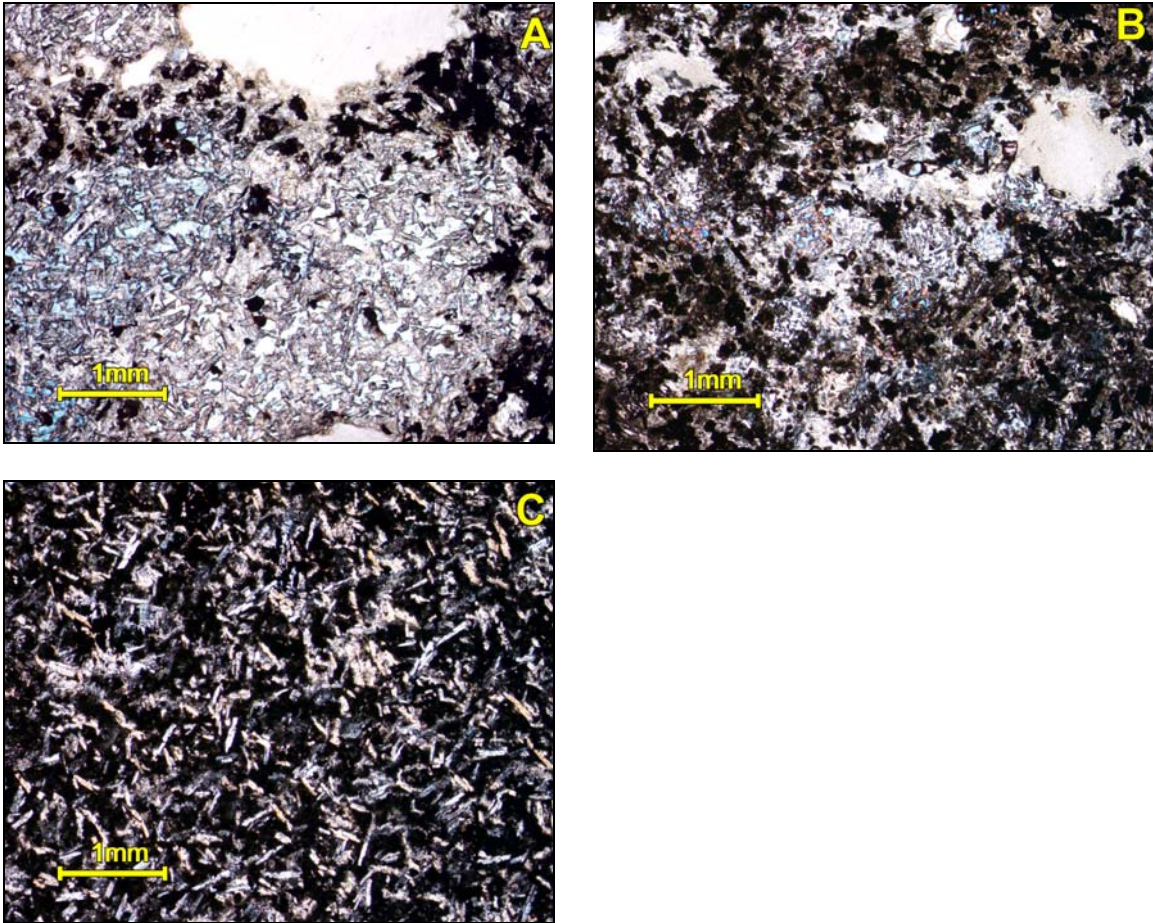


Figure 3.4: Various levels of secondary alteration in the matrix of NSVG basalts sampled during the field season. All photomicrographs were taken through crossed polars. A) Alteration (darker areas) occurs in a network pattern through the matrix (sample NS04-31), surrounding areas of unaltered matrix and connecting zeolitized amygdules. Fresh feldspars and pyroxenes can be observed in the unaltered matrix (lighter areas). B) Thicker network pattern of matrix alteration (sample NS04-15) surrounding small patches of unaltered matrix where fresh feldspars and pyroxenes can still be observed. C) Matrix has undergone complete alteration (sample NS04-14), with visible feldspar laths but no residual pyroxene.

The dominant minerals observed within these alteration aureoles are iron oxides, clay minerals, and zeolites. There is a dominant expression of iron oxides occurring within the altered matrix further away from pore spaces, while zeolite mineralization increases closer to primary pore spaces. Samples exhibiting more intense alteration show the complete disappearance of primary pyroxene and alteration of the plagioclase laths.

## **Reaction Progress**

Low-grade metabasalt samples exhibiting zeolite zone alteration were selected to show varying levels of secondary mineral formation through increasing alteration from chabazite to mesolite-scolecite to laumontite zeolite zones. Samples from Greenland, Iceland, and Sites 4 and 6 from the NSVG were analyzed for aspects of pore geometry such as spacing, size and shape and were observed with respect to the extent of reaction progress experienced during alteration. The progress of reaction is evident through the progressive infilling of vesicles. At very low grades, the vesicles experience partial infilling, and as grade increases, so does the amount of secondary mineral precipitation within the vesicle. Vesicles are progressively filled with clay minerals, clay and zeolite minerals, or multiple generations of zeolite minerals.

### **Partial infilling at low-grades**

A low-grade metabasalt from East Greenland exhibiting chabazite zone alteration (Neuhoff *et al.*, 1997) was used for analysis of very low grades of alteration, as alteration lower in grade than the analcime zeolite zone are not preserved within the NSVG lavas. A thin section (421505) representing chabazite zone alteration is shown in Figure 3.5A. This thin section contains vesicles exhibiting three levels of alteration, those that are variably empty, completely filled with chabazite, or partially filled with chabazite, and analysis is performed to assess vesicle properties in relation to these alteration characteristics. Figure 3.5B shows the thin section converted into a shape-file for area analysis in ArcView 3.2a. The region highlighted in both images by the dashed line depicts an area with very little secondary mineral infilling. The lack of mineralization is independent of vesicle size and shape, and instead may be an effect of limited fluid flow through this region during alteration.

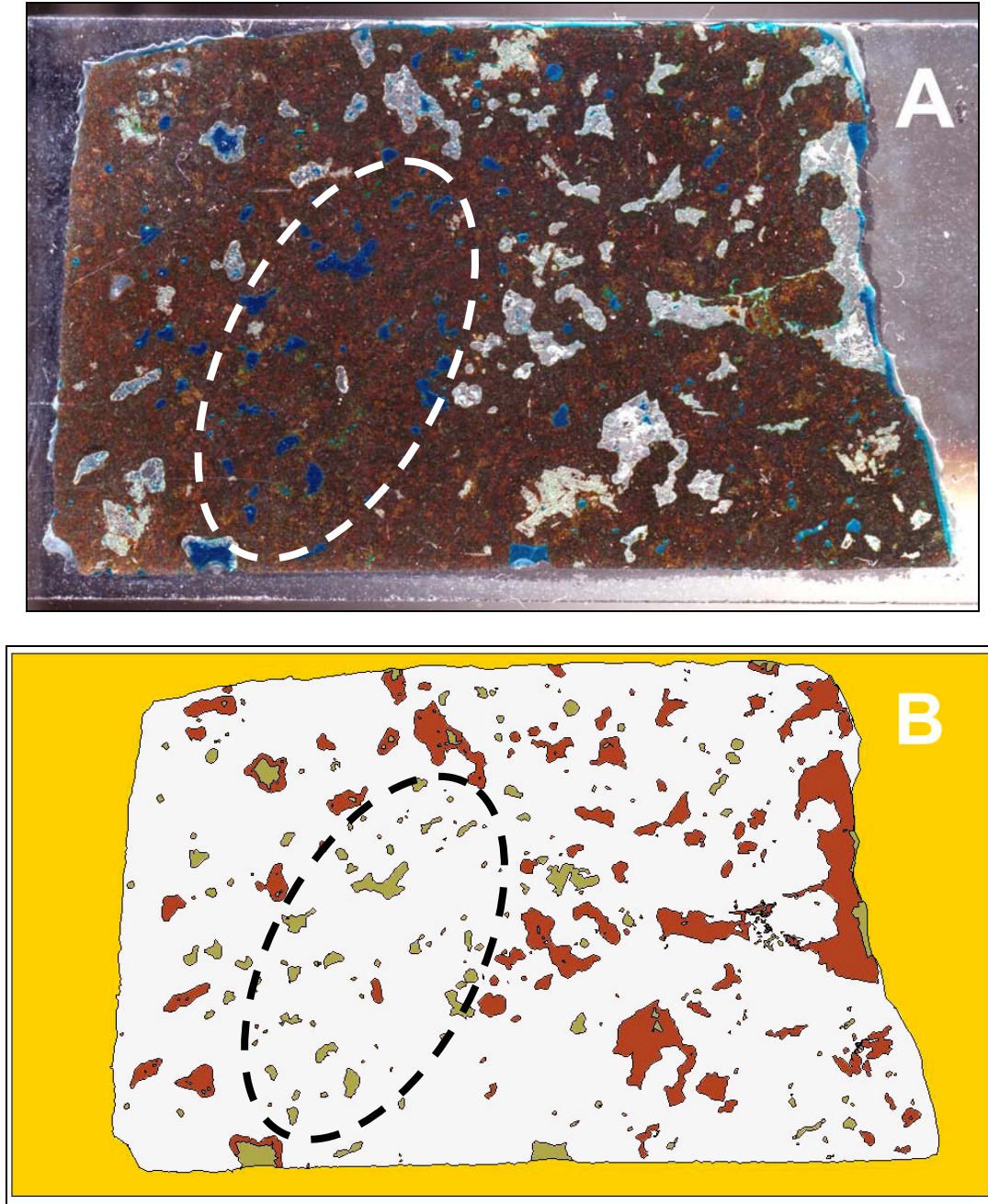


Figure 3.5: Example of digital analysis of vesicle fillings in a zeolite facies vesicular lava from East Greenland. The original thin section (A) contains vesicles (278 individual objects, comprising 13.2% of the sample) that are partly filled with chabazite. The region highlighted within the dashed line (in A and B) shows almost no secondary mineralization; see text for discussion. Part (B) shows separation of the three degrees of vesicle-scale alteration; vesicles unaffected (unfilled) by alteration (light brown), completely-filled vesicles (dark brown), and partially-filled vesicles (light and dark brown).

Area measurements were conducted on 284 vesicles, and each vesicle was then categorized with respect to the level of alteration with values shown in Table 3.2. Total original porosity of the sample (calculated from the area of vesicle space divided by the total thin section area) is 13.2%, and the zeolite infillings occupy 70.4% of the original pore space (corresponding to a 9.4% increase in solid volume during alteration). Figure 3.6 shows the frequency of vesicles as a function of area and the level of alteration observed within the pore. Visual inspection of Figure 3.6 suggests that, in this sample, chabazite infilling is most prominent in larger vesicles, and that larger chabazite-filled vesicles are more likely to retain porosity after zeolite formation. The large spread in data shows that while the level of alteration is affected by vesicle size (average area of vesicles retaining open porosity is larger than those completely filled), this may not be the only controlling factor.

Table 3.2: Statistical analysis of vesicle size (area) as a function of reaction progress from measured vesicles of a low-grade metabasalt from East Greenland (thin section 421505). Vesicles are either completely filled (filled), completely open (unfilled), or partially filled with residual pore space (partially filled).

|                                      | All vesicles  | Filled        | Unfilled      | Partially filled |
|--------------------------------------|---------------|---------------|---------------|------------------|
| <i>Statistical Data<sup>a</sup></i>  |               |               |               |                  |
| n                                    | 278           | 68            | 189           | 21               |
| Size Range                           | 0.001 – 2.502 | 0.001 – 1.395 | 0.001 – 0.543 | 0.053 – 2.502    |
| Mean                                 | 0.094         | 0.082         | 0.035         | 0.661            |
| Mode                                 | 0.002         | 0.002         | 0.002         | --               |
| St. Dev. <sup>b</sup>                | 0.239         | 0.090         | 0.072         | 0.586            |
| <i>Size Distribution<sup>c</sup></i> |               |               |               |                  |
| 25%                                  | 0.004         | 0.011         | 0.003         | 0.280            |
| 50%                                  | 0.018         | 0.051         | 0.010         | 0.401            |
| 75%                                  | 0.086         | 0.126         | 0.033         | 0.907            |
| 100%                                 | 2.502         | 0.395         | 0.543         | 2.502            |

<sup>a</sup>All area values are given in mm<sup>2</sup>. <sup>b</sup>Standard Deviation. <sup>c</sup>Percentage of pores  $\leq$  given value.

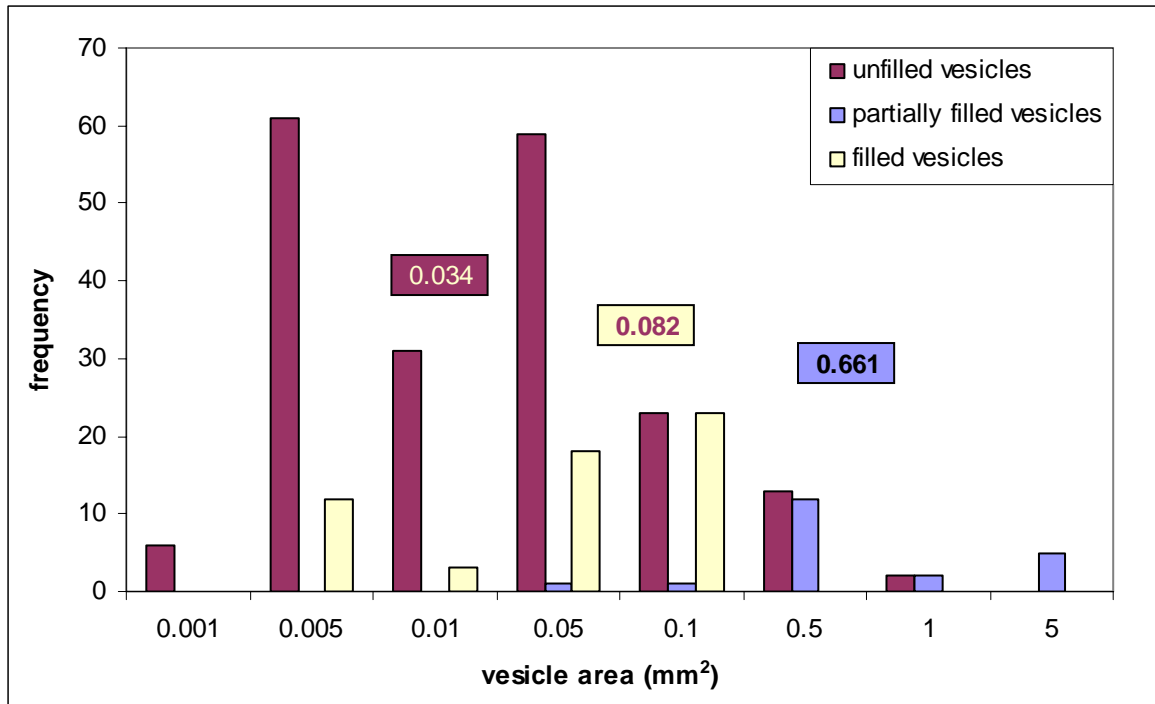


Figure 3.6: Frequency of vesicle areas versus the amount of secondary alteration filling the vesicle for a sample of chabazite-thomsonite zone alteration from East Greenland (cf. Neuhoff *et al.*, 1997). Vesicles are unfilled, partially filled or completely filled with chabazite. Average vesicle area for each level of alteration is labeled.

### Mafic phyllosilicate to zeolite infilling

Observation of lavas exhibiting zeolite alteration higher in grade than chabazite-thomsonite zone found no residual pore space in vesicles observed in thin section. The relationship between reaction progress and alteration minerals then becomes related to the progressive stages of mineral precipitation within vesicles. Low-grade metabasalts from Site 4 in the NSVG and from eastern Iceland exhibit early precipitation of mafic phyllosilicates followed by later stage zeolite infilling.

Samples collected during the field season at the Cutface Creek location (Site 4, see Table 2.1) within the NSVG exhibit laumontite zone alteration. Microprobe analysis of a sample in thin section shows each vesicle initially filled with chlorite rims (Figure 3.3),

with any residual pore space completely filled with laumontite during later stages of alteration. Visual inspection of vesicles (Figure 3.3) also shows a consistency in thickness of chlorite rims irrespective of vesicle size and shape. All vesicles within this thin section were measured for total area and for the amount (in area) filled by laumontite and chlorite, and values are represented in Table 3.3. Chlorite rim thicknesses in this sample also were measured (Table 3.3) and are statistically consistent throughout the thin section (0.52 +/- 0.12 mm). Figure 3.7 plots this consistency in thickness with respect to vesicle area, as well as the percentage of the vesicle filled with chlorite, and shows that the decrease in chlorite infilling as vesicle size increases is due to the consistency in chlorite rim thicknesses. Figure 3.8 again shows the percentage of chlorite infilling with respect to area, and also shows the percentage of laumontite infilling with respect to area. Due to the consistency in clay rim thicknesses, the percentage of each vesicle filled with chlorite decreases as the area of the pore increases, leaving more residual space in larger pores for later infilling of laumontite.

Table 3.3: Statistical analysis of vesicle size as a function of reaction progress for vesicles filled with chlorite and/or laumontite at the thin section scale (sample NS04-14) from Site 4. Area data is given in mm<sup>2</sup> for the entire vesicle and for the area of the vesicle filled by laumontite and chlorite. Chlorite rim thickness measurements are given in mm.

|                                      | Vesicle Area | Laumontite Area | Chlorite Area | Chlorite thickness |
|--------------------------------------|--------------|-----------------|---------------|--------------------|
| <i>Statistical Data</i>              |              |                 |               |                    |
| n                                    | 23           | 23              | 23            | 255                |
| Size Range                           | 1.39 – 23.30 | 0.00 – 16.84    | 1.29 – 14.21  | 0.29 – 0.90        |
| Mean                                 | 10.33        | 5.01            | 5.32          | 0.52               |
| Mode                                 | --           | 0.00            | --            | 0.55               |
| St. Dev. <sup>a</sup>                | 6.43         | 4.76            | 3.16          | 0.12               |
| <i>Size Distribution<sup>c</sup></i> |              |                 |               |                    |
| 25%                                  | 3.76         | 1.36            | 2.41          | 0.41               |
| 50%                                  | 5.17         | 1.71            | 3.46          | 0.67               |
| 75%                                  | 14.12        | 7.28            | 6.84          | 0.50               |
| 100%                                 | 16.43        | 15.14           | 1.29          | 0.51               |

<sup>a</sup>Standard Deviation. <sup>b</sup>Percentage of pores  $\leq$  given value.

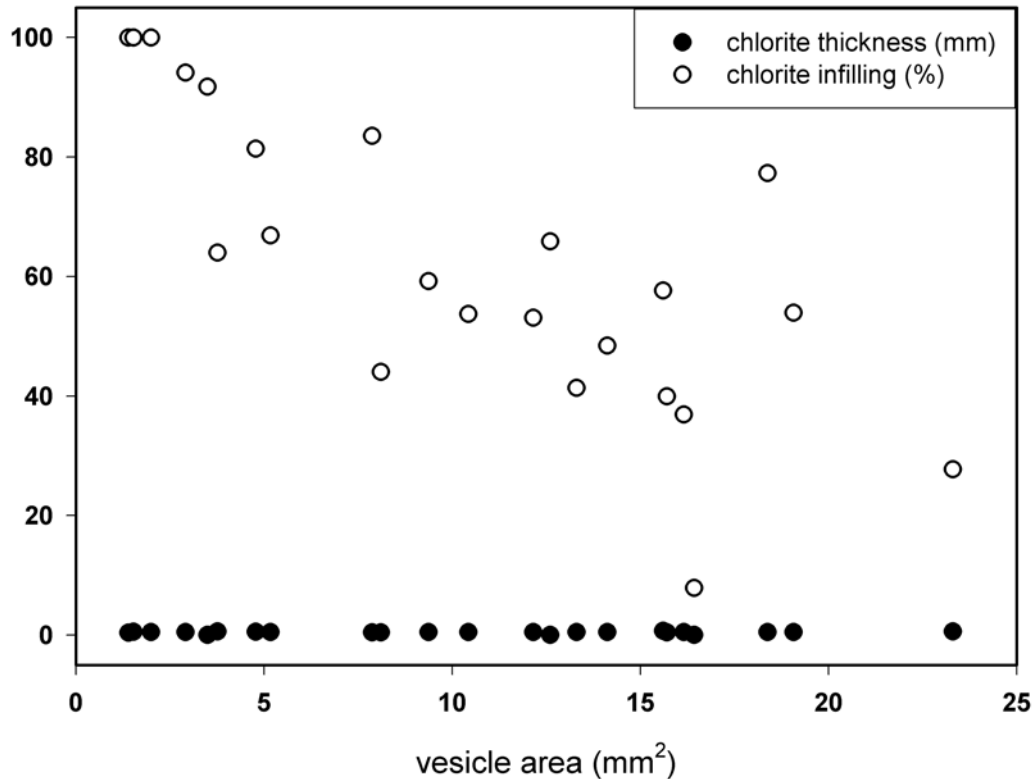


Figure 3.7: Plot shows the thickness in mm of chlorite rims (black circles) and the total percent of the vesicle filled with chlorite (open circles) with respect to total vesicle area in mm<sup>2</sup>. As vesicle area increases, the chlorite rims maintain a consistent thickness of ~0.52 mm, while the percentage of vesicle occlusion by chlorite steadily decreases.

Further analysis of this consistency in thickness of mafic phyllosilicate rims was performed on a previously collected sample from eastern Iceland. Mesolite-scolecite zone alteration in a sample from eastern Iceland contains vesicles completely filled by interlayered chlorite-smectite (*c/s*) and scolecite. Each pore was initially filled with clay rims during early stages of alteration, leaving residual pore space in larger pores that becomes completely filled with scolecite during later stages of alteration (Figure 3.9). Figure 3.9 highlights three vesicles, each exhibiting a different size and shape. Each vesicle is initially filled with rims of *C/S* that are of a consistent thickness between vesicles. The smallest vesicle is almost completely occluded by the *C/S* while the other

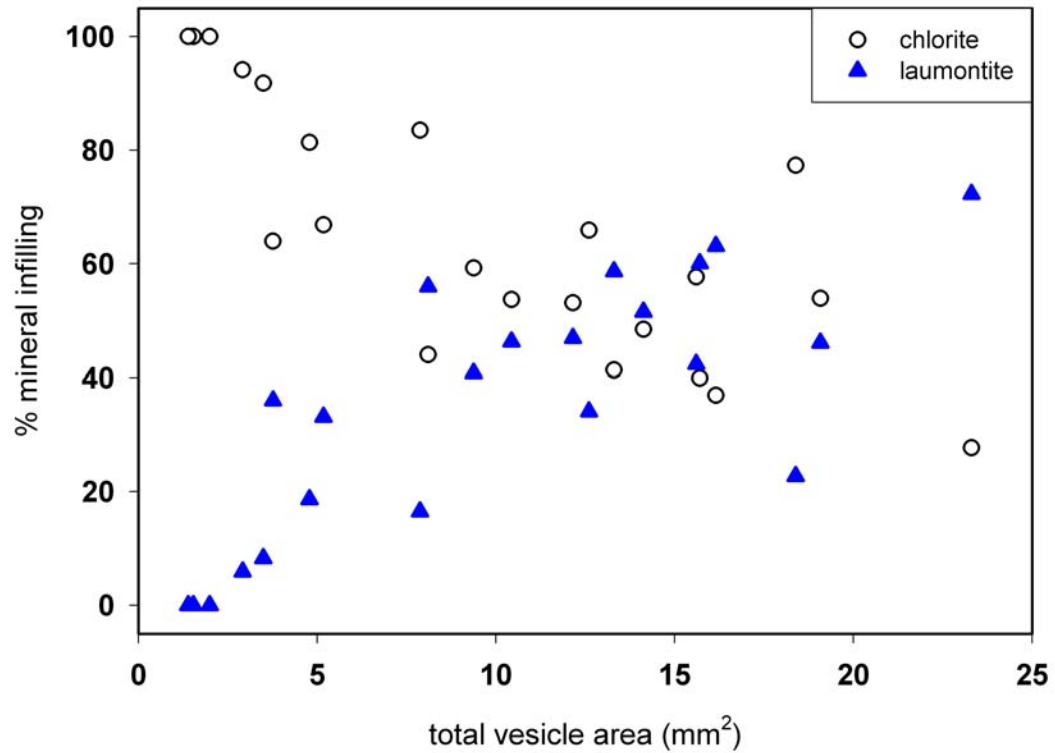


Figure 3.8: Plot shows the percentage of mineral infilling with respect to total vesicle area. Smallest vesicles are completely filled with chlorite. As the vesicle size increases, the percentage of the vesicle filled with chlorite decreases, and the residual space is filled with laumontite.

two retain pore space for scolecite infilling. Measured clay rim thicknesses are given in Table 3.4 and are shown to be consistent throughout the thin section (0.091 +/- 0.02 mm) irrespective of pore size, although a slight variation in thickness is observed in non-ovoid pores (Figure 3.9) due to geometric effects of taking a two-dimensional slice of a three-dimensional object.

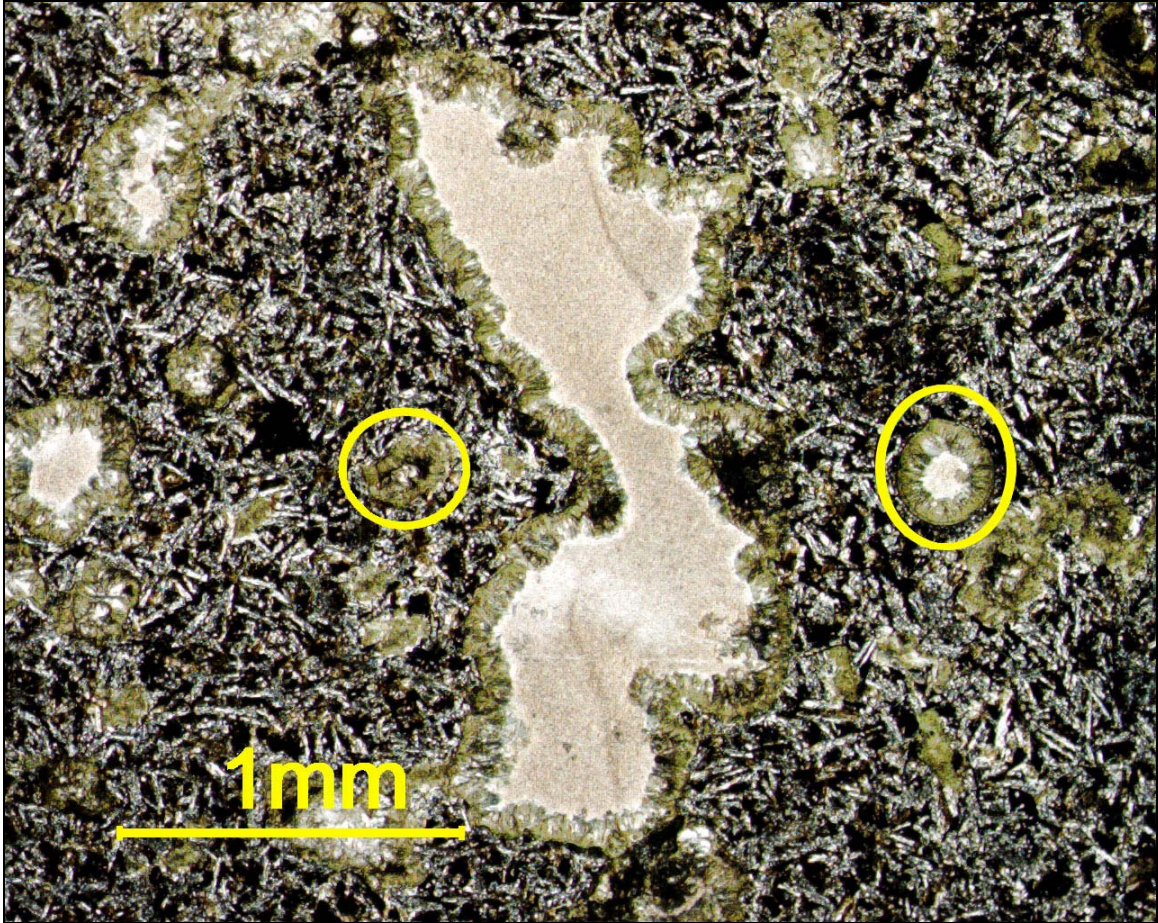


Figure 3.9: Photomicrograph showing a thin section of a mesolite-scolecite zone lava from eastern Iceland. Each pore is filled initially with a chlorite-smectite clay rim; larger pores are subsequently filled with scolecite. Clay rim thicknesses are consistent throughout the section ( $0.10 \pm 0.02$  mm) irrespective of pore size, highlighted by the two circled pores and the larger pore between them. Pores smaller than  $0.1 \text{ mm}^2$  are completely filled with clay.

Digital analysis of pore sizes compared to level of infilling is performed using ArcView and Image J software. The vesicles are analyzed as either filled with both C/S and stilbite or completely occluded by c/s. This information is plotted in Figure 3.10, and shows that pores with an area of  $0.1 \text{ mm}^2$  or less are completely filled with clay, while larger pores are filled with both clay and zeolites due to the consistency in C/S thicknesses.

Table 3.4: Statistical analysis of vesicle areas (mm<sup>2</sup>) and clay rim thicknesses (mm) for sample 94-80 from eastern Iceland.

|                                      | Vesicle Area  | Clay thickness |
|--------------------------------------|---------------|----------------|
| <i>Statistical Data</i>              |               |                |
| n                                    | 229           | 344            |
| Size Range                           | 0.001 – 2.191 | 0.038 – 0.163  |
| Mean                                 | 0.079         | 0.091          |
| Mode                                 | 0.003         | 0.092          |
| St. Dev. <sup>a</sup>                | 0.245         | 0.022          |
| <i>Size Distribution<sup>b</sup></i> |               |                |
| 25%                                  | 0.004         | 0.104          |
| 50%                                  | 0.013         | 0.088          |
| 75%                                  | 0.043         | 0.046          |
| 100%                                 | 2.191         | 0.068          |

<sup>a</sup>Standard Deviation. <sup>b</sup>Percentage of pores  $\leq$  given value.

### Multiple stage zeolite infilling

Initial rims of mafic phyllosilicates were not observed in every analyzed sample, and instead analysis of reaction progress was based on successive levels of zeolite infilling. Observations at the outcrop scale of Site 6 show that all vesicles exhibit thomsonite mineralization while only larger pores progress to crystallization of mesolite. A representative analysis of pore size distributions within the lavas (Table 3.1) shows that pores exhibiting only thomsonite alteration have an average radius of 2.62 mm, while those progressing to mesolite growth have an average radius of 23.76 mm.

## Discussion

### Nature of Porosity and Permeability in Basalts

Previous laboratory studies of unaltered lavas suggest that fluid movement through the rock is dependant on the geometric and spatial aspects of the vesicle space such as the aspect ratio, size, and spacing, thus implying a dependency of fluid movement on the geometry and connectivity of vesicles within the rock. Typical porosity within high vesicular zones of basaltic lavas, however, is highly variable, as shown by the correlation

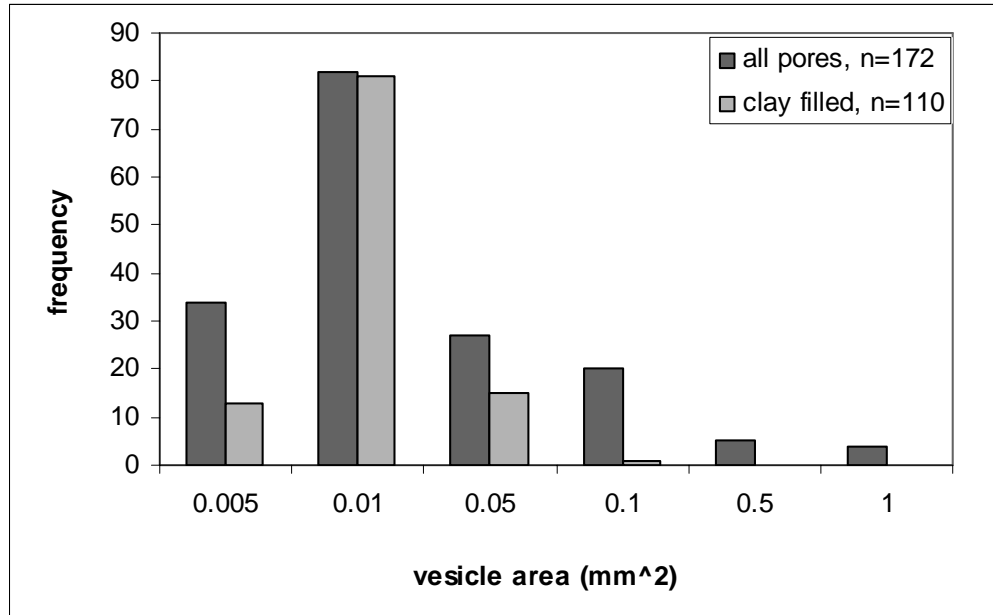


Figure 3.10: Data compiled from digital analysis of mesolite-scolecite zone lava from eastern Iceland (refer to Figure 3.3). Analysis performed at the thin section scale using ArcView and ImageJ software. Plot shows the area variation of all vesicles within the thin section, compared to a random sampling of those filled only with clay. Vesicles exceeding an area of  $0.1 \text{ mm}^2$  are filled with both clay and zeolites, while those smaller than  $0.1 \text{ mm}^2$  are filled completely with clay.

of these observations from basaltic lava samples between different regions. Observations at the outcrop scale of basalts from the NSVG (Figure 3.1) show local areas of little to no porosity surrounded by areas of higher porosity that display much variation in the vesicle size and shape. Analysis of samples in thin section from the NSVG, East Greenland and eastern Iceland (e.g., Figure 3.9) show this occurring even at the mm scale, and it is apparent at this scale that all analyzed samples also exhibited random vesicle-vesicle spacing with little to no interconnection of vesicles.

In spite of the high variability in vesicle size, shape and spacing, all vesicles are partially to completely occluded due to secondary mineralization, implying that there is some other factor controlling fluid flow through the rock and gaining access to pores.

The observed alteration aureoles (Figures 3.2, 3.3 and 3.4) suggest that fluid is transported through the rock along a permeable network of microfractures and connected vesicles. This implies that vesicles will experience secondary alteration regardless of their size shape and spacing as long as they are a part of the fluid flow pathways. This also suggests that the overall permeability of vesicular basalts will remain high even in areas where porosity is low and vesicles are widely distributed. In these areas there will be pathways of high permeability surrounding areas of little to no permeability. The general highlighted region in Figure 3.5, for example, reflects a portion of the sample that was not permeable enough to allow for diffusion of the chemical components necessary to precipitate the secondary mineralization. This may reflect localized lowered permeability due to the absence of the fluid flow pathways necessary for these pores to be part of the permeable network through the lava.

Observation of alteration within the matrix shows these alteration aureoles occurring around and between vesicles. The primary magmatic phases are highly weathered within these aureoles signifying that these are preserving the pathways of fluid movement through the rock during alteration. This suggests that the chemical components necessary to precipitate the vesicle-filling minerals are derived from a spatially restricted region (alteration aureoles) around the vesicle and the fluid pathways over which diffusion occurs. Almost as in a hydrologic system with streams flowing in and out of a lake, where the streams represent the pathways between vesicles and the lake represents the vesicle, the residence time of fluid within the lake is expected to be higher than within the stream due to its larger storage capacity. This means that the alteration

occurring in and around vesicles should be greater than those surrounding the pathways between vesicles, which is seen in Figure 3.2.

The exact nature and initial formation of these pathways are still unclear, though there are many possible explanations. These microfractures are interpreted to be primary features created during formation and cooling of the lava, and not secondary openings due to external stress. Kowallis *et al.* (1982) observed similar microfractures in comparable basalts collected from the IRDP (Iceland Research Drilling Project) borehole in Reydarfjörður, Iceland. Their observations show that the observed microfractures formed during cooling and have since undergone secondary alteration and mineralization due to massive amounts of fluid movement through the basalt. Termination of these fractures appears blunt, rather than the tapered termination typical of newly formed cracks, and the presence of delicate secondary mineral growth within these features would not have survived the stress induced during a secondary cracking process (Kowallis *et al.*, 1982). They also describe fractures coincident with grain boundaries that are often produced by thermal stressing, as well as non-coincident grain boundary fractures produced by local strain variations. Though these fractures increase the accessibility of the basalt matrix to alteration, they do not appear to coincide with those observed in this study as they would not necessarily bridge vesicles and have a major affect on permeability.

Processes experienced by a given lava flow during formation can control the total amount of porosity and can exert a fundamental control on the nature and connectivity of primary pore space. Lava viscosity, lava volatile content, atmospheric pressure, and the degree of crystallinity of the lava, among other factors, all affect both the total

vesicularity of a lava flow and the vesicle size distribution (e.g., Cashman and Mangan, 1994; Sahagian and Maus, 1994; Prousevitch and Sahagian, 1996, 1998; Sahagian *et al.*, 2002). Srouga *et al.* (2004) suggests that autobrecciation processes during cooling of rhyolitic lavas can also enhance the primary porosity within the lava. They suggest that even though these pore spaces are small they may form a connected network, which has potential for increasing the rate of fluid flow through the rock. This potential network, however, is not similar to the network observed in the NSVG basalts as it would not necessarily connect vesicles formed due to trapped gas bubbles within the rock during cooling.

Another possible explanation of the connected network between vesicles observed in this study is the creation of microcracks due to the elongation of bubbles during lava flow and degassing prior to cooling (Saar and Manga, 1999; Mueller *et al.*, 2005). The strong presence of spherical vesicles in the high permeability zones of the cooled lava, however, suggests that these vesicles retain gas after cooling which must later escape through the solid rock. This escaping gas, however, will create a connected network of pathways between vesicles and through the matrix, which can then be reused as a pathway for fluid flow during later events of low-grade alteration. Fluid moving through this network will have a longer residence time in the larger pore spaces, allowing for more of the surrounding matrix to undergo interaction and alteration with the fluid. This will cause larger vesicles to be surrounded by thicker alteration aureoles than the smaller vesicles or thinner connecting pathways, creating alteration aureoles similar to those observed in the NSVG basalts.

### **Controls on Reaction Progress**

The level of reaction progress experienced by a vesicle can be related to the amount and type of secondary mineralization observed within the vesicle, and is strongly dependant on the vesicle size and shape. In general, larger vesicles will retain residual pore space in lower stages of alteration, as observed in the chabazite grade zeolite alteration present in the Greenland sample. Vesicles exposed to higher grades of zeolitization, however, retain no residual pore space and instead the presence of later stage mineralization is controlled by vesicle size.

There is a general trend of secondary mineralization throughout the reaction progress from clay mineral precipitation to progressive stages of zeolite mineral precipitation. Observations show that larger vesicles will progress to later stages of alteration while smaller ones will become closed off earlier in the reaction progress. Also, irregularly shaped vesicles may close off earlier in the reaction progress even with large areas due to constriction caused by the smallest diameter.

In vesicles where clay rims are present, these rims will generally form first and grow to a consistent thickness within a sample irrespective of vesicle size. Thus, smaller vesicles will become completely occluded by clay minerals, while larger ones will show later stage zeolitization. Comparison of clay rim thicknesses between the measured samples discussed above shows that while the thicknesses within a given sample are consistent, variation will occur between lava flows. This shows no relation to vesicle size and instead must be due instead to differences in mineralogy of the rock and of the clay rimming the pores, which is explored in Chapter 4.

All vesicles within basaltic lavas that are connected to the fluid flow pathways can be analyzed and used to interpret the reaction progress experienced by the basalt during

secondary alteration. Interpretations must not be made, however, without close analysis of the vesicle size and shape characteristics, as smaller vesicles and/or those with constrictions due to irregularity in shape may not show the full extent of alteration experienced by the lava. Assessments of the lava chemistry and alteration grade are also necessary, as this will cause a variation in secondary mineral precipitation which will affect interpretations of reaction progress experienced by the lava.

## CHAPTER 4 MODELING OF MINERAL PARAGENESES

### **Introduction**

The field, petrographic, and digital observations summarized in preceding chapters illustrate several key factors involved in the coupled interactions between pore space evolution and mineral paragenesis during low-grade alteration of vesicular lavas. First, there is a definite crystallization sequence of secondary minerals that typically progresses from amorphous silica to mafic phyllosilicates (chlorites and di-octahedral to tri-octahedral smectites) to zeolites, followed in some instances by late zeolites or calcite. Second, these minerals typically occlude primary porosity, with the degree of reaction progress being sensitive to vesicle size. For instance, measured thicknesses of mafic phyllosilicate rims are consistent at the thin section scale irrespective of the size, geometry, and connectivity of vesicles. This same phenomenon is manifested by the vesicle-size dependence of occurrence of late stage zeolites and preservation of residual pore space. Third, a notable feature observed in these rocks is the presence of reaction aureoles around primary pore spaces and networking microfractures. Alteration aureoles are clearly visible as lighter areas surrounding the vesicles and microfractures (Figure 3.3). These aureoles potentially represent fluid pathways through the matrix during alteration, suggesting that the chemical components necessary to precipitate the vesicle-filling minerals are derived from a spatially restricted region (alteration aureoles) around the vesicle and the fluid pathways over which diffusion occurs.

This chapter describes the results of irreversible reaction path modeling conducted in order to interpret these features of low-grade metabasalts. These calculations are used to 1) explain the genesis of the sequence of secondary minerals formed during alteration; and 2) interpret the evolution of porosity during alteration. The results are then used in concert with my field, petrographic, and digital observations to develop a geometric model explaining the relationship between pore size, mineral authigenesis, and porosity evolution during alteration.

### **Methods**

Mineral paragenesis and porosity evolution during low grade alteration are modeled using the irreversible reaction path code EQ3/6 (Wolery, 1979; Wolery *et al.*, 1990). The program computes the compositional evolution in systems of water-rock interaction during reactive mass transfer assuming local and partial equilibrium between an aqueous fluid and coexisting mineral and gas phases (Wolery, 1979). Basic inputs to the code are the composition of the starting fluid, temperature (with pressure corresponding to liquid-vapor equilibrium for water), and the composition and abundances of phases that will be reacted with the fluid. In all models presented below, the initial fluid was taken to be 1 kg of dilute aqueous fluid undersaturated with respect to all minerals that interacts with a lava containing 20% initial porosity (or a bulk rock volume of 4 liters).

In the first set of models, a simplified basalt composition was created as an input for the program (Table 4.1 and 4.2) that is representative of the mineral modes, mineral compositions, and the bulk rock composition of olivine tholeiites in the North Shore Volcanic Group (after Brannon, 1984). The model simulates titration of 4 liters of lava into 1 kg of a dilute aqueous solution (initially no saturated phases) in a closed system at

Table 4.1: Bulk rock composition for olivine tholeiite basalt (wt %)

| Oxide                          | Calculated | Sampled* | Average* | Range*      |
|--------------------------------|------------|----------|----------|-------------|
| SiO <sub>2</sub>               | 47.75      | 47.26    | 48.07    | 47.6 – 48.5 |
| Al <sub>2</sub> O <sub>3</sub> | 18.01      | 16.86    | 16.80    | 16.5 – 17.4 |
| CaO                            | 13.67      | 11.03    | 10.93    | 10.6 – 11.2 |
| Na <sub>2</sub> O              | 2.26       | 2.51     | 2.48     | 2.38 – 2.64 |
| K <sub>2</sub> O               | 0.12       | 0.31     | 0.28     | 0.13 – 0.44 |
| MgO                            | 6.44       | 6.74     | 6.98     | 6.25 – 7.56 |
| FeO                            | 9.67       | 11.98    | 12.20    | 11.4 – 12.6 |
| TiO <sub>2</sub>               | 1.83       | 1.67     | 1.71     | 1.43 – 1.93 |

\*Values from Brannon, 1984

Table 4.2: Modal abundances and compositions of primary mineral phases in olivine tholeiite

| Initial Phase | End-member   | X <sup>1</sup> | Moles <sup>2</sup> | Volume % | Mass    | Rate <sup>3</sup> |
|---------------|--------------|----------------|--------------------|----------|---------|-------------------|
| Feldspar      |              |                | 23.60              | 59.30    | 6425.79 | 1                 |
|               | Anorthite    | 65.00          |                    |          |         |                   |
|               | Albite       | 33.80          |                    |          |         |                   |
|               | Orthoclase   | 1.20           |                    |          |         |                   |
| Pyroxene      |              |                | 27.40              | 24.10    | 3059.99 | 10                |
|               | Wollastonite | 42.00          |                    |          |         |                   |
|               | Enstatite    | 43.50          |                    |          |         |                   |
| Olivine       |              |                | 4.30               | 11.00    | 708.31  | 100               |
|               | Forsterite   | 63.90          |                    |          |         |                   |
|               | Fayalite     | 36.10          |                    |          |         |                   |
| Ilmenite      |              |                | 2.50               | 2.00     | 37931   | 1                 |
| Magnetite     |              |                | 1.70               | 1.90     | 393.62  | 1                 |
| Glass         |              |                | 2.60               | 1.70     | 182.21  | 1000              |

<sup>1</sup>Molar percentages are represented by X. <sup>2</sup>Moles are for 4 liters of basalt. <sup>3</sup>Relative reaction rates represent dissolution rates of mineral phases.

70°C, P<sub>sat</sub>. This bulk composition and temperature condition is typical of the thomsonite-mesolite zone alteration found in the NSVG. Two isochemical versions of this model were run that differed only in the relative rates of dissolution of components into the fluid. In the first, the lava was titrated into the fluid stoichiometrically. In the second, the same bulk composition was distributed among separate primary phases in their relative modal proportions and allowed to react at relative rates that approximate differences in bulk dissolution rates (Table 4.2; Gislason and Eugster, 1987; Palandri and

Kharaka, 2004). Thermodynamic data for this model was taken from the “combined” database provided with EQ3/6. Precipitation of epidote solid solutions, grandite garnet solid solutions, prehnite, and tremolite was suppressed in the model as these species are not expected to form under these conditions but are predicted to be stable using the data in the combined database.

The second model uses a calculated phase assemblage that is representative of the mineral modes, mineral compositions and bulk rock compositions of a sampled basaltic andesite (sample NS04-14 from sampling site 4; see Table 4.3) from the NSVG. This sample is representative of upper zeolite facies conditions, although it is somewhat more silicic than most of the NSVG. Because of the extensive matrix alteration of the sample that precluded optical determination of primary mineral modes, the relative abundances of primary minerals were calculated with the computer program KWare Magma (Wohletz, 1999) by assuming a CIPW normative mineralogy of the unaltered basalt. The resulting mineralogy (Table 4.4) compares favorably with previous observations of andesites in the NSVG (Brannon, 1984; Schmidt, 1990). Representative mineral formulas were taken from Chapter 2 along with reported values by Brannon (1984) and Schmidt (1990). In this model, the temperature was set at 120°C (typical of laumontite zone alteration; cf. Chapter 3), and the primary phases were titrated in their relative modal proportions using relative rate constants that approximate differences in bulk dissolution rates (Table 4.4; Gislason and Eugster, 1987; Palandri and Kharaka, 2004). Due to the simpler alteration assemblage encountered in this sample, the calculations were performed with a database based on SUPCRT92 (Johnson *et al.*, 1992) augmented with data for ilmenite from Stefansson (2001) and hydroxyapatite and daphnite from the

Table 4.3: Calculated anhydrous bulk composition of basaltic andesite before and after reaction.

|                                | Ilmenite | Hydroxyl-<br>Apatite | Clino-<br>Pyroxene | Ortho-<br>Pyroxene | Albite | Anorthite | K-Feldspar | Quartz | Hematite | Chlorite | Laumontite | Whole<br>Rock |
|--------------------------------|----------|----------------------|--------------------|--------------------|--------|-----------|------------|--------|----------|----------|------------|---------------|
| <i>Unaltered Andesite</i>      |          |                      |                    |                    |        |           |            |        |          |          |            |               |
| SiO <sub>2</sub>               | 0.00     | 0.00                 | 1.51               | 14.77              | 23.12  | 4.98      | 6.52       | 6.86   | 0.00     | 0.00     | 0.00       | 57.67         |
| TiO <sub>2</sub>               | 2.26     | 0.00                 | 0.00               | 0.00               | 0.00   | 0.00      | 0.00       | 0.00   | 0.00     | 0.00     | 0.00       | 2.26          |
| Al <sub>2</sub> O <sub>3</sub> | 0.00     | 0.00                 | 0.00               | 0.00               | 6.54   | 4.23      | 1.84       | 0.00   | 0.00     | 0.00     | 0.00       | 12.62         |
| FeO <sup>a</sup>               | 2.03     | 0.00                 | 0.60               | 11.36              | 0.00   | 0.00      | 0.00       | 0.00   | 0.00     | 0.00     | 0.00       | 13.98         |
| MgO                            | 0.00     | 0.00                 | 0.17               | 3.54               | 0.00   | 0.00      | 0.00       | 0.00   | 0.00     | 0.00     | 0.00       | 3.72          |
| CaO                            | 0.00     | 0.56                 | 0.74               | 0.00               | 0.00   | 2.33      | 0.00       | 0.00   | 0.00     | 0.00     | 0.00       | 3.62          |
| Na <sub>2</sub> O              | 0.00     | 0.00                 | 0.00               | 0.00               | 3.98   | 0.00      | 0.00       | 0.00   | 0.00     | 0.00     | 0.00       | 3.98          |
| K <sub>2</sub> O               | 0.00     | 0.00                 | 0.00               | 0.00               | 0.00   | 0.00      | 1.70       | 0.00   | 0.00     | 0.00     | 0.00       | 1.70          |
| P <sub>2</sub> O <sub>5</sub>  | 0.00     | 0.42                 | 0.00               | 0.00               | 0.00   | 0.00      | 0.00       | 0.00   | 0.00     | 0.00     | 0.00       | 0.45          |
| Total                          | 4.29     | 0.98                 | 3.02               | 29.66              | 33.64  | 11.54     | 10.06      | 6.86   | 0.00     | 0.00     | 0.00       | 100.00        |
| <i>Altered Andesite</i>        |          |                      |                    |                    |        |           |            |        |          |          |            |               |
| SiO <sub>2</sub>               | 0.00     | 0.00                 | 5.97               | 0.00               | 23.15  | 0.00      | 6.52       | 13.96  | 0.00     | 6.20     | 1.87       | 57.67         |
| TiO <sub>2</sub>               | 2.26     | 0.00                 | 0.00               | 0.00               | 0.00   | 0.00      | 0.00       | 0.00   | 0.00     | 0.00     | 0.00       | 2.26          |
| Al <sub>2</sub> O <sub>3</sub> | 0.00     | 0.00                 | 0.00               | 0.00               | 6.55   | 0.00      | 1.84       | 0.00   | 0.00     | 3.51     | 0.79       | 12.69         |
| FeO <sup>a</sup>               | 2.03     | 0.00                 | 1.79               | 0.00               | 0.00   | 0.00      | 0.00       | 0.00   | 2.90     | 7.42     | 0.00       | 14.13         |
| MgO                            | 0.00     | 0.00                 | 1.00               | 0.00               | 0.00   | 0.00      | 0.00       | 0.00   | 0.00     | 2.77     | 0.00       | 3.78          |
| CaO                            | 0.00     | 0.59                 | 2.79               | 0.00               | 0.00   | 0.00      | 0.00       | 0.00   | 0.00     | 0.00     | 0.44       | 3.82          |
| Na <sub>2</sub> O              | 0.00     | 0.00                 | 0.00               | 0.00               | 3.98   | 0.00      | 0.00       | 0.00   | 0.00     | 0.00     | 0.00       | 3.98          |
| K <sub>2</sub> O               | 0.00     | 0.00                 | 0.00               | 0.00               | 0.00   | 0.00      | 1.70       | 0.00   | 0.00     | 0.00     | 0.00       | 1.70          |
| P <sub>2</sub> O <sub>5</sub>  | 0.00     | 0.45                 | 0.00               | 0.00               | 0.00   | 0.00      | 0.00       | 0.00   | 0.00     | 0.00     | 0.00       | 0.45          |
| Total                          | 4.28     | 1.05                 | 11.55              | 0.00               | 33.68  | 0.00      | 10.07      | 13.96  | 2.90     | 19.90    | 3.10       | 100.48        |

<sup>a</sup>Total Fe reported as FeO

combined database. In addition, ideal chlorite, plagioclase, and orthopyroxene solid solutions were defined. Andradite and grossular garnet, prehnite, annite, tremolite, epidote, talc, analcime, and magnetite are all phases that are suppressed in the input file of the model so that they will not form as part of the alteration sequence.

Table 4.4: Reactant phase composition, abundance, and relative dissolution rate in basaltic andesite used as input for reaction path model.

| Initial Phase | End-member   | X <sup>1</sup> | Moles <sup>2</sup> | Volume % | Mass    | Rate <sup>3</sup> |
|---------------|--------------|----------------|--------------------|----------|---------|-------------------|
| Feldspar      |              |                | 24.49              | 62.39    | 6569.50 | 10                |
|               | Anorthite    | 20.12          |                    |          |         |                   |
|               | Albite       | 62.33          |                    |          |         |                   |
|               | Orthoclase   | 17.55          |                    |          |         |                   |
| Orthopyroxene |              |                | 29.23              | 23.63    | 3527.30 | 100               |
|               | Enstatite    | 35.7           |                    |          |         |                   |
|               | Ferrosilite  | 64.3           |                    |          |         |                   |
| Clinopyroxene |              |                | 2.99               | 2.71     | 353.22  | 100               |
|               | Diopside     | 100.00         |                    |          |         |                   |
|               | Hedenbergite | 0.00           |                    |          |         |                   |
| Quartz        |              |                | 13.58              | 7.70     | 815.86  | 1                 |
| Ilmenite      |              |                | 3.36               | 2.66     | 510.21  | 100               |
| Apatite-OH    |              |                | 0.23               | 0.91     | 114.72  | 100,000           |

<sup>1</sup>Molar percentages are represented by X. <sup>2</sup>Moles are for 4 liters of basalt. <sup>3</sup>Relative reaction rates represent dissolution rates of mineral phases.

## Results

### Mineral parageneses

Figures 4.1A and 4.1B depicts the mineralogic evolution of an olivine tholeiite as a function of reaction progress ( $\xi$ ) assuming either congruent dissolution of the bulk lava (4.1A) or dissolution controlled by the relative dissolution rates of the primary minerals (4.1B). Note that the plots in Figure 4.1 represent the relative abundances of minerals in terms of absolute volume. A value of  $\log \xi$  of -10 corresponds to the beginning of reaction; a value of 0 represents completion of reaction.

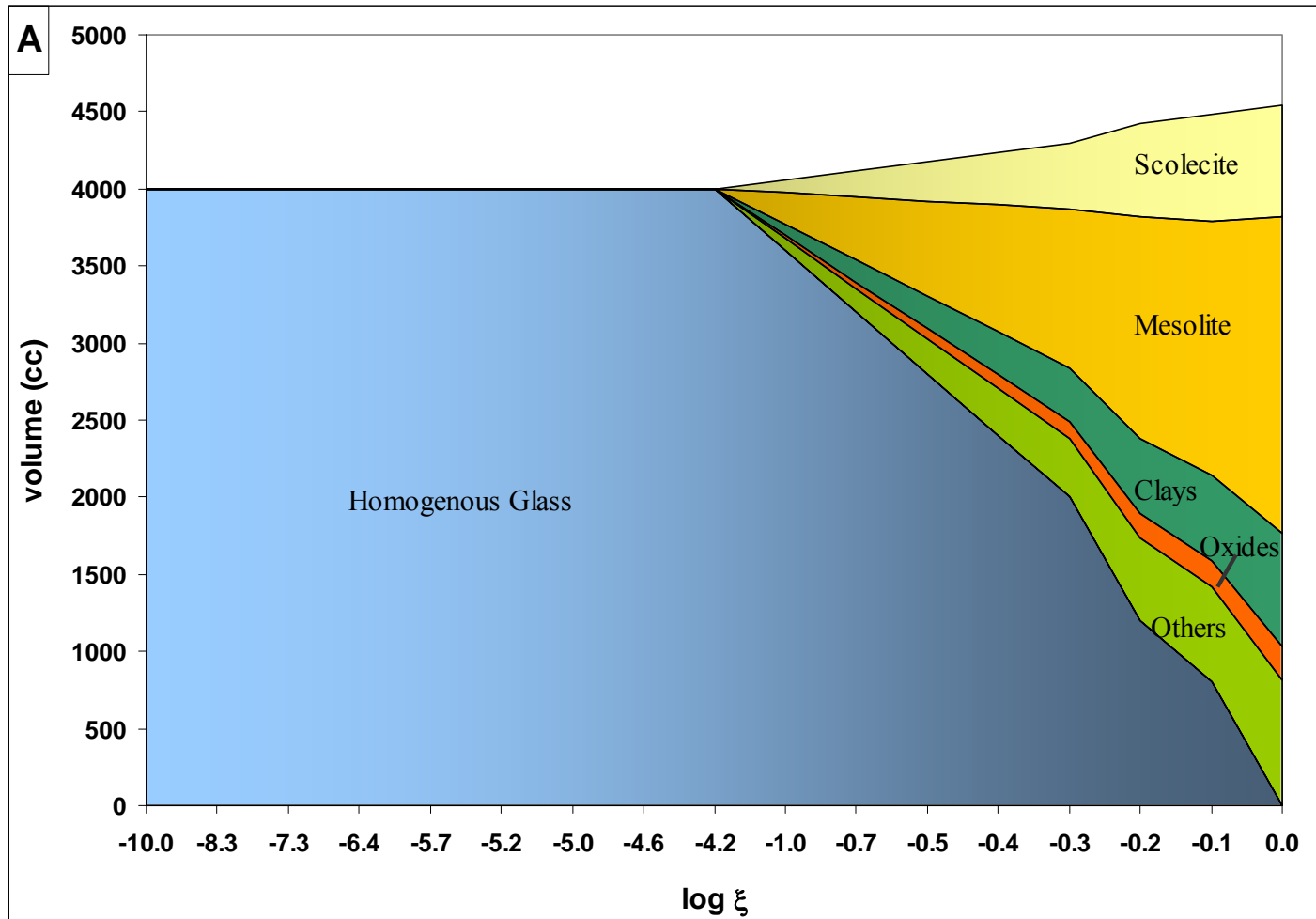


Figure 4.1: Mineralogic composition of lavas as a function of reaction progress for models describing A) homogeneous dissolution of an olivine tholeiite at 70 °C; B) incongruent dissolution of an olivine tholeiite controlled by relative dissolution rates of primary minerals at 70 °C; and C) incongruent dissolution of a basaltic andesite controlled by the relative dissolution rates of primary minerals at 120 °C.

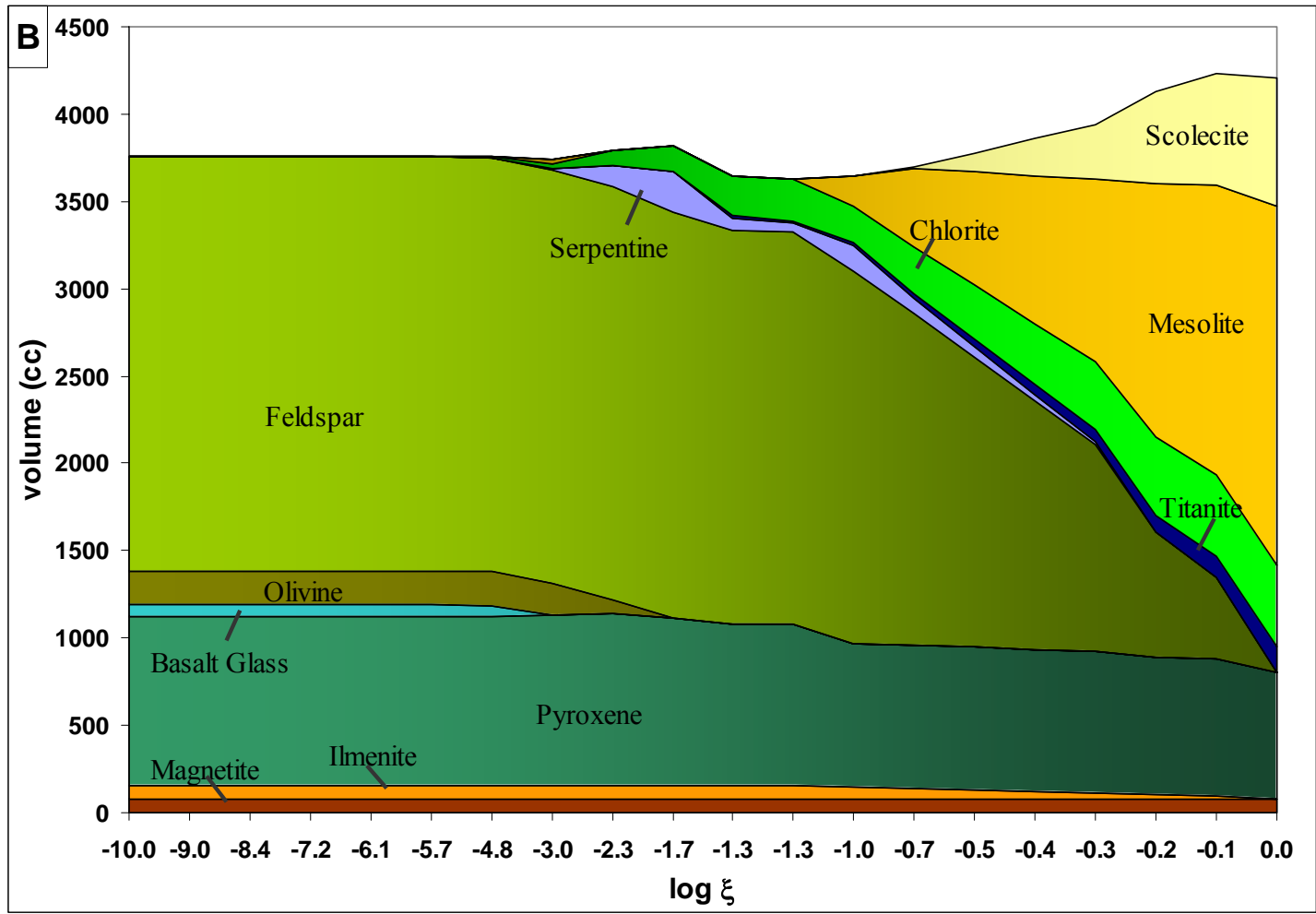


Figure 4.1: (continued)

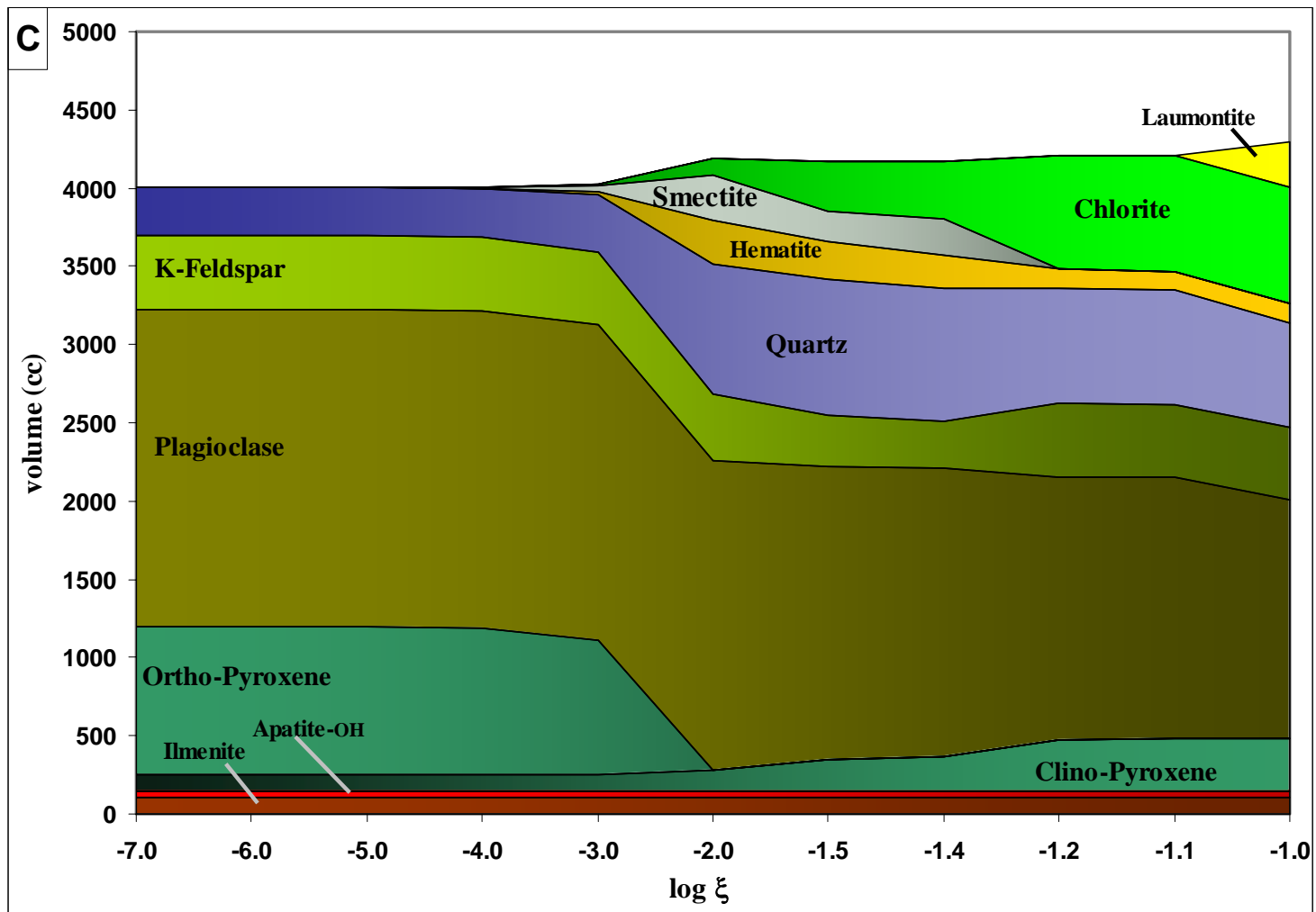


Figure 4.1: (continued)

For the congruent dissolution model in Figure 4.1A, the onset of secondary mineral precipitation occurs simultaneously for all phases. The zeolites mesolite and scolecite comprise the largest fraction of the alteration assemblage. Clay minerals predicted by the model consist mostly of chlorite with minor precipitation of biotite and saponite. Oxides have the least affect on volume increase with precipitation mostly occurring as titanite, though magnetite, rutile, hematite, and gibbsite also form. The remaining minerals are grouped as others. Diopside dominates the volume contribution of these other minerals during the run, with only minor amounts of clinozoisite. At the final stage of the model the homogenous glass has dissolved completely and all volume in the system consists of secondary minerals.

Figure 4.1B depicts the mineralogic evolution of an olivine tholeiite consisting initially of glass, olivine, pyroxene, feldspar, ilmenite and magnetite in their modal proportions. Each primary phase dissolves to various levels of completion at different stages of the reaction controlled by their relative reaction rate. Contrary to the results of the congruent dissolution model, the onset of secondary mineral precipitation varies between phases. The complete dissolution of glass and olivine, along with the compositional change of pyroxene from  $\text{Wo}_{0.42}\text{En}_{0.435}\text{Fs}_{0.145}$  to diopside, donates iron and magnesium needed to form the chlorite and serpentine clay minerals relatively early in the reaction. The complete dissolution of feldspar donates the calcium and sodium needed to form the zeolites mesolite and scolecite. All potassium dissolved from the feldspar remains in the aqueous phase. Ilmenite completely dissolves, donating the titanium for precipitation of titanite. Magnetite is the only primary magmatic phase that remains stable throughout the reaction.

Although both of the above models predict roughly the same mineral assemblage, they differ in their predictions of the timing of mineral formation. Both models predict a mineral assemblage dominated by the zeolites mesolite and scolecite along with pyroxene and mafic phyllosilicate, consistent with what is observed in olivine tholeiites within the thomsonite-mesolite zone of the NSVG. However, the model depicted in Figure 4.1B more closely approximates the mineral parageneses observed in zeolite facies metabasalts than that shown in Figure 4.1A in terms of the relative abundance of secondary mineral phases and their relative sequence of precipitation. Early formation of mafic phyllosilicate phases relative to zeolites that is observed in the relative timing of mineral precipitates within vesicles is a consequence of the differential reaction rates of primary mineral phases in the incongruent dissolution model.

Comparison of the results for olivine tholeiite dissolution either congruently or incongruently (Figures 4.1A and 4.1B) illustrates the importance of relative dissolution rates in controlling reaction paths. Alteration of the olivine tholeiite as a homogenous glass (4.1A) shows the onset of secondary mineral precipitation to occur simultaneously for all phases, and allows the large volume increase due to zeolitization to dominate throughout precipitation. These results do not correlate to the petrographic observations of altered basalts from the NSVG, indicating that the observed paragenesis of early mafic phyllosilicates followed by zeolites can not be explained by stoichiometric reaction of the basalt, but rather is a consequence of differential dissolution rates for primary basalt phases as shown in Figure 4.1B, and in the incongruent dissolution of basaltic andesite in Figure 4.1C. Consequently, modeling of the mineral paragenesis observed in the basaltic andesite employed only an incongruent dissolution approach.

Figure 4.1C depicts the mineralogic evolution of a basaltic andesite during interaction with dilute meteoric solutions at 120 °C. Input and output values for the moles, volume, and mass of mineral phases are compared to calculated values and shown in Table 4.5. The final phase assemblage listed in Table 4.5 consists of hematite, chlorite, laumontite, K-feldspar, albite, clinopyroxene, quartz, hydroxyapatite, and ilmenite, which is essentially the assemblage observed in sample NS04-14. The output

Table 4.5: Mole, volume and mass amounts in unaltered and altered andesite for the computer (modeled) and mathematical (calculated) models.

|                  | <b>Moles*</b> |         | <b>Volume %</b> |         | <b>Mass (g)</b> |          |
|------------------|---------------|---------|-----------------|---------|-----------------|----------|
|                  | Calculated    | Modeled | Calculated      | Modeled | Calculated      | Modeled  |
| <b>Unaltered</b> |               |         |                 |         |                 |          |
| Quartz           | 13.58         | 13.58   | 7.70            | 7.70    | 815.85          | 815.86   |
| K-Feldspar       | 4.30          | 4.30    | 11.70           | 11.69   | 1196.42         | 1196.40  |
| Albite           | 15.26         | 15.26   | 38.24           | 38.30   | 4000.77         | 4002.50  |
| Anorthite        | 4.93          | 4.93    | 12.43           | 12.41   | 1372.44         | 1370.60  |
| Ilmenite         | 3.36          | 3.36    | 2.66            | 2.66    | 510.21          | 510.21   |
| Apatite-OH       | 0.23          | 0.23    | 0.91            | 0.91    | 116.55          | 114.72   |
| Clinopyroxene    | 2.99          | 2.99    | 2.71            | 2.71    | 353.22          | 353.22   |
| Orthopyroxene    | 29.23         | 29.23   | 23.64           | 23.63   | 3527.43         | 3527.30  |
| Total            | 73.88         | 73.88   | 100.00          | 100.00  | 11892.89        | 11890.81 |
| <b>Altered</b>   |               |         |                 |         |                 |          |
| Quartz           | 27.50         | 29.30   | 14.39           | 15.48   | 1652.24         | 1760.20  |
| K-Feldspar       | 4.28          | 4.30    | 10.75           | 10.88   | 1192.05         | 1196.40  |
| Albite           | 15.20         | 15.26   | 35.15           | 35.56   | 3986.04         | 4002.20  |
| Ilmenite         | 3.34          | 3.36    | 2.44            | 2.48    | 507.07          | 510.21   |
| Apatite-OH       | 0.25          | 0.23    | 0.92            | 0.85    | 123.72          | 114.72   |
| Clinopyroxene    | 5.90          | 5.09    | 9.14            | 7.84    | 1366.98         | 1112.52  |
| Hematite         | 4.29          | 3.97    | 3.00            | 2.80    | 342.73          | 634.10   |
| Chlorite         | 4.07          | 3.53    | 19.81           | 17.34   | 2355.68         | 2319.75  |
| Laumontite       | 0.92          | 1.40    | 4.40            | 6.77    | 366.38          | 659.30   |
| Total            | 65.76         | 66.43   | 100.00          | 100.00  | 11892.89        | 12309.40 |

\*Values are for 4 liters of Basalt

generated by the model shows mass remaining relatively constant, with an increase of only 3.5%. Mass increase largely reflects hydration of the lava. The bulk composition of the lava is relatively unchanged other than this gain of H<sub>2</sub>O, as shown by the comparison of the initial and final bulk compositions shown in Table 4.3. Early, complete dissolution

of orthopyroxene and anorthite contributes the iron, magnesium and calcium needed to create the hematite, chlorite and laumontite observed in the sample. Iron released early in the reaction progress re-precipitates as hematite until enough magnesium and aluminum are present in the aqueous phase to reach chlorite saturation. Chlorite is the modally most important secondary mineral until laumontite saturation is reached, which is the last mineral to form. Table 4.6 lists the compositions of mineral solids solutions present at the end of the model. The anorthite component in plagioclase is lost during dissolution, and all remaining plagioclase is completely albitized.

Table 4.6: Phase compositions and abundances at end of reaction path for basaltic andesite given in their respective end-members and molar proportions (where solid solutions exist), moles, volume %, and mass.

| Final Phase   | End-member   | X <sup>1</sup> | Moles <sup>2</sup> | Volume % | Mass    |
|---------------|--------------|----------------|--------------------|----------|---------|
| Feldspar      |              |                | 19.56              | 46.44    | 1196.40 |
|               | Anorthite    | 0.00           |                    |          |         |
|               | Albite       | 78.02          |                    |          |         |
|               | Orthoclase   | 21.98          |                    |          |         |
| Clinopyroxene |              |                | 5.09               | 7.84     | 1112.52 |
|               | Diopside     | 93.07          |                    |          |         |
|               | Hedenbergite | 6.93           |                    |          |         |
| Chlorite      |              |                | 3.53               | 17.34    | 2319.75 |
|               | Clinochlore  | 35.23          |                    |          |         |
|               | Daphnite     | 64.77          |                    |          |         |
| Laumontite    |              |                | 1.40               | 6.77     | 659.30  |
| Hematite      |              |                | 3.97               | 2.80     | 634.10  |
| Quartz        |              |                | 29.30              | 15.48    | 1760.20 |
| Ilmenite      |              |                | 3.36               | 2.48     | 510.21  |
| Apatite-OH    |              |                | 0.23               | 0.85     | 114.72  |

<sup>1</sup>Molar percentages are represented by X. <sup>2</sup>Moles are for 4 liters of basalt.

Orthopyroxene compositions are essentially constant while this phase is present in the model. Clinopyroxene increases in modal abundance with reaction progress, and also becomes steadily more Fe-rich. Chlorite compositions are initially clinochlore-rich, but become more daphnite rich with increasing reaction progress.

The bulk solid composition is in excellent agreement with that calculated by assuming that the lava completely altered to the observed mineral assemblage. The lower half of Table 4.5 shows the modal abundances of secondary minerals determined through a normative calculation analogous to that of the CIPW norm, but with the observed secondary mineral assemblage in place of primary igneous phases. These calculations indicate the creation of chlorite, laumontite, hematite, and an increase in clinopyroxene and quartz through complete destruction of the orthopyroxene and the anorthite. All other primary phases including the ilmenite, hydroxyl-apatite, albite, and k-feldspar show no change in their compositions or amounts present throughout alteration.

### **Volume Changes During Alteration**

Volume change observed during the reaction of each modeled run can be observed both as the total volume change and as the instantaneous volume change at each step of the reaction. The total volume change of the system with respect to reaction progress is presented in Figure 4.1. In each run, the mass is held constant throughout the reaction to maintain a constant initial primary porosity of ~20%; therefore, any volume increase observed in each run is a result of the formation of secondary minerals with higher molar volumes than initial primary magmatic phases. Reaction of the olivine tholeiite shows a volume increase of 14% at the end of reaction (Figures 4.1A and 4.1B), while reaction of the basaltic andesite in (Figure 4.1C) shows an 8% increase in volume.

Instantaneous volume change, i.e., the net change in amount of products relative to reactants at each  $\xi$  step, is calculated for each step of the reaction and depicted in Figure 4.2. Negative values along the y-axis of this plot correspond to a volume decrease in the system, which can also be explained as porosity increase. Conversely, positive values

correspond to a volume increase which relates to porosity destruction. In each modeled reaction, there is an initial volume decrease in the system creating a subtle increase in porosity before there is a more significant volume increase causing a destruction or occlusion of primary porosity. In the congruent dissolution model for olivine tholeiite, the positive volume change occurs at the onset of mineral precipitation, and is related to the formation of the whole phase assemblage. For the incongruent dissolution model, the instantaneous volume change becomes positive early due to the formation of serpentine and chlorite and before formation of zeolites. The need for space during early phyllosilicate formation may account for the prominent clay rims observed in many samples. A similar trend is observed for reaction of the basaltic andesite.

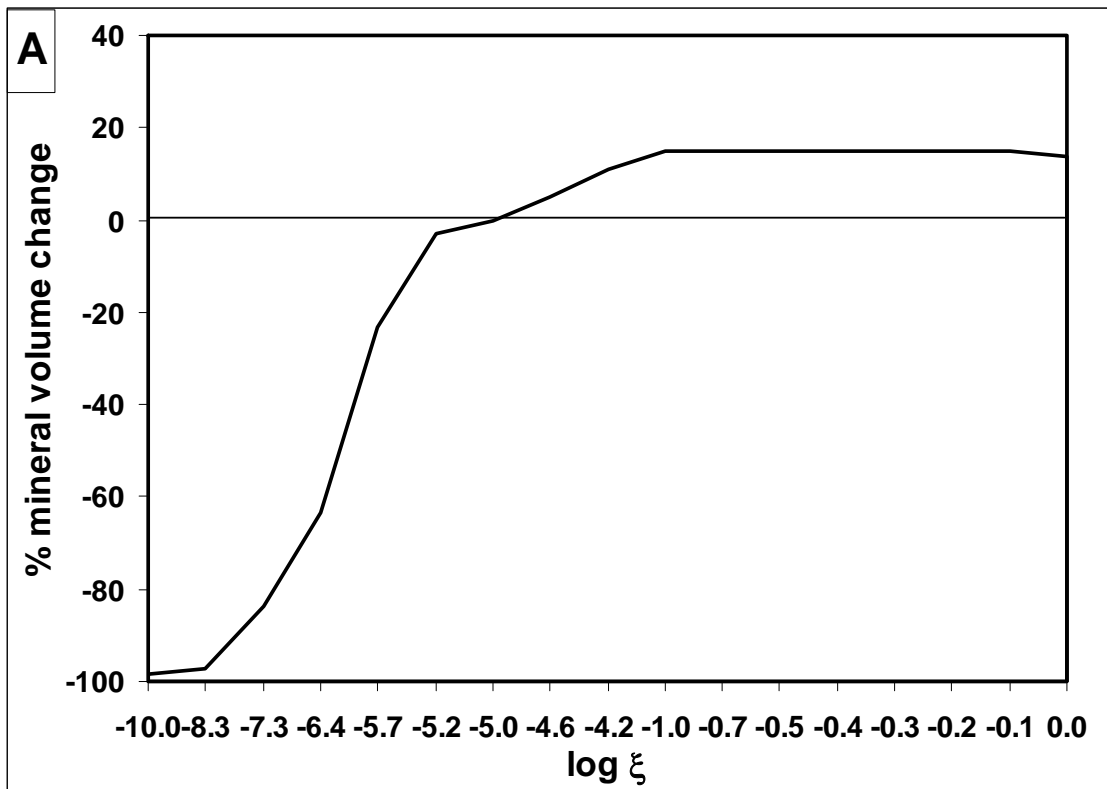


Figure 4.2: Instantaneous change in total mineral volume as a function of reaction progress. Panels A, B, and C correspond to models shown in Figure 4.1.

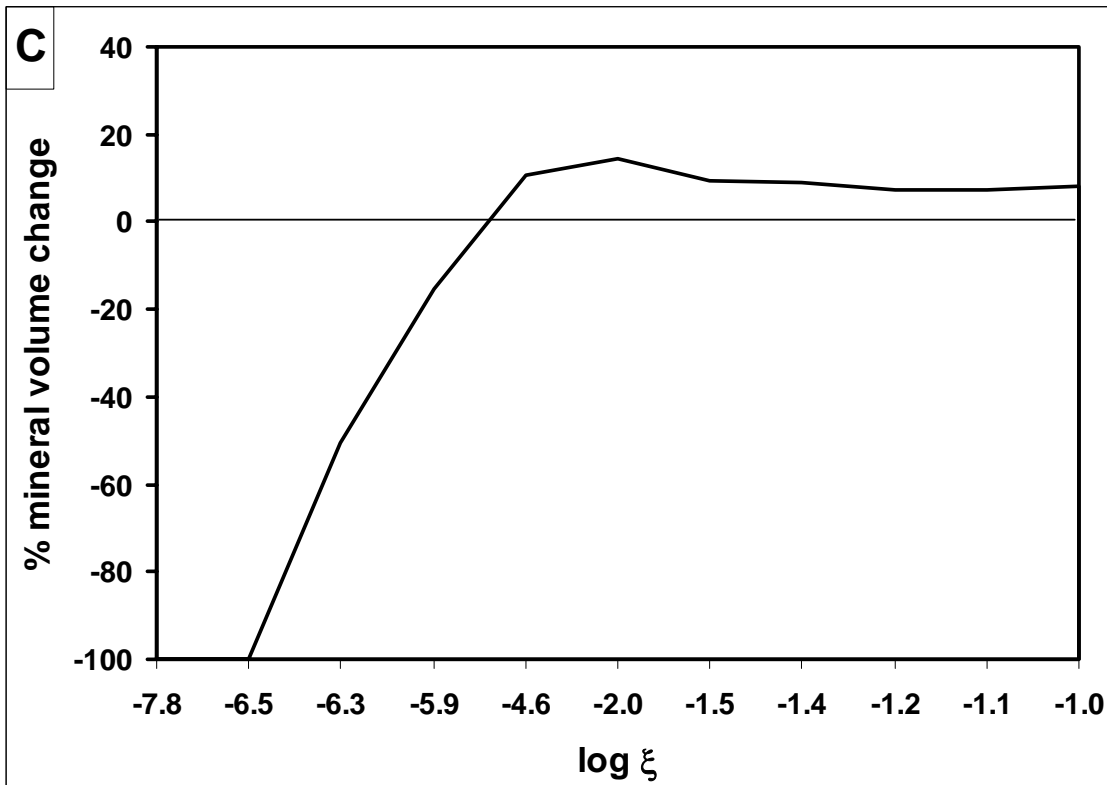
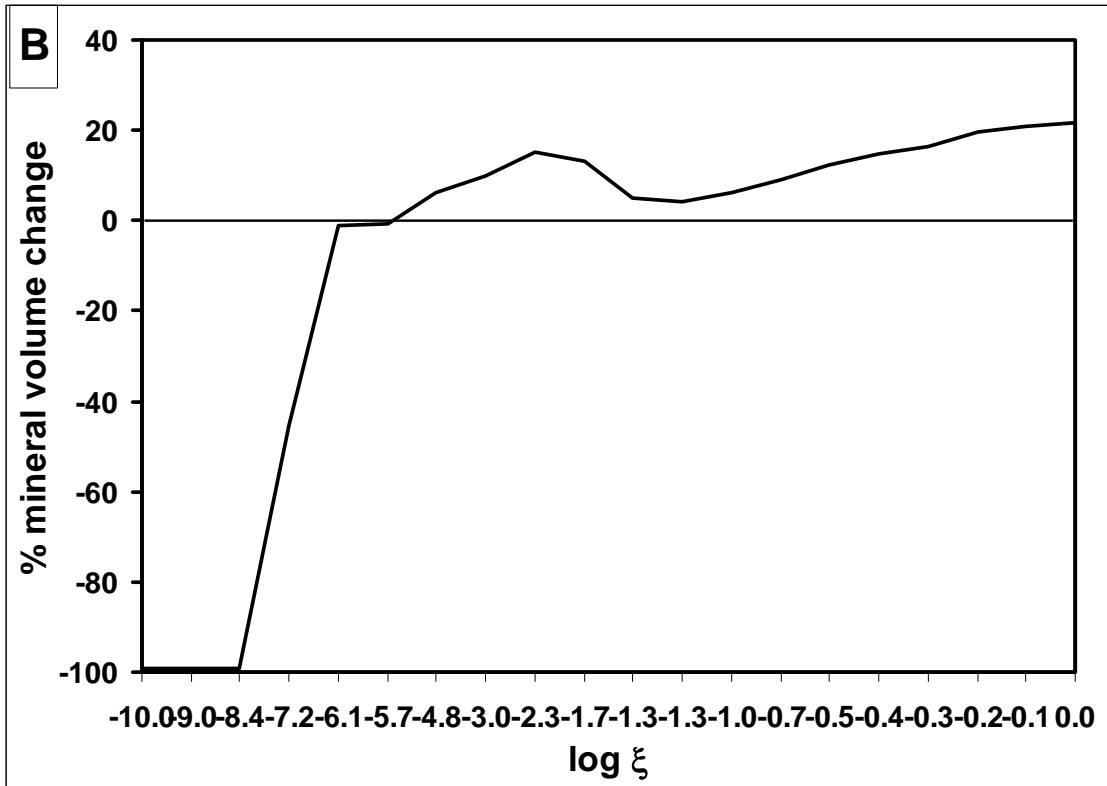


Figure 4.2: (continued)

## CHAPTER 5 DISCUSSION

### **Reaction Progress in Low-Grade Metabasalts**

Petrographic observations of low-grade metabasalts (cf. Chapter 3) show a definite progression from mafic phyllosilicates to zeolites to late stage zeolites. In some cases, residual pore space is left over after alteration. Alteration within the matrix is dominated by the presence of Fe(Ti) oxides, and mafic phyllosilicates along with variable amounts of silica, feldspars (albite and microcline at higher grades), and zeolites. Clinopyroxenes tend to survive alteration, while other mafic phases (olivine, orthopyroxene, and glass) tend to be completely altered, often pseudomorphically. The reaction path modeling described in Chapter 4 indicates that this is a consequence of incongruent dissolution of the lavas. The sequence of secondary mineralization is controlled by the differential dissolution rates for primary basaltic phases as well as the volume change throughout the reaction due to the variation in molar volumes of secondary minerals. In the olivine tholeiite (Figure 4.1B), the first modeled minerals to form are titanite, serpentines and chlorite brought on by early dissolution of olivine and basaltic glass, which have the highest dissolution rates (Table 4.2). Figure 4.2B shows an instantaneous volume increase of 17% related to the high molar volumes of the serpentines and chlorites. This positive volume change forces precipitation to progress from the matrix to the vesicle in search of available pore space, forming observed clay rims lining vesicle walls.

The onset of feldspar and pyroxene dissolution as the alteration progresses leads to zeolite precipitation. There is still precipitation of the early forming minerals, but the

system becomes dominated by these zeolites due to their large molar volumes compared to both the primary basaltic phases and the mafic phyllosilicates. They create a final instantaneous volume increase of 14% (Figure 4.2B), causing occlusion of any residual pore space within vesicles. The model predicts mesolite to form first with late stage formation of scolecite, which is a common sequence observed in samples exhibiting mesolite-scolecite zone alteration (pers. com.; Neuhoff, P.S., 2006).

A similar progression of secondary mineralization is seen in the modeled alteration of basaltic andesite (Figure 4.1C), where hematite, smectite and chlorite are the first minerals to form with later progression to the zeolite laumontite. The early dissolution of orthopyroxene and anorthite due to their high dissolution rates (Table 4.4) leads to the initial precipitation of Fe(Ti) oxides and mafic phyllosilicates. The small molar volume of hematite creates no volume increase during precipitation, allowing precipitation to occur in situ without progressing to open vesicle space. As the levels of magnesium and aluminum dissolved into the aqueous solution increase (Table 4.3), clay mineral precipitation dominates the system. The positive instantaneous volume change reaching 14.41% at this stage in the reaction (Figure 4.2C) is then due to the high molar volumes of the chlorite and smectite, causing precipitation to migrate into open pore space and form the observed chlorite rims lining vesicle walls in these samples (Chapter 3). At this stage in the reaction, the model also shows an increase in the amount of quartz in the system, which is observed petrographically as sporadic appearances of silica within the matrix or occasional silica rims observed lining pores.

As the reaction progresses, the aqueous phase acquires enough calcium to become saturated with respect to the zeolite laumontite. This shift from clay minerals to zeolites

appears to be sudden due to the observed consistency in clay rim thicknesses. In other samples of metabasalts where no clay rims line vesicle walls, this shift may have occurred before significant volume change due to clay precipitation, whereas very thick clay rims would suggest a large increase in volume prior to zeolite formation. Once this shift occurs, one or more generations of zeolites will fill any remaining pore space in the basalt, which is usually within or immediately surrounding vesicles. In the modeled basaltic andesite, the precipitation of laumontite causes an instantaneous volume increase of 8.84% (Figure 4.2C) and fills remaining pore space in vesicles. Smaller vesicles which have been closed during earlier stages of alteration will not experience zeolitization, and the relative amount of zeolite crystallization in a given vesicle will increase with vesicle size due to the consistency in clay rim thicknesses.

### **Dependence of Reaction Progress on Pore Size**

Observations described in preceding chapters suggest that the alteration observed in and around vesicles in mafic lavas occurs through fluid-rock interaction at the scale of individual pores. Most notably, the prominent vesicle size dependence on reaction progress noted in Chapter 3 indicates that chemical components are not homogenized across the lava during alteration, but rather that each vesicle independently exchanges chemical components with the surrounding lava matrix. This is most prominently exhibited by the constancy of mafic phyllosilicate rim thicknesses. In addition, the variations in zeolite mineralogy observed between pores in low-grade metabasalt samples observed in previous studies (e.g., Neuhoff *et al.*, 1999; 2006) suggest that local interactions between fluids within vesicles and the surrounding matrix are important. This is not to say that there is not chemical communication between pores, as the relatively high permeabilities of vesicular lavas noted above requires that advective-

dispersive transport leads to solute transport between vesicles. Nonetheless, the prominence of vesicle-scale chemical interaction leads to a number of important conclusions about the coupling between porosity and chemical alteration in vesicular lavas.

The dependence of reaction progress on pore size (e.g., whether zeolites will be developed in a given pore) can be explained using these results of the EQ3/6 models through the use of geometric models. A system is considered where each pore and the lava immediately surrounding it (i.e., the reaction aureole) act as a closed (batch dissolution) system. Figure 5.1 shows a schematic representation of a spherical vesicle of radius  $r_{\text{pore}}$  surrounded by a reaction aureole of thickness  $x_{\text{aureole}}$ , and the radius of the system ( $r_{\text{system}}$ ) is equivalent to  $r_{\text{pore}}$  plus  $x_{\text{aureole}}$ . I can then use this system to interpret the % volume change needed to fill in a pore space given set values of pore size and aureole size.

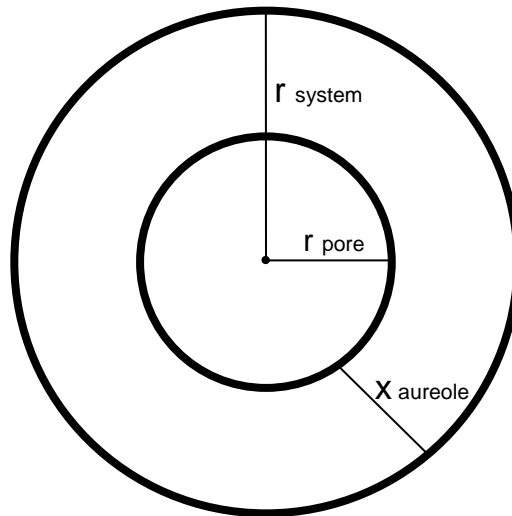


Figure 5.1: Schematic representation of a spherical pore of radius  $r_{\text{pore}}$  surrounded by a reaction aureole of thickness  $x_{\text{aureole}}$ . The radius of the system ( $r_{\text{system}}$ ) is equivalent to  $r_{\text{pore}}$  plus  $x_{\text{aureole}}$ .

The plot in Figure 5.2 depicts the percentage of the volume of the system shown in Figure 5.1 occupied by the vesicle in a given pore-aureole local reaction region as a function of  $r_{\text{pore}}$  and  $x$  using pore sizes and aureole thickness typical of petrographic observations. For a vesicle of a constant size, the necessary aureole thickness required to fill the pore decreases as the % volume change during reaction increases. Inversely, if I increase the aureole thickness (for instance, if the rate of diffusion into the matrix is higher), then less volume increase is required to fill the pore. Note that as aureole thickness increases, the percent of volume occupied by the pore in the system becomes relatively insensitive to pore size. Thus, factors influencing the size of the aureole (i.e.,

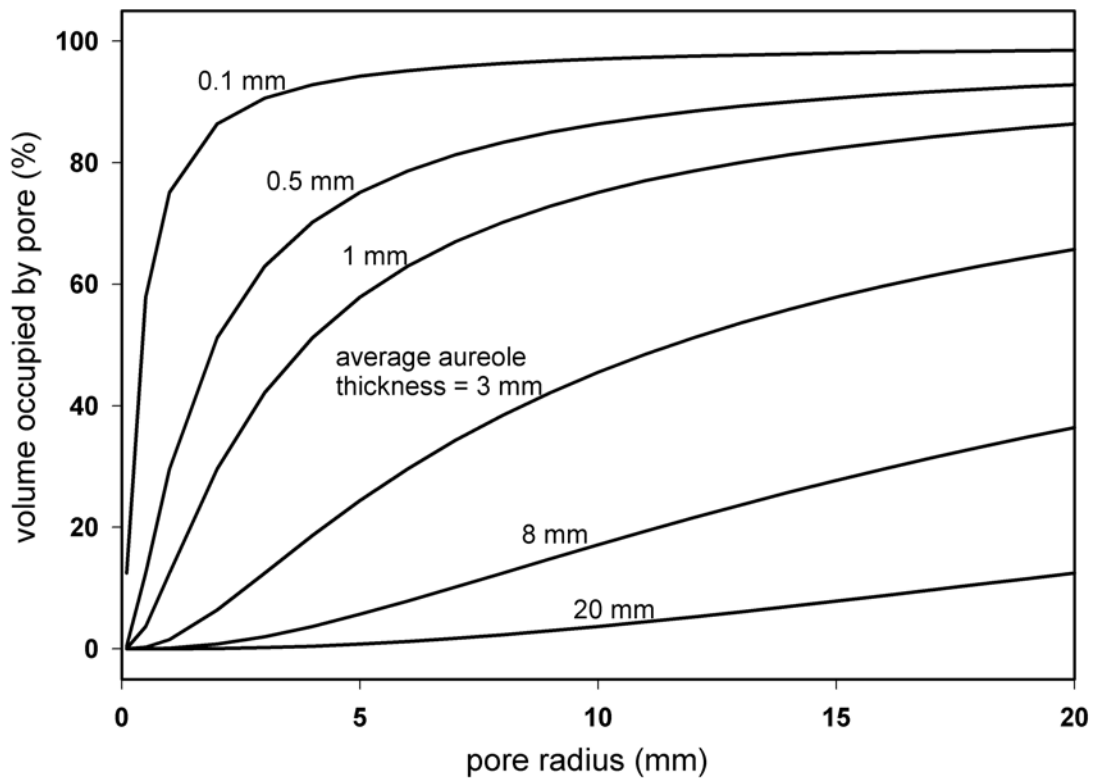


Figure 5.2: Graph depicting the percentage of volume occupied by the pore in a given pore-aureole local reaction region as a function of  $r_{\text{pore}}$  and  $x_{\text{aureole}}$  using pore sizes and aureole thicknesses typical of vesicular mafic lavas.

the extent of aqueous diffusion between the vesicle and the matrix) such as time, temperature, and lava texture should greatly affect the extent of mineral paragenesis and degree of porosity modification.

In a system representative of typical alteration observed in vesicular basalts (Chapter 3), average vesicle radii range from 1-5mm and average total original porosities range from 10-20%. This constrains the aureole thicknesses required to completely close off porosity through secondary mineralization to ~0.5-8 mm, and this observation is consistent with the thickness of the alteration aureoles described in Chapter 3. If the increase in mineral volume during reaction exceeds the volume of the pore, then reaction will stop. For example, in the above EQ3/6 model of the olivine tholeiite, the instantaneous volume increase reaches 15% (Figure 4.2B) during mafic phyllosilicate precipitation. If the alteration aureole at this point in the reaction progress has a thickness of 1 mm, then all pores with radii of ~1 mm will be filled, whereas large pores still retain space for further mineral development (e.g., zeolite formation). The instantaneous volume increase during later zeolite precipitation reaches up to 20%, thus having the ability to fill larger pore space and effectively decreasing porosity in the system to zero.

I can then relate this geometric model to petrographic observations of pore size variations and alteration characteristics to predict the amount of basalt that must be altered to create these features. Petrographic observations of alteration characteristics in the basaltic andesite samples from the NSVG shows initial clay rims lining vesicle walls with a consistent thickness of 0.52 +/- 0.12 mm, with the residual pore space filled by laumontite. These features are schematically represented in Figure 5.3, where the pore radius equals the clay rim thickness plus the radius of the laumontite infilling of residual

pore space. The total thickness of the alteration aureole can then be divided into the thickness required to create the consistent clay rim ( $x_{\text{chlorite}}$ ) plus the additional thickness required to fill residual pore space with laumontite ( $x_{\text{laum}}$ ). These required thicknesses will be sensitive to the vesicle size, as shown in Figure 5.4 where aureole thickness is plotted with respect to pore radius.

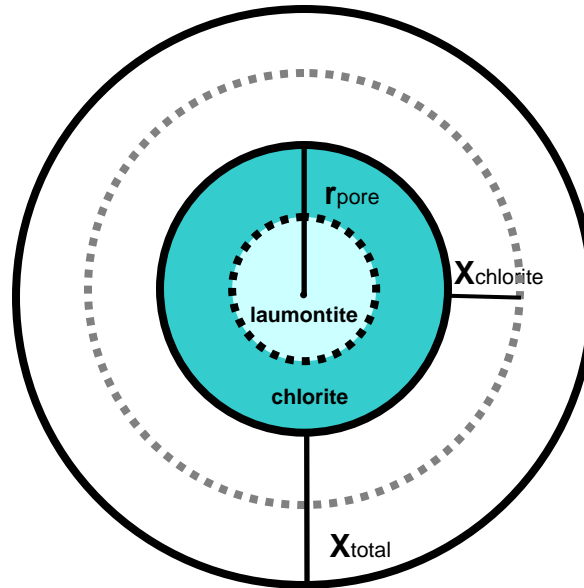


Figure 5.3: Schematic representation of a spherical pore showing secondary infilling typical of the petrographically observed alteration in the basaltic andesite of the NSVG. The vesicle with radius  $r_{\text{pore}}$  is surrounded by a reaction aureole with thickness  $x_{\text{total}}$ .

Modeled alteration of this sample shows that the instantaneous volume change during mafic phyllosilicate precipitation is 14.41%, while the instantaneous volume change during precipitation of laumontite is only 8.84%. This suggests that for a given pore radius, the required amount of basalt alteration to create the chlorite rims will be less than the amount required to create the laumontite infilling. Using Figure 4.6 and assuming a pore radius of 5mm shows that the aureole thickness required to create the chlorite rim is ~2 mm while the entire thickness has to be ~5.5 mm to fill the remaining pore space with laumontite.

The spherical model in Figure 5.1 represents one end-member in a continuum of vesicle shapes that are present in lavas. Vesicles shapes in many flows vary from nearly spherical to highly elongate, and this will have a profound impact on the degree of reaction progress observed in a given vesicle. For instance, Figure 5.5 shows the percent

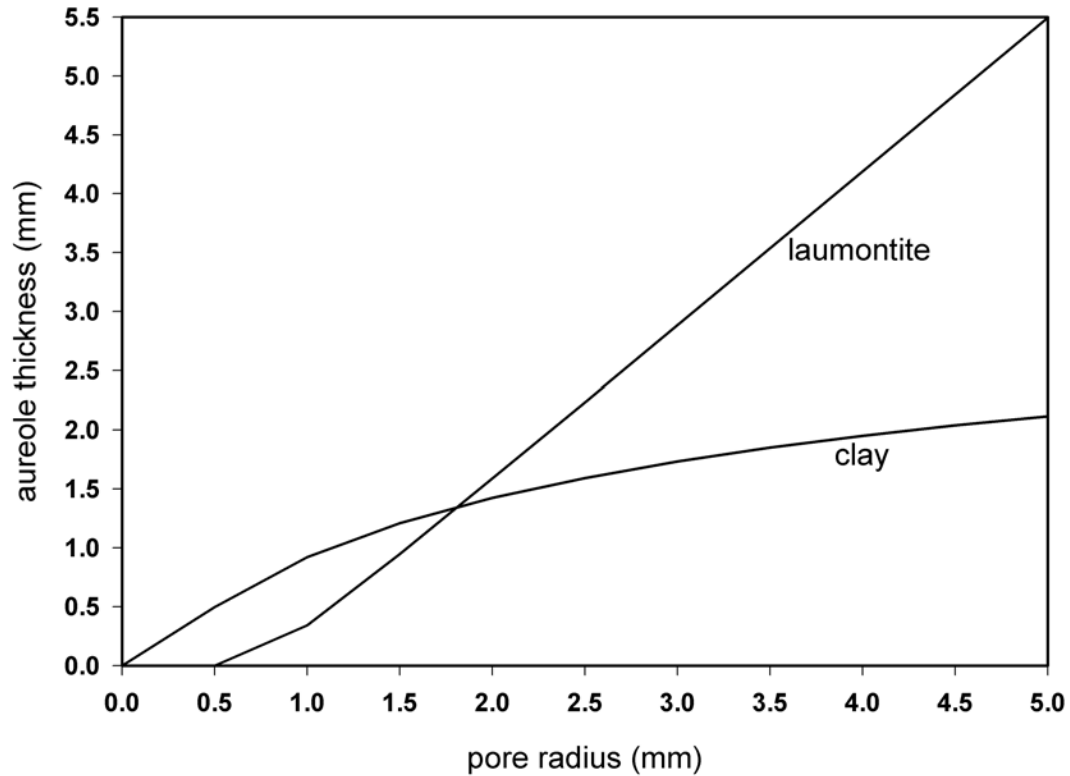


Figure 5.4: Plot depicting the aureole thickness ( $x$ ) required to completely fill pore space within a vesicle of a given pore radius ( $r_{\text{pore}}$ ) with alteration minerals, shown for total infilling and for clay or laumontite infilling.

of chlorite infilling vesicles with volumes equivalent to spheres with radii ( $r_{\text{pore}}$ ) of 0.25, 0.5, and 1 cm assuming a constant chlorite rim thickness of 0.5 mm as a function of the ratio of the length of the long axis over that of the shorter axes (assuming elongation in only one direction). For all pores, the percentage of chlorite infilling increases exponentially with increasing ellipticity (axial ratio). As pore size decreases, the effect of

elongation one the degree of clay infilling increases dramatically. Thus, vesicle shape as well as vesicle size can exert a profound influence on the degree of reaction progress.

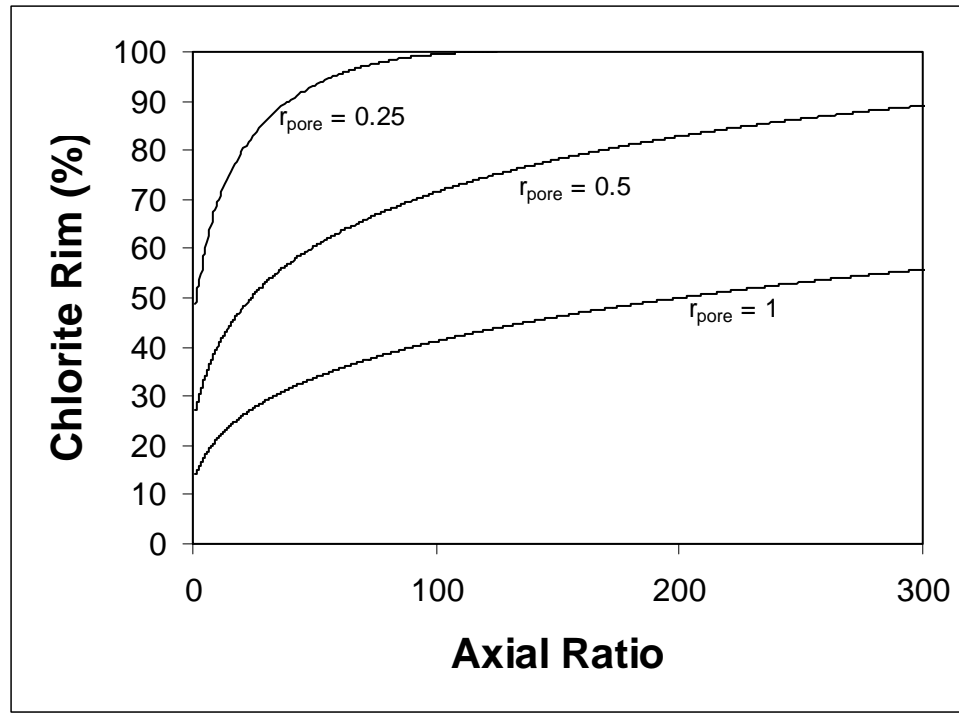


Figure 5.5: Percent chlorite infilling as a function of the axial ratio (ratio of the length of the long axis over that of the two shorter axes) for an ellipsoidal vesicle elongated in one direction assuming a constant volume equivalent to a spherical vesicle with radii of 0.25, 0.5, and 1 cm and a constant chlorite rim thickness of 0.5 mm.

This system is sensitive to many variables, and any small change will cause the numerical values given above to change. For example, the fluid composition used in these models is a dilute aqueous solution which may not be representative of groundwater compositions present during the time of alteration. More chemical constituents available in the initial fluid would allow for more secondary mineral precipitation, thus creating a larger positive volume change and changing the exact values relating the pore radius, aureole thickness and volume % required to occlude porosity. Also, the temperature and pressure conditions for each modeled run are determined based on known conditions

required to form the observed zeolite alteration; these minerals do occur over a small range of conditions, however, and the exact conditions of the model may not coincide exactly with conditions experienced during alteration. This can also be said for other set parameters in the model where assumptions are made in order to best represent the expected conditions, as the model sensitivity to slight variations in these parameters may alter the amount of secondary mineralization experienced during alteration.

## CHAPTER 6 CONCLUSIONS

Secondary mineral parageneses were used to delineate time-dependent changes in the nature of fluid storage capacity and transmission in vesicular lavas. The review of the present state of understanding of the hydrologic properties of vesicular lavas in Chapter 1 led to several questions that formed the motivation for this study. The detailed observations are summarized below with respect to these questions:

1. What causes the high permeabilities of vesicular volcanic rocks, even at low porosities?

Fluid movement through vesicular basalts occurs along a permeable network of microfractures and connected vesicles. The microfractures are usually not visible, but their locations are depicted by the alteration aureoles that surround these pathways and the vesicles they connect. The basalt is highly weathered within these aureoles signifying that these are preserving the pathways of fluid movement through the rock during alteration. This implies that vesicles will experience secondary alteration regardless of their size, shape and spacing as long as they are connected to the fluid flow pathways. This can explain the high permeability observed in vesicular basalts with low porosity and little to no visible interconnection between vesicles, as well as observed patches of completely unaltered vesicles within altered lavas.

There are a number of processes that create various types of microfractures within vesicular basalts. Not all of these microfractures, however, create a network of pathways through the matrix that connect vesicles as observed in the basalts of the NSVG. The

strong presence of spherical vesicles in the high permeability zones of the cooled lava, however, suggests that these vesicles retain gas after cooling which must later escape through the solid rock. This escaping gas will create a connected network of pathways between vesicles and through the matrix, which can then be reused as fluid flow pathways during later events of low-grade alteration.

2. Does the extent of reaction progress (as evidenced by the temporal sequence of mineral infillings of pore space) vary with aspects of pore geometry such as spacing, size, and shape?

AND

3. What is the relationship between pore geometry and porosity evolution during mineral paragenesis?

Though the vesicle-vesicle spacing shows no control on the extent of reaction progress experienced by a given vesicle, there is a heavy influence imposed by the vesicle size and shape. Observations show that mineral assemblages within larger vesicles exhibit greater degrees of reaction progress while smaller ones will become closed off earlier in the reaction progress. In situations where vesicles are ellipsoidal or irregularly shaped, they may close off earlier in the reaction progress even with large areas due to constriction caused by the shortest diameter.

This dependence of reaction progress on pore size is not purely based on the size of the pore, but on the volume % that this pore occupies within a closed pore-aureole system. It has been shown that each vesicle independently exchanges chemical components with the surrounding lava matrix, which implies that the progress of reaction exhibited within a given vesicle is based on the ratio of the vesicle to aureole size. A vesicle that may be small compared to the average size within a given sample has the ability to show low levels of reaction progress if the alteration around this vesicle is also

very small. Inversely, a smaller alteration aureole around a larger vesicle implies less fluid-rock interaction, which may be seen in lower grades of alteration or younger lavas, as this may not create enough secondary mineralization to progress to later stages of alteration or to completely fill the pore space.

## LIST OF REFERENCES

- Aharonov, E., Spiegelman, M., and Kelemen, P., 1997, Three-dimensional flow and reaction in porous media: Implications for the Earth's mantle and sedimentary basins: *Journal of Geophysical Research*, v. 102, p. 14,821-14,834.
- Allen, D.J., Hinze, W.J., Dickas, A.B., Mudrey, M.G. Jr, 1997, Integrated geophysical modeling of the North American Midcontinent Rift System: New interpretations for western Lake Superior, north-western Wisconsin, and eastern Minnesota, *in* Ojakangas, R.W., Dickas, A.B., and Green, J.C., eds., *Middle Proterozoic to Cambrian Rifting, Central North America*: Boulder, Colorado, Geological Society of America Special Paper 312.
- Allen, D., Hinze, W., and Cannon, W., 1992, Drainage, topographic, and gravity anomalies in the Lake Superior region: Evidence for a 1100 Ma mantle plume: *Geophysical Research Letters*, v. 19, p. 2119-2122.
- Al-Harhi, A.A., Al-Amri, R.M., and Shehata, W.M., 1999, The porosity and engineering properties of vesicular basalt in Saudi Arabia: *Engineering Geology*, v. 54, p. 313-320.
- Arnorsson, S., 1995a, Geothermal systems in Iceland: Structure and conceptual models. 1. High temperature areas. *Geothermics*, v. 24, p. 561-602.
- Arnorsson, S., 1995b, Geothermal systems in Iceland: Structure and conceptual models. 2. Low temperature Areas: *Geothermics*, v. 24, p. 603-629.
- Balashov, V.N., and Yardley, B.W.D., 1998, Modeling metamorphic fluid flow with reaction-compaction-permeability feedbacks: *American Journal of Science*, v. 298, p. 441-470.
- Basaltic Volcanism Study Project, 1981, *Basaltic volcanism on the terrestrial planets*: Pergamon Press, New York, 1289 p.
- Bevins, R.E., Robinson, D., and Rowbotham G., 1991, Compositional variations in mafic phyllosilicates from regional low-grade metabasites and application of the chlorite geothermometer: *Journal of Metamorphic Geology*, v. 9, p. 711-721.
- Blower, J.D., 2001a, Factors controlling porosity-permeability relationships in magma: *Bulletin of Volcanology*, v. 63, p. 497-503.

- Blower, J. D., 2001b, A three-dimensional network model of permeability in vesicular material: *Computers and Geosciences*, v. 27, p. 115-119.
- Boerboom, T., Miller, J., Green, J., 2004, Geologic highlights of new mapping in the southwestern sequence of the North Shore Volcanic Group and in the Beaver Bay Complex, *in* Severson, M. J., and Heinz, J., ed., *Institute on Lake Superior geology: Duluth, Part 2 – Field Trip Guidebook*, p. 46-85.
- Bolton, E.W., Lasaga, A.C., and Rye, D.M., 1999, Long-term flow/chemistry feedback in a porous medium with heterogeneous permeability: kinetic control of dissolution and precipitation: *American Journal of Science*, v. 299, p. 1-68.
- Bosl, W.J., Dvorkin, J., Nur, A., 1998, A study of porosity and permeability using a lattice Boltzmann simulation: *Geophysical Research Letters*, v. 25, no. 9, p. 1475-1478.
- Brannon, J.C., 1984, *Geochemistry of successive lava flows of the Keweenaw North Shore Volcanic Group*; Doctoral Thesis, Washington University, St. Louis, Mo.
- Broedehoeft, J.D., and Norton, D.L., 1990, Mass and energy transport in deforming Earth's crust, *in* *The Role of Fluids in Crustal Processes*, Washington, D.C.: National Academy, p. 27-41.
- Burgisser, A., Gardner, J.E., 2004, Experimental constraints on degassing and permeability in volcanic conduit flow: *Bull. Volcanol.*, v. 67, p. 42-56.
- Cannon, W.F., 1994, Closing of the midcontinent rift – a far-field effect of Grenvillian compression: *Geology*, v. 22, p. 155-158.
- Cannon, W.F., 1992, The Midcontinent rift in the Lake Superior region with emphasis on its geodynamic evolution: *Tectonophysics*, v. 213, p. 41-48.
- Cannon, W.F., Cannon, W.C., Green, A.G., Hutchinson, D.R., Lee, M.W., Milkereit, B., Behrendt, J.C., Halls, H.C., Green, J.C., Dickas, A.B., Morey, G.B., Sutcliffe, R., Spencer, C., 1989, The Midcontinent rift beneath Lake Superior from GLIMPCE seismic reflection profiling: *Tectonics*, v. 8, p. 305-332.
- Carman, P.C., 1956, *Flow of Gases Through Porous Media*: Academic, San Diego, 182 p.
- Cashman, K.V., and Mangan, M.T., 1994, Physical aspects of magmatic degassing II. Constraints on vesiculation processes from textural studies of eruptive products, *in* Carroll, M.R., and Holloway, J.R. (eds) *Volatiles in magmas: Mineralogical Society of America Reviews in Mineralogy* 30, p. 447-478.
- Cathles, L.M., 1981, Fluid flow and hydrothermal ore deposits: *Economic Geology*, v. 75, p. 424-457.

- Cathles, L.M., 1990, Scales and effects of fluid flow in the upper crust: *Science*, v. 248, p. 323-328.
- Christiansen, F.G., 1994, Seeps and other bitumen showings: A review of origin, nomenclature and occurrences in Greenland: *Open File Series Grønlands Geologiske Undersøgelse*, 94/7, 41 p.
- Christiansen, F. G., Boesen, A., Bojesen-Koefoed, J., Dallhoff, F., Dam, G., Neuhoff, P. S., Pedersen, A. K., Pedersen G. K., Stannius, L. S., and Zinck-Joergensen, K., 1999, Petroleum geological activities onshore West Greenland in 1997: *Geology of Greenland Survey Bulletin*, v. 180, p. 10-17.
- Coffin, M.F., Eldholm, O., 1994, Large Igneous Provinces: Crustal structure, dimensions, and external consequences: *Reviews of Geophysics*, v. 32, p. 1-36.
- Dewers, T., and Ortoleva, P., 1990, Geochemical self-organization III: Mechano-chemical mode of metamorphic differentiation: *American Journal of Science*, v. 290, p. 473-521.
- Dullien, F.A.L., 1992, *Porous media; fluid transport and pore structure*: Academic Press, San Diego, CA, United States, 574p.
- Eichelberger, J. C., Carrigan, C. R., Westrich, H. R., and Price, R. H., 1986, Non-explosive silicic volcanism: *Nature*, v. 323, p. 598-602.
- Etheridge, M.A., Wall, V.J., and Vernon, R.H., 1983, The role of the fluid phase during regional metamorphism and deformation: *Journal of Metamorphic Geology*, v. 1, p. 205-226.
- Feng, S., Halperin, B.I., Sen, P.N., 1987, Transport properties of continuum systems near the percolation threshold: *Physical Review B*, v. 35, p. 197-214.
- Fisher, A.T., 1998, Permeability within basaltic oceanic crust: *Reviews of Geophysics*, v. 36, p. 143-182.
- Freedman, V.L., Saripalli, K.P., and Meyer, P.D., 2003, Influence of mineral precipitation and dissolution on hydrologic properties of porous media in static and dynamic systems: *Applied Geochemistry*, v. 18, p. 589-606.
- Gardner, J.E., Thomas, R.M.E., Jaupart, C., Tait, S., 1996, Fragmentation of magma during Plinian volcanic eruptions: *Bull. Volcanol.*, v. 58, p. 144-162.
- Garven, 1989, The role of regional fluid flow in the genesis of the Pine Point deposit. reply: *Economic Geology*, v. 81, p. 1015-1020.
- Garven, G., 1985, The role of regional fluid flow in the genesis of the Pine Point deposit: *Economic Geology*, v. 81, p. 307-324.

- Garven, G., 1995, Continental-scale groundwater flow and geologic processes: Annual Review of Earth and Planetary Sciences, v. 24, p. 89-117.
- Garven, G., and Freeze, R.A., 1984a, Theoretical analysis of the role of groundwater flow in the genesis of a stratabound ore deposit: 1. Mathematical and numerical model: American journal of Science, v. 284, p. 1085-1124.
- Garven, G., and Freeze, R.A., 1984b, Theoretical analysis of the role of groundwater flow in the genesis of a stratabound ore deposit: 2. Quantitative results: AmericanJournal of Science, v. 284, p. 1125-1174.
- Garven, G., and Raffensperger, J.P., 1994, Hydrogeology and geochemistry of ore genesis in sedimentary basins, *in* Barnes, H.L., ed., The Geochemistry of Hydrothermal Ore Deposits, ch. 4, in press.
- Garven, G., Ge, S., Person, M.A., and Sverjensky, D.A., 1993, Genesis of stratabound ore deposits in the Midcontinent basins of North America. 1. The role of regional groundwater flow: American Journal of Science, v. 293, p. 497-568
- Gislason, S.R., and Eugster, H.P., 1987, Meteoric water-basalt interactions; I, A laboratory study: Geochimica et Cosmochimica Acta, v. 51, no.10, p. 2827-2840.
- Green, J.C., 1982, Geology of the Keweenawan extrusive rocks: Geological Society of America Memoir 156.
- Grimmett, G., 1999, Percolation, 2<sup>nd</sup> edition: Berlin Heiderlberg New York, Springer.
- Hearn, P.P, Jr., Steinkampf, W.C., Horton, D.G., Solomon, G.C., White, L.D., and Evans, J.R., 1989, Oxygen-isotope composition of ground water and secondary minerals in Columbia Plateau basalts; implications for the paleohydrology of the Pasco Basin: Geology, v. 17, p. 606-610.
- Hinze, W.J., David, J.A., Lawrence, W.B., Mariano, J., 1997, The Midcontinent Rift System: A major Proterozoic continental rift, *in* Ojakangas, R.W., Dickas, A.B., and Green, J.C., eds., Middle Proterozoic to Cambrian Rifting, Central North America: Boulder, Colorado, Geological Society of America Special Paper 312.
- Iijima, A., 2001, Zeolites in petroleum and natural gass reservoirs, *in* Bish, D.L., and Ming, D.W., eds., Natural Zeolites: Occurrence, Properties, Applications: Reviews in Mineralogy and Geochemistry, Mineralogical Society of America and the Geochemical Society, Washington, D.C., p. 347-402.
- Ingebritsen, S. E., and M. A. Scholl, 1993, The hydrology of Kilauea volcano. Geothermics, v. 22, p. 255-270.
- Jakobsson, S.P., and Moore, J.G., 1986, Hydrothermal minerals and alteration rates at Surtsey volcano, Iceland: Geological Society of America Bulletin, v. 97, p. 648-659.

- Johnson, J.W., Oelkers, E.H., and Helgeson, H., 1992, CSUPCRT92; a software package for calculating the standard molal thermodynamic properties of minerals, gases, aqueous species, and reactions from 1 to 5000 bar and 0 to 1000 degrees C: Computers & Geosciences, vol.18, no.7, pp.899-947.
- Johnson, D. M., 1980, Crack distribution in the upper oceanic crust and its effects upon seismic velocity, seismic structure, formation permeability, and fluid circulation: Initial Reports, Deep Sea Drilling Project, v. 51-53, p. 1479-1490.
- Jorgensen, O., 1984, Zeolite zones in the basaltic lavas of the Faeroe Islands, *in* The deep drilling project 1980-1981 in the Faeroe Islands: Annales Societatis Scientiarum Faroensis, Supplementum, v. 9, p. 71-91.
- Klug, C., and Cashman, K. V., 1996, Permeability development in vesiculating magmas: implications for fragmentation: Bulletin of Volcanology, v. 58, p. 87-100.
- Kononov, 1978, Hydrogeology of Iceland: International Geology Review, v. 21, no. 4, p. 385-398.
- Kowallis, B.J., Roeloffs, E.A., and Wang, H.F., 1982, Microcrack studies of basalts from the Iceland Research Drilling Project: Journal of Geophysical Research, v. 87, no. B8, p. 6650-6656.
- Kristmannsdóttir, H., and Tómasson, J., 1978, Zeolite zones in geothermal areas in Iceland, *in* Sand, L. B., and Mumpton, F. A., ed., Natural Zeolites: Oxford, Pergamon Press Ltd., p. 277-284.
- Larsen, J.F., Denis, M.H., Gardner, J.E., 2004, Experimental study of bubble coalescence in rhyolitic and phonolitic melts: Geochemica et Cosmochimica Acta, v. 68, no. 2, p. 333-344.
- Lasaga, A.C., 1986, Metamorphic reaction rate laws and the development of isograds: Mineralogical Magazine, v. 50, p. 359-373.
- Lasaga, A.C., 1989, Fluid flow and chemical reaction kinetics in metamorphic systems: a new simple model: Earth and Planetary Science Letters, v. 94, p. 417-424.
- Lasaga, A.C., and Rye, D.M., 1993, Fluid flow and chemical reaction kinetics in metamorphic systems: American Journal of Science, v. 293, p. 361-404.
- Lee, S. B., 1990, Universality of continuum percolation: Physics Reviews, v. 42, p. 4877-4880.
- Le Gallo, Y., Bildstein, O., and Brosse, E., 1998, Coupled reaction-flow modeling of diagenetic changes in reservoir permeability, porosity, and mineral compositions: Journal of Hydrology, v. 209, p. 366-388.

- Le Maitre, R.W., Bateman, P., Dudek, A., Keller, J., Lameyre Le Bas, M.J., Sabine, P.A., Schmid, R., Sorensen, H., Streckeisen, A., Woolley, A.R., and Zanettin, B., 1989, *A Classification of Igneous Rocks and Glossary of Terms*: Oxford, Blackwell.
- Lichtner, P.C., Steefel, C.I., and Oelkers, E.H., eds., 1996, *Reactive transport in porous Media: Mineralogical Society of American Reviews in Mineralogy v. 34*, 438 p.
- Luo, J., Morad, S., Liang, Z., and Zhu, Y., 2005, Controls on the quality of Archean metamorphic and Jurassic volcanic reservoir rocks from the Xinglongtai buried hill, western depression of Liaohe basin, China: *American Association of Petroleum Geologists Bulletin*, v. 89, p. 1319-1346.
- Lysak, S.V., 1992, Heat flow variations in continental rifts: *Tectonophysics*, v. 208, p. 309–323.
- Manning, C.E., and Bird, D.K., 1991, Porosity evolution and fluid flow in the basalts of the Skaergaard magma-hydrothermal system, East Greenland: *American Journal of Science*, v. 291, no. 3, p. 201-257.
- Manning, C.E., and Bird, D.K., 1995, Porosity, permeability, and basalt metamorphism: *Special Paper – Geological Society of America*, v. 296, p. 123-140.
- Manning, C.E., Ingebritsen, S.E., and Bird, D.K., 1993, Missing mineral zones in contact metamorphosed basalts. *American Journal of Science*, v. 293, p. 894-938.
- Manga, M., 1997, A model for discharge in spring-dominated streams and implications for the transmissivity and recharge of quaternary volcanics in the Oregon Cascades: *Water Resources Research*, v. 33, p. 1813-1822.
- Manga, M., 1999, On the timescales characterizing groundwater discharge at springs: *Journal of Hydrology*, v. 219, p. 56-69.
- Miller, J.D., Jr., Green, J.C., Severson, M.J., Chandler, V.W., and Peterson, D.M., 2001, *Geologic map of the Duluth Complex and related rocks, northeastern Minnesota*: Minnesota Geological Survey Miscellaneous Map M-119, scale 1:200000.
- Miller, J.D., Jr., Green, J.C., Severson, M.J., Chandler, V.W., Hauck, S.A., Peterson, D.M., and Wahl, T.E., 2002, *Geology and mineral potential of the Duluth Complex and related rocks of northeastern Minnesota*: Minnesota Geological Survey Report of Investigations 58, 207 p.
- Mueller, S., Melnik, O., Spieler, O., Scheu, B., Dingwell, D.B., 2004, Permeability and degassing of dome lavas undergoing rapid decompression: An experimental determination: *Bull. Volcanol.*, v. 60, p. 526-538.
- Murata, K. J., Formoso, M. L. L., and Roisenberg, A., 1987, Distribution of zeolites in lavas of southeastern Parana Basin, state of Rio Grande do Sul, Brazil: *Journal of Geology*, v. 95, p. 455-467.

- Neuhoff, P.S., Rogers, K.L., Stannius, L.S., Bird, D.K., Pedersen, A.K., 2006, Regional very low-grade metamorphism of basaltic lavas, Disko-Nuussuaq Region, West Greenland: *Lithos*, *in press*.
- Neuhoff, P. S., Fridriksson, T., Bird, D. K., 2000, Zeolite paragenesis in the North Atlantic Igneous Province: implications for geotectonics and groundwater quality of basaltic crust: *International Geology Review*, v. 42, p. 15-44.
- Neuhoff, P. S., Fridriksson, T., Arnorsson, S., 1999, Porosity evolution and mineral paragenesis during low-grade metamorphism of basaltic lavas at Teigarhorn, Eastern Iceland: *American Journal of Science*, v. 299, p. 467-501.
- Neuhoff, P.S., Watt, W.S., Bird, D.K., and Pedersen, A.K., 1997, Timing and structural relations of regional zeolite zones in basalts of the East Greenland continental margin: *Geology*, v. 25, p. 803-806.
- Norton, D., 1988, Metasomatism and permeability: *American Journal of Science*, v. 288, p. 604-618.
- Norton, D.L., 1984, Theory of hydrothermal systems: *Annual Review of Earth and Planetary Sciences*, v. 12, p. 155-177.
- Norton, D., and Knight, J., 1977, Transport phenomena in hydrothermal systems: cooling plutons: *American Journal of Science*, v. 277, p. 937-981.
- Ojakangas, R.W., and Dickas, A.B., 2002, The 1.1-Ga Midcontinent Rift System, central North America: sedimentology of two deep boreholes, Lake Superior region: *Sedimentary Geology*, v. 147, p. 13-36.
- Ojakangas, R.W., and Matsch, C.L., 1982, *Minnesota's Geology*: Minneapolis, the University of Minnesota Press, 255 p.
- Ortoleva, P., Chadam, J., Merino, E., and Sen, A., 1987, Geochemical self-organization II: The reactive-infiltration instability: *American Journal of Science*, v. 287, p. 1008-1040.
- Oxburgh, E.R., and Argell, S.G., 1982, Thermal conductivity and temperature structure of the Reydarfjörður borehole: *Journal of Geophysical Research*, v. 87, p. 6423-6428.
- Palandri, J.L., and Kharaka, Y.K., 2004, A compilation of rate parameters of water-mineral interaction kinetics for application to geochemical modeling: Open-File Report - U. S. Geological Survey, Report: OF 2004-1068, 64 p.
- Panda, M. N. and Lake, L. W., 1995, A physical model of cementation and its effects on single phase permeability: *American Association of Petroleum Geologists Bulletin*, v. 79, p. 431-434.

- Park, A.J., and Ortoleva, P.J., 2003, WRIS.TEQ: Multimineralic water-rock interaction, mass transfer and textural dynamics simulator: *Computers and Geosciences*, v. 29, p. 277-290.
- Pendkar, N., and Kumar, A., 1999, Delineation of reservoir section in Deccan Trap basement, example from Padra Field, Cambay Basin: *Bulletin of the Oil and Natural Gas Corporation Limited*, v. 36, p. 83-88.
- Person, M., Raffensperger, J.P., Ge, S., and Garven, G., 1996, Basin-scale hydrogeologic modeling: *Reviews of Geophysics*, v. 34, p. 61-87.
- Putnis, A., 2002, Mineral replacement reactions; from macroscopic observations to microscopic mechanisms: *Mineralogical Magazine*, v. 66, no. 5, p 689-708.
- Raffensperger, J.P., and Garven, G., 1995a, The formation of unconformity-type uranium ore deposits. 1. Coupled groundwater flow and heat transport modeling: *American Journal of Science*, v. 295, p. 581-636.
- Raffensperger, J.P., and Garven, G., 1995b, The formation of unconformity-type uranium ore deposits. 2. Coupled hydrochemical modeling: *American Journal of Science*, v. 295, p. 639-696.
- Robert, C., 2001, Hydrothermal alteration processes of the Tertiary lavas of Northern Ireland: *Mineralogical Magazine*, v. 65, p. 543-554.
- Robert, C., and Goffé, B., 1993, Zeolitization of basalts in subaqueous freshwater settings: Field observations and experimental study: *Geochimica et Cosmochimica Acta*, v. 57, p. 3597-3612.
- Rose, N.M., 1995, Geochemical consequences of fluid flow in porous basaltic crust containing permeability contrasts: *Geochimica et Cosmochimica Acta*, v. 59, p. 4381-4392.
- Rose, T.P., Davisson, M.L., Criss, R.E., 1996, Isotope hydrology of voluminous cold springs in fractured rock from an active volcanic region, northeastern California: *Journal of Hydrology*, v. 179, p. 207-236.
- Saar, M.O., 1998, The relationship between permeability, porosity and microstructure in vesicular basalts [Master's Thesis]: University of Oregon, p. 1-101.
- Saar, M. O., Manga, M., 1999, Permeability – porosity relationship in vesicular basalts: *Geophysical Research Letters*, v. 26, no. 1, p 111-114.
- Sahagian, D.L., and Proussevitch, A.A., 1998, 3D particle size distributions from 2D observations: Stereology from natural applications: *Journal of Volcanology and Geothermal Research*, v. 84, p. 173-196.

- Sahagian, D.L., Anderson, A.T., and Ward, B., 1989, Bubble coalescence in basalt flows: Comparison of a numerical model with natural examples: *Bulletin of Volcanology*, v. 52, p. 49-56.
- Sahagian, D.L., Proussevitch, A.A., and Carlson, W.D., 2002, Analysis of vesicular basalts and lava emplacement processes for application as a paleobarometer/paleoaltimeter: *The Journal of Geology*, v. 110, p. 671-685.
- Saemundsson, K., 1979, Outline of the geology of Iceland: *Joekull*, no. 29, p.7-28.
- Sahimi, M., 1994, Applications of percolation theory: Taylor and Francis, London, p. 1-300.
- Sahimi, M., 1995, Flow and Transport in Porous Media and Fractured Rocks: VHC Verlagsgesellschaft mbH, Weinheim, p. 1-496.
- Saripalli, K.P., Meyer, P.D., Parker, K.E., and Lindberg, M.J., 2005, Effect of chemical reactions on the hydrologic properties of fractured and rubberized glass media: *Applied Geochemistry*, v. 20, p. 1677-1686.
- Saripalli, K.P., Meyer, P.D., Bacon, D.H., and Freedman, V.L., 2001, Changes in hydrologic properties of aquifer media due to chemical reactions: a review: *Critical Reviews in Environmental Science and Technology*, v. 31, p. 311-349.
- Schiffman, P., and Fridleifsson, G.Ó., 1991, The smectite-chlorite transition in drillhole NJ-15, Nesjavellir geothermal field, Iceland: XRD, BSE and electron microprobe investigations: *Journal of Metamorphic Geology*, v. 9, p. 679-696.
- Schmidt, S.Th., 1993, Regional and local patterns of low-grade metamorphism in the North Shore Volcanic Group, Minnesota, USA: *Journal of Metamorphic Geology*, v. 11, p. 401-414.
- Schmidt, S.T., 1990, Alteration under conditions of burial metamorphism in the North Shore Volcanic Group, Minnesota – Mineralogical and geochemical zonation [Ph.D. thesis]: Heidelberg, Heidelberg Geowissenschaftliche Abhandlungen, 309 p.
- Schmidt, S.T., Robinson, D., 1997, Metamorphic grade and porosity and permeability controls on mafic phyllosilicate distributions in a regional zeolite to greenschist facies transition of the North Shore Volcanic Group, Minnesota: *GSA Bulletin*, v. 109, no. 6, p. 683-697.
- Song, S.-R., Jones, K.W., Lindquist, W.B., Down, B.A., and Sahagian, D.L., 2001, Synchrotron X-ray computed microtomography: studies on vesiculated basaltic rocks: *Bulletin of Volcanology*, v. 63, p. 252-263.

- Sruoga, P., Rubinstein, N., and Hinterwimmer, G., 2004, Porosity and permeability in volcanic rocks: a case study on the Serie Tobífera, South Patagonia, Argentina: *Journal of Volcanology and Geothermal Research*, v. 132, p. 31-43.
- Steeffel, C.I., and Lasaga, A.C., 1992, Putting transport into water-rock interaction models: *Geology*, v. 20, p. 680-684.
- Steeffel, C.I., and Lasaga, A.C., 1994, A coupled model for transport of multiple chemical species and kinetic precipitation/dissolution reactions with applications to reactive flow in single phase hydrothermal systems: *American Journal of Science*, v. 294, p. 529-592.
- Steeffel, C.I., and Van Cappellen, P., 1990, A new kinetic approach to modeling water-rock interaction: the role of nucleation, precursors, and Ostwald ripening: *Geochimica et Cosmochimica Acta*, v. 54, p. 2657-2677.
- Stimac, J.A., Powell, T.S., and Golla, G.U., 2004, Porosity and permeability of the Tiwi geothermal field, Philippines based on continuous and spot core measurements: *Geothermics*, v. 33, p. 87-107.
- Sukheswala, R. N., Avasia, R. K., and Gangopadhyay, M., 1974, Zeolites and associated secondary minerals in the Deccan Traps of western India: *Mineralogical Magazine*, v. 39, p. 658-671.
- Tingle, T.N., Neuhoff, P.S., Ostergren, J.D., Jones, R.E., and Donovan, J.J., 1996, The effect of "missing" (unanalyzed) oxygen on quantitative electron microprobe microanalysis of hydrous silicate and oxide minerals: *Geological Society of America, Abstracts with Programs*, v. 28, p. A-212.
- Toramaru, A., 1990, Measurement of bubble size distribution in vesiculated rocks with implications for quantitative estimation of eruptive processes: *Geothermal Research*, v. 43, p. 71-90.
- Van Schmus, W.R., and Hinze, W.J., 1985, The Midcontinent Rift System: *Annual Reviews of Earth and Planetary Sciences*, v. 13, p. 345-383.
- Vervoort, J.D., and Green, J.C., 1997, Origin of evolved magmas in the Midcontinent rift system, northeast Minnesota: Nd-isotope evidence for melting of Archean crust: *Canadian Journal of Earth Science*, v. 34, p. 521-535.
- Walker, G. P. L., 1951, The amygdale minerals in the Tertiary lavas of Ireland. I. The distribution of chabazite habits and zeolites in the Garron plateau area, County Antrim: *Mineralogy Magazine*, v. 29, p. 773-791.
- Walker, G. P. L., 1960a, The amygdale minerals in the Tertiary lavas of Ireland. III. Regional distribution: *Mineralogical Magazine*, v. 32, p. 503-527.

- Walker, G. P. L., 1960b, Zeolite zones and dike distribution in relation to the structure of the basalts of eastern Iceland: *Journal of Geology*, v. 68, p. 515-528.
- Wedepohl, K.H., 1969, *Composition and abundance of common igneous rocks*: New York, Springer, p. 227-249.
- White, W.S., 1966, Tectonics of the Keweenawan basin, western Lake Superior region: U.S. Geological Survey Professional Paper 524-E, p. E1-E23.
- Winter, J.D., 2001, *An Introduction to Igneous and Metamorphic Petrology*: Upper Saddle River, Prentice-Hall Inc., 697 p.
- Wohletz, K.H., 1999, Magma, Los Alamos National Laboratory computer code LA-CC 99-28, Los Alamos, NM.
- Wolery, T. J., 1979, Calculation of chemical equilibria between aqueous solutions and minerals: The EQ3/6 software package: Lawrence Livermore National Laboratory Report, UCRL-52658.
- Wolery, T. J., Jackson, K. J., Bourcier, W. L., Bruton, C. J., Viani, B. E., Knauss, K. B., and Delany, J. M., 1990, Current status of the EQ3/6 software package for geochemical modeling, *in* Melchior, D. C., and Bassett, R. L., ed., *Chemical Modeling in Aqueous Systems II.*: American Chemical Society, p. 104-116.
- Wood, J.R., and Hewett, T.A., 1984, Reservoir diagenesis and convective fluid flow, *in* McDonald, D.A., and Surdam, R.C., eds., *Clastic Diagenesis*: American Association of Petroleum Geologists Memoir, v. 37, p. 3-13.
- Xu, T., and Pruess, K., 2001, Modeling multiphase non-isothermal fluid flow and reactive geochemical transport in variably saturated fractured rocks: 1. Methodology: *American Journal of Science*, v. 301, p. 16-33.

## BIOGRAPHICAL SKETCH

Jane E. Gustavson was born in Milwaukee, Wisconsin, in April of 1980 to James M. Gustavson. She graduated from Wauwatosa East High School in the Spring of 1998, and started college immediately in the Fall to work towards a degree in geology. After a semester at Winona State University and a year at the University of Wisconsin – Milwaukee, she spent her last two and a half years at the University of Wisconsin – Oshkosh, receiving her Bachelor of Science in 2002. In 2003, she began her graduate work in the Department of Geological Sciences at the University of Florida under the guidance of Dr. Philip Neuhoff. Following graduation, Jane plans to pursue a career in geology that focuses on practical applications of her thesis work.